

**Low Energy Proton Transfer Reactions by
Deuterons on Light Nuclei with Astrophysical
Applications**

by
Arthur K. Pallone

ProQuest Number: 10796861

All rights reserved

INFORMATION TO ALL USERS

The quality of this reproduction is dependent upon the quality of the copy submitted.

In the unlikely event that the author did not send a complete manuscript and there are missing pages, these will be noted. Also, if material had to be removed, a note will indicate the deletion.



ProQuest 10796861

Published by ProQuest LLC (2019). Copyright of the Dissertation is held by the Author.

All rights reserved.

This work is protected against unauthorized copying under Title 17, United States Code
Microform Edition © ProQuest LLC.

ProQuest LLC.
789 East Eisenhower Parkway
P.O. Box 1346
Ann Arbor, MI 48106 – 1346

A thesis submitted to the Faculty and the Board of Trustees of the Colorado School of Mines in partial fulfillment of the requirements for the degree of Doctor of Philosophy (Applied Physics).

Golden, Colorado

Date 6/22/2000

Signed: Arthur K. Pallone
Arthur K. Pallone

Approved: M. A. Hofstee
Dr. Mariet A. Hofstee
Assistant Professor of Physics
Thesis Advisor

Approved: F. Edward Cecil
Dr. F. Edward Cecil
Professor of Physics
Thesis Co-Advisor

Golden, Colorado

Date 6/22/00

Don L. Williamson
Dr. Don L. Williamson
Professor and Head
Department of Physics

ABSTRACT

Low energy nuclear reactions on light nuclei are important for understanding stellar and big bang nucleosynthesis. The reactions also are important in fusion reactor diagnostics. To complement previous angular distribution measurements of the (d,p) reactions, the current research investigates the analog (d,n) reactions. The γ photon flux accompanying the neutrons required excellent neutron - γ discrimination. A pulse shape discriminator was used to reject the γ signal for the (d,n) experiments. The detector - discriminator combination also performed well as a γ spectrometer. Measurements of the (d,n) reaction on ^2H , ^6Li , ^7Li , ^9Be , ^{10}B , and ^{11}B were performed at deuteron laboratory energies below 150 keV. The relative angular distributions, absolute reaction cross sections, and astrophysical S-factors were derived. The application of the cross section results to stellar and big bang nucleosynthesis and to fusion diagnostics was discussed.

TABLE OF CONTENTS

ABSTRACT	iii
LIST OF FIGURES	vi
LIST OF TABLES	xi
ACKNOWLEDGEMENTS	xiii
Chapter 1 INTRODUCTION	1
1.1 Motivation	1
1.2 Energy Regime	3
1.3 Literature Search	4
Chapter 2 NEUTRON DETECTION	6
2.1 Neutron Interactions with Matter	6
2.2 Pulse Shape Discrimination	12
Chapter 3 INSTRUMENTATION	16
3.1 The Pulse Shape Discriminator	16
3.2 Accelerator	19
3.2.1 Requirements	19
3.2.2 Cockcroft-Walton Design	19
3.2.3 Accelerator Details	22
Chapter 4 THE DETECTOR	27
4.1 Response of Bicron BC-501A to MeV photons	27
4.1.1 Data collection	27
4.1.2 Energy calibration	29
4.1.3 γ -Efficiency	30
4.1.4 Time axis calibration	30
4.2 Response of BC-501A to neutrons	35
Chapter 5 THEORY OF REACTIONS AND CROSS SECTIONS	42
5.1 Reaction Yields	42

5.2	Nonresonant Cross Sections and the Astrophysical S-Factor	45
5.3	Effective energy and relative cross sections	50
Chapter 6	THE REACTIONS	54
6.1	Validation of the Kent State University Neutron Detection Efficiency Code with the known reaction ${}^2\text{H}(d,n){}^3\text{He}$	54
6.2	${}^6\text{Li}(d,n){}^7\text{Be}$ - an improved measurement at low energy	67
6.3	Cross sections for the direct decay reaction ${}^7\text{Li}(d,n){}^8\text{Be} \rightarrow 2\alpha$	73
6.4	The ${}^{10}\text{B}(d,n){}^{11}\text{C}$ reaction	86
6.5	The ${}^{11}\text{B}(d,n){}^{12}\text{C}$ reaction.	94
6.6	Observation of the ${}^{10}\text{B}$ final states from deuteron-induced proton transfer reactions on ${}^9\text{Be}$	103
Chapter 7	APPLICATIONS	119
7.1	Reaction Rates	119
7.2	Fusion Diagnostics	122
7.2.1	Background	122
7.2.2	Monitoring plasma contamination	124
Chapter 8	SUMMARY AND CONCLUSIONS	126
8.1	Summary	126
8.2	Conclusions	128
8.3	Outlook	130
	REFERENCES	132
Appendix A	PULSE SHAPE DISCRIMINATOR ELECTRONICS	138
Appendix B	SELECT PROPERTIES OF BC-501A	140
Appendix C	SAMPLE KENT STATE NEUTRON DETECTION EF- FICIENCY CODE INPUT FILE	142
Appendix D	CHARGED PARTICLE AND NEUTRON DATA . . .	144

LIST OF FIGURES

1.1	Mass abundances expressed as fractions of total mass. Top axis is age of universe. Bottom axis is the corresponding temperature. [Reproduced from [1].]	2
2.1	Nuclear Reaction Cross Section vs Neutron Energy for select nuclear reactions used for neutron detection [2].	7
2.2	Velocity vectors before and after scattering [reproduced from Figure 1.21 in [3]].	9
2.3	Recoil energy spectrum for protons [reproduced from Figure 1.11 in [4]].	12
2.4	Figure of Merit [5, 6]	14
2.5	Comparison of effectiveness of one-dimensional (Time only) and two dimensional (Energy vs Time) pulse shape discrimination. Top: Projection of counts onto time axis, Bottom: Typical Energy (Vertical) - Time (horizontal) - Counts (color) graph.	15
3.1	Effect of electronics on time walk in zero-crossing method.	18
3.2	Block diagram of the pulse shape discriminator. [See Appendix A for greater detail.]	18
3.3	Basic Cockcroft-Walton Accelerator.	20
3.4	Example of the excellent ion species selection attainable with the 90 degree bending magnet. The beam current is directly proportional to the number of ions successfully passing through the magnet. [reproduced from [7]]	24
3.5	Colorado School of Mines Accelerator Schematic.	25
3.6	Schematic of scattering chamber on the Colorado School of Mines Accelerator.	26

4.1	Points used for gamma photon energy calibration. Channel of maximum counts is set equal to the Compton edge in one method and equal to the full energy of the photon in another method. The channel of 1/2-maximum is set equal to 104% of the Compton energy in a third method.	31
4.2	Gamma energy calibration for tube voltages from 700 to 900 volts. Results are for the method that uses the Compton edge as the full photon energy.	32
4.3	Gamma photon detection efficiency methods. Counts in the Upper Half-Width Half-Maximum [UHWHM - the striped section] are summed to determine the efficiency via the UHWHM method. In the modified UHWHM method, the counts at the (1/2-maximum + 1) channel are subtracted from each channel before summing.	33
4.4	Gamma photon detection efficiencies for sample of tube voltages using the modified Upper-Half-Width Half-Maximum method.	34
4.5	Calibration of time axis of pulse shape discriminator.	36
4.6	Integral efficiency curves predicted by Kent State detection code for uniform illumination and for point illuminations corresponding to various locations [hence angles] along the face of the detector. Only the point illumination corresponding to an angle of 1.25° produced a discernable difference from the uniform detector illumination.	40
4.7	Comparison of differential efficiency curve predicted by Kent State code to the measured spectrum for deuteron-induced proton transfer reactions on ⁹ Be. The first excited state is determined by subtracting the Kent State differential fit to the ground state from the measured spectrum.	41
5.1	Coulomb barrier	47
6.1	Typical neutron spectrum for the ² H(d,n) ³ He reaction.	56
6.2	Graphical representation of the method for determining the true neutron counts for the ² H(d,n) ³ He reaction.	57
6.3	Typical charged particle spectrum for the deuteron-induced reaction on deuterium.	59

6.4	Differential absolute cross sections for the ${}^2\text{H}(d,n){}^3\text{He}$ reaction in the center-of-momentum reference frame.	62
6.5	Comparison of measurements of the differential cross sections for the ${}^2\text{H}(d,n){}^3\text{He}$ reaction at an effective center-of-momentum energy = 40 keV.	63
6.6	Variation of the integrated cross section with energy for the ${}^2\text{H}(d,n){}^3\text{He}$ reaction in the center-of-momentum reference frame. Information regarding the cross section compilation by Arzamas can be found in reference [8].	65
6.7	Variation of the astrophysical S-factor with energy for the ${}^2\text{H}(d,n){}^3\text{He}$ reaction in the center-of-momentum reference frame.	66
6.8	Sample ${}^6\text{Li}(d,n){}^7\text{Be}$ neutron spectrum. Note the contribution (below channel 28) from the ${}^2\text{H}(d,n){}^3\text{He}$ reaction. The smooth curve is a best fit to the background neutrons from the ${}^7\text{Li}(d,n){}^8\text{Be}$ reactions. . . .	69
6.9	Sample charged particle spectrum for deuterons on ${}^6\text{Li}$	70
6.10	Curve fit to the ${}^6\text{Li}(d,p_0){}^7\text{Li}$ 90° differential cross section data provided in table VI of the paper by Elwyn, et. al. [9].	72
6.11	Differential cross section for the ${}^6\text{Li}(d,n){}^7\text{Be}$ reaction. Note that the distribution is isotropic to within the errors, indicating pure s-wave contribution to the cross section.	74
6.12	Variation of the integrated cross section with energy for the ${}^6\text{Li}(d,n){}^7\text{Be}$ reaction in the center-of-momentum reference frame. Information regarding the data of Guzhovich and of Qichang can be found in [10] and in [11] respectively.	75
6.13	Variation of the astrophysical S-factor with energy for the ${}^6\text{Li}(d,n){}^3\text{He}$ reaction in the center-of-momentum reference frame.	76
6.14	Typical charged particle spectrum for the deuteron-induced reactions on ${}^7\text{Li}$. Note the reaction peaks from the natural abundance of ${}^6\text{Li}$ in the target.	78
6.15	Typical neutron spectrum for the direct decay reaction. Neutrons from the sequential decay reaction are not discernable in the spectrum. . .	79

6.16	Graphical representation of the method for determining the direct decay reaction neutron count.	81
6.17	Differential cross section for the direct decay reaction ${}^7\text{Li}(d,n){}^8\text{Be}\rightarrow 2\alpha$	84
6.18	Differential cross sections for the direct decay reaction ${}^7\text{Li}(d,n){}^8\text{Be}\rightarrow 2\alpha$	85
6.19	Comparison of integrated cross sections for the direct decay reaction ${}^7\text{Li}(d,n){}^8\text{Be}\rightarrow 2\alpha$. Information regarding the data of Osetinskij and of Qichang can be found in references [12] and [11] respectively.	87
6.20	Variation of the astrophysical S-factor with energy for the direct decay reaction ${}^7\text{Li}(d,n){}^8\text{Be}\rightarrow 2\alpha$	88
6.21	Typical ${}^{10}\text{B}(d,n){}^{11}\text{C}$ neutron spectrum. Note the contribution from the ${}^2\text{H}(d,n){}^3\text{He}$ reaction and from the ${}^{11}\text{B}(d,n){}^{12}\text{C}$	90
6.22	Graphical representation of the method for determining the true neutron counts for the ${}^{10}\text{B}(d,n){}^{11}\text{C}$ reaction.	91
6.23	Typical charged particle spectrum for the deuteron-induced reactions on ${}^{10}\text{B}$	92
6.24	Differential cross section for the ${}^{10}\text{B}(d,n){}^{11}\text{C}$ reaction.	95
6.25	Variation of the integrated cross section with energy for the ${}^{10}\text{B}(d,n){}^{11}\text{C}$ reaction. Information regarding the data of Wohlleben and of Guzhovskij and of Anders can be found in references [13] and [14] and [15] respectively.	96
6.26	Variation of the astrophysical S-factor with energy for the ${}^{10}\text{B}(d,n){}^{11}\text{C}$ reaction.	97
6.27	Typical neutron spectrum for the ${}^{11}\text{B}(d,n){}^{12}\text{C}$ reaction. Note the presence of neutrons from the ${}^{10}\text{B}(d,n){}^{11}\text{C}$ reactions.	98
6.28	Graphical representation of the method for determining the direct decay reaction neutron count.	100
6.29	Typical charged particle spectrum for the deuteron-induced reactions on naturally occurring boron. Note the presence of reaction products from the ${}^{10}\text{B}$ in the target.	101

6.30	Differential cross section for the $^{11}\text{B}(\text{d},\text{n})^{12}\text{C}$ reaction.	104
6.31	Comparison of integrated cross sections for the $^{11}\text{B}(\text{d},\text{n})^{12}\text{C}$ reaction. Information regarding the data of Ames and of Class can be found in references [16] and [17] respectively.	105
6.32	Variation of the astrophysical S-factor with energy for the $^{11}\text{B}(\text{d},\text{n})^{12}\text{C}$ reaction.	106
6.33	Typical neutron spectrum for the deuteron-induced proton transfer reactions on ^9Be . Note the existence of the ^{10}B ground and 1st excited states.	108
6.34	Comparison of differential efficiency curve predicted by Kent State code to the measured spectrum for deuteron-induced proton transfer reactions on ^9Be . The first excited state shown in the graph is calculated by subtracting the differential curve of the Kent State code from the measured spectrum.	110
6.35	Typical charged particle spectrum for the deuteron-induced reactions on ^9Be	112
6.36	Differential cross section for the $^9\text{Be}(\text{d},\text{n})^{10}\text{B}$ reaction.	114
6.37	Comparison of integrated cross sections for the deuteron-induced proton transfer reactions on ^9Be . Information regarding the data of Devaney and of Koltay and of Bardes & Owen can be found in references [18] and [19].	115
6.38	Variation of the astrophysical S-factor with energy for the deuteron-induced proton transfer reactions on ^9Be	116
7.1	Nuclear reaction network.	123
7.2	Effect of contamination on the Bremsstrahlung radiation losses in a typical tokamak plasma [reproduced from [7]].	124
A.1	Pulse shape discriminator electronics details with pulse shapes. . . .	139
C.1	Sample input file for Kent State University Neutron Detector Efficiency code	143

LIST OF TABLES

1.1	Gamow peak energies and energy windows for the deuteron induced reactions.	5
2.1	Neutron Classification	6
4.1	Activities of γ sources	29
5.1	Energy relations for the deuteron-induced proton transfer reactions .	51
6.1	Experimental differential cross sections for the reaction ${}^2\text{H}(\text{d},\text{n}){}^3\text{He}$.	60
6.2	Experimental differential cross sections for the reaction ${}^6\text{Li}(\text{d},\text{n}){}^7\text{Be}$. The quoted errors do not include the 7.5% systematic error.	73
6.3	Experimental differential cross sections for the reaction ${}^7\text{Li}(\text{d},\text{n}){}^8\text{Be} \rightarrow 2\alpha$. Values include statistical error only. The systematic error was 7.5%.	83
6.4	Experimental differential cross sections for the reaction ${}^{10}\text{B}(\text{d},\text{n}){}^{11}\text{C}$. The quoted errors are purely statistical and do not include the 6.90% systematic error.	93
6.5	Experimental differential cross sections for the ${}^{11}\text{B}(\text{d},\text{n}){}^{12}\text{C}$ reaction. Values include statistical error only. The systematic error was 6.90%.	103
6.6	Experimental differential cross sections for the deuteron-induced proton transfer reactions on ${}^9\text{Be}$	113
6.7	Differential cross section coefficients in the center-of-momentum reference frame for the deuteron-induced proton transfer reactions	117
6.8	Integrated cross sections and astrophysical S-factors for the deuteron-induced proton transfer reactions. The relative errors apply to the cross sections and the S-factors.	118
B.1	Select properties of the organic liquid scintillator BC-501A	141
D.1	Charged particle monitor reactions for the ${}^2\text{H}$ and ${}^6\text{Li}$ reactions	145
D.2	Charged particle monitor reactions used for the ${}^7\text{Li}(\text{d},\text{n}){}^8\text{Be}$ reaction	146

D.3	Charged particle monitor reactions for ^9Be , ^{10}B , and ^{11}B	147
D.4	Range of sampled channels for determining counts from deuteron-induced proton transfer reactions on ^2H and on ^6Li	148
D.5	Range of sampled channels for determining counts from deuteron-induced proton-transfer reactions on ^7Li	149
D.6	Range of sampled channels for determining counts from deuteron-induced proton-transfer reactions on ^9Be , ^{10}B , and ^{11}B	150
D.7	True counts determined for deuteron-induced proton transfer reactions on ^2H and on ^6Li	151
D.8	True counts determined for deuteron-induced proton-transfer reactions on ^7Li	152
D.9	True counts determined for deuteron-induced proton-transfer reactions on ^9Be , ^{10}B , and ^{11}B	153

ACKNOWLEDGEMENTS

First among the many individuals, I wish to thank my advisor, Dr. Mariet Hofstee, and co-advisor, Dr. F. Edward Cecil. I have learned much from them over the course of conducting this research and preparing this dissertation. They not only have provided insights into aspects of the research but also have guided my continuing development as a professional scientist.

Other individuals aided in key areas of my research. Dr. Cynthia Galovich, from the University of Northern Colorado, spent countless hours in the laboratory with me. Her help in optimizing the electronics was much appreciated. I also wish to thank, Dr. Uwe Greife, a committee member and fellow member of the Colorado School of Mines nuclear group. He offered valuable insights and direction during the analysis of the data. Dr. James McNeil, also a member of the Colorado School of Mines nuclear group, provided helpful insights into understanding the results. Dr. B. D. Anderson, from Kent State University, provided the computer code that determined the neutron detector efficiency. He also provided additional insights, through personal communications, on the inner workings of that computer code. Eric Hawk, a graduate student member of the Colorado School of Mines nuclear group, deserves thanks for being the preliminary sounding board for many of my ideas.

Next, I want to thank all of my committee members. They have been patient with me as I worked out the details in this dissertation.

In addition to the individuals, there are some institutions which I wish to acknowledge. First, the Department of Energy provided the funding for this research. Second, Triangle Universities Nuclear Laboratories [TUNL] provided the computer facilities on which I ran the Kent State neutron detector efficiency code. [The code

was written for Vax/VMS platform which the Colorado School of Mines does not possess / support.] Running the code at TUNL saved valuable time and effort over porting it to a Linux platform. Lastly, I wish to acknowledge the efforts of the persons responsible for the National Nuclear Data Center[NNDC]. The work they do in collecting and organizing the wealth of information within nuclear physics is invaluable. Specifically, much of the experimental cross section data to which I compare my results was obtained from the Experimental Nuclear Reaction Data File on the NNDC website.

Finally, I wish to thank my parents. They have always supported me in my efforts and encouraged me to pursue my academic career.

Chapter 1

INTRODUCTION

A complete picture of nucleosynthesis requires knowledge of all possible reactions involved. The reactions that govern stellar evolution, the big bang, and fusion reactors occur at low energies. The Colorado School of Mines nuclear physics group actively pursues research at those low energies. The research on proton transfer reactions presented in this thesis complement the recently completed neutron transfer reaction research [7, 20].

1.1 Motivation

Nuclear reactions governed the evolution of the elements from the early universe to modern times. The fusion of neutrons with protons formed deuterons in the early universe. These deuterons opened other reaction channels which allowed the production (and destruction) of other light elements through lithium-7 (and possibly beryllium-9). The relative mass abundances of these light elements during this era of primordial nucleosynthesis is shown in Figure 1.1 [1]. Three of the possible reactions include ${}^2\text{H}(d,n){}^3\text{He}$, ${}^6\text{Li}(d,n){}^7\text{Be}$, and ${}^7\text{Li}(d,n\alpha){}^4\text{He}$. The first reaction provides a means for destruction of deuterium and the beginning of an alternative reaction chain that results in ${}^4\text{He}$. The second and third reactions participate in an alternative reaction network that results in the production of ${}^4\text{He}$ and in the production of and destruction of ${}^7\text{Li}$ [21].

A complete understanding of primordial nucleosynthesis requires precise knowledge of the primordial ${}^7\text{Li}$ and ${}^9\text{Be}$ abundances. Two competing models of primordial

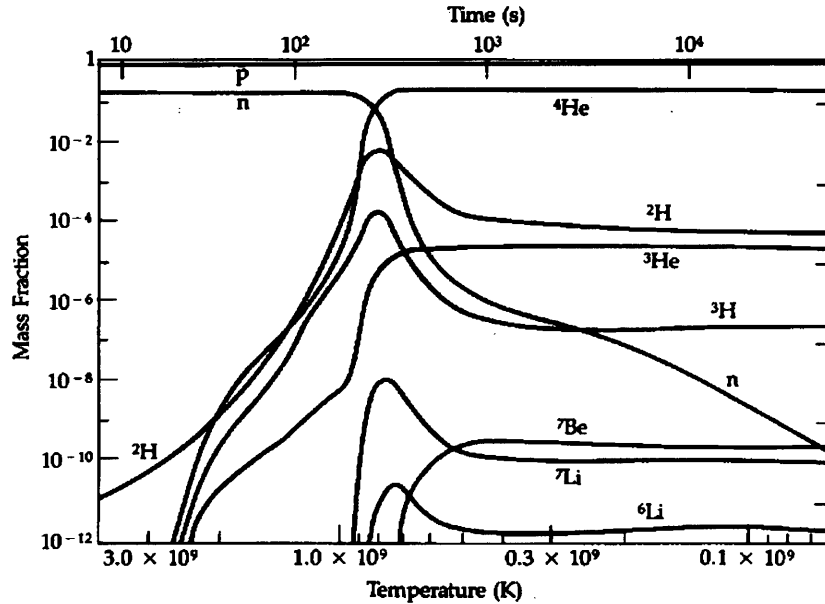


FIG. 1.1. Mass abundances expressed as fractions of total mass. Top axis is age of universe. Bottom axis is the corresponding temperature. [Reproduced from [1].]

nucleosynthesis are the homogeneous big bang nucleosynthesis (HBBN) and the inhomogeneous big bang nucleosynthesis (IBBN). The HBBN assumes a uniform baryon density. The IBBN assumes regions of high and low neutron to proton ratio. These regions formed during the phase transition of the universe from the quark-gluon plasma to hadrons. In the IBBN, nucleosynthesis occurred independently within these regions and later mixed to form the observed mass ratios [22]. The neutron-rich regions produced ${}^9\text{Be}$ in addition to the other elements. The ${}^9\text{Be}$ formed via reactions with ${}^7\text{Li}$. These neutron-rich regions also produced higher concentrations of deuterons. For this reason, knowledge of the deuteron-induced reactions on ${}^7\text{Li}$ and on ${}^9\text{Be}$ is important in determining the primordial abundances of ${}^7\text{Li}$ and ${}^9\text{Be}$ in the IBBN model [7].

Reaction network codes use cross section data as one input. These codes deter-

mine the time evolution of elemental abundances [21, 23]. The presence of ${}^9\text{Be}$ during nucleosynthesis in the big bang also opens reaction chains to heavier elements [21]. Deuteron-induced single-nucleon transfer reactions form chains that produce elements from ${}^{10}\text{B}$ to ${}^{16}\text{O}$. Three of these proton transfer reactions - ${}^9\text{Be}(d,n){}^{10}\text{B}$, ${}^{10}\text{B}(d,n){}^{11}\text{C}$, and ${}^{11}\text{B}(d,n){}^{12}\text{C}$ - complement the analog (d,p) reactions on the same target nuclei previously investigated by the Colorado School of Mines nuclear physics group [7].

These same three proton transfer reactions have applications in fusion reactor diagnostics. The inner walls of some tokamak fusion reactors are lined with beryllium or with boron. The power radiated by charged particles under acceleration, such as those in the tokamak, is proportional to the square of the charge [Z] of the particle. Contamination of the fusion plasma with beryllium [$Z=4$] or boron [$Z=5$] from the tokamak walls greatly increases the power loss. Measuring the contamination in the plasma requires knowledge of the ${}^9\text{Be} + d$ or ${}^{10,11}\text{B} + d$ reaction cross sections.

1.2 Energy Regime

Two important factors determine reaction rates between nuclei. First, particles in the plasmas of stars and tokamaks follow Maxwell-Boltzmann energy distributions. The Maxwell-Boltzmann distribution peaks at low energies. Second, the quantum mechanical probability for penetrating the Coulomb barrier increases with increasing energy. These competing terms produce a peak, known as the Gamow peak, in the reaction rate with a maximum at energy E_0 and a width of energy Δ .

$$\begin{aligned} E_0 &= 1.22 \left(Z_p^2 Z_t^2 \mu T_6^2 \right)^{1/3} \text{ (keV)} \\ \Delta &= 0.749 \left(Z_p^2 Z_t^2 \mu T_6^5 \right)^{1/6} \text{ (keV)} \end{aligned} \tag{1.1}$$

where temperature is designated by $T_n = T/10^n$ in Kelvin, Z_p and Z_t are the charges of the projectile and target nuclei, and μ is the reduced mass of the system. The energy windows of the Gamow peaks for environments of primordial nucleosynthesis ($T_9 \sim 0.60$), tokamaks ($T_9 = 0.12$), and massive stars (interiors at $T_6 \sim 60$) are given in Table 1.1.

1.3 Literature Search

Deuteron-induced proton-transfer reactions on the light nuclei in the present work have been investigated by others. These include but are not limited to [10, 14, 24, 11, 12, 19, 25]. Only a small number of these published experiments address the (d,n) reactions at energies comparable to those in this research. Most of those publications concentrate on the ${}^2\text{H}(d,n){}^3\text{He}$ reaction. The standard references for the ${}^2\text{H} + d$ reactions are the publications by Jarmie and Brown [26, 27]. A thorough reference for the ${}^6\text{Li} + d$ reactions is the paper by Elwyn, et al. [9]. The Elwyn paper covers laboratory energies as low as 204 keV for (d,n) and as low as 118 keV for (d,p) reactions. Hirst, et al. [28] measured the total cross section for the ${}^6\text{Li}(d,n){}^7\text{Be}$ down to an deuteron energy of 115 keV in the laboratory reference frame. Publications for the direct measurement of (d,n) reactions on ${}^7\text{Li}$ exist but only give the differential cross sections at 90° for energies comparable to those in this research. No publications were found that covered the (d,n) reactions on ${}^9\text{Be}$, ${}^{10}\text{B}$, and ${}^{11}\text{B}$ for energies comparable to those in this research.

Table 1.1. Gamow peak energies and energy windows for the deuteron induced reactions.

Target	T_6	E_0 keV	Δ keV
${}^2\text{H}$	6.0×10^2	8.70×10^1	1.55×10^2
	1.2×10^2	2.98×10^1	4.05×10^1
	6.0×10^1	1.87×10^1	2.77×10^1
	1.5×10^1	7.44×10^0	7.16×10^0
${}^6\text{Li}$	6.0×10^2	2.07×10^2	2.39×10^2
	1.2×10^2	7.08×10^1	6.25×10^1
	6.0×10^1	4.46×10^1	3.51×10^1
	1.5×10^1	1.77×10^1	1.11×10^1
${}^7\text{Li}$	6.0×10^2	2.10×10^2	2.40×10^2
	1.2×10^2	7.17×10^1	6.29×10^1
	6.0×10^1	4.52×10^1	3.53×10^1
	1.5×10^1	1.79×10^1	1.11×10^1
${}^9\text{Be}$	6.0×10^2	2.58×10^2	2.67×10^2
	1.2×10^2	8.83×10^1	6.98×10^1
	6.0×10^1	5.56×10^1	3.92×10^1
	1.5×10^1	2.21×10^1	1.23×10^1
${}^{10}\text{B}$	6.0×10^2	3.01×10^2	2.88×10^2
	1.2×10^2	1.03×10^2	7.54×10^1
	6.0×10^1	6.50×10^1	4.23×10^1
	1.5×10^1	2.58×10^1	1.33×10^1
${}^{11}\text{B}$	6.0×10^2	3.03×10^2	2.89×10^2
	1.2×10^2	1.04×10^2	7.56×10^1
	6.0×10^1	6.53×10^1	4.24×10^1
	1.5×10^1	2.59×10^1	1.34×10^1

Chapter 2

NEUTRON DETECTION

2.1 Neutron Interactions with Matter

Direct detection of neutrons by ionization techniques is impossible. Neutrons carry no electric charge; therefore, they interact very little with atomic electrons. Without the Coulomb interaction, neutrons produce no direct ionizations. Nuclear reactions [including scattering] between the neutrons and nuclei can produce energetic charged particles. These charged particles will produce ionizations which can be detected. The detection of the ionizations of the secondary particle indirectly provides detection of the neutrons [4].

Neutron energy ranges are classified according to the dominant interaction used to detect the neutrons [29]. [See Table 2.1.]

Nuclear reactions used to detect thermal and slow neutrons are less effective at higher energies. Neglecting any resonances, the nuclear reaction cross section depends on the

Table 2.1. Neutron Classification

Interaction	Neutron Energy	Classification
Hadron Shower	100+ MeV	High Energy
Scattering	1 - 100	Fast
Nuclear Reactions, (n,x)	eV - keV	Slow
Fission	Room Temperature	Thermal

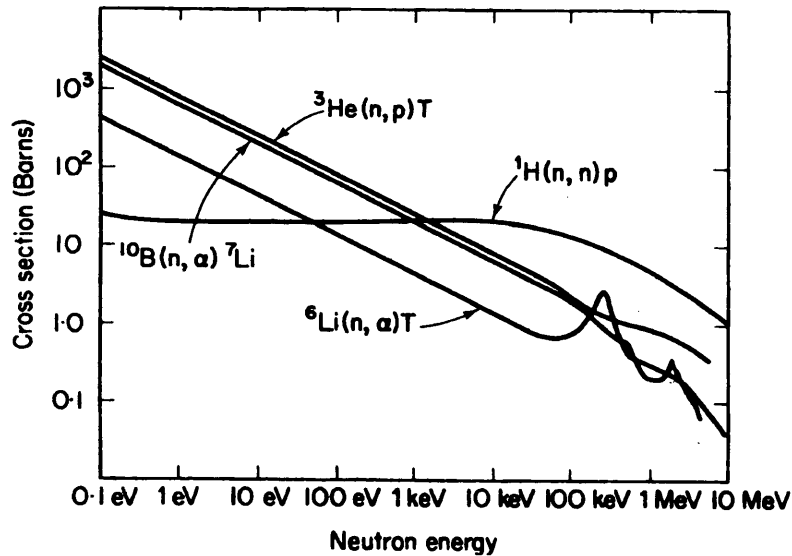


FIG. 2.1. Nuclear Reaction Cross Section vs Neutron Energy for select nuclear reactions used for neutron detection [2].

inverse of the neutron velocity ($\sigma \propto 1/v$) and, therefore, on the inverse square of the neutron energy [6]. At MeV energies, this energy dependence results in very low cross sections compared to scattering reactions as shown in Figure 2.1. Low cross sections produce low counts, so, these methods are not good for detection of higher energy neutrons [6]. The (d,n) reactions in this research produced neutrons with kinetic energies between 2 MeV and 15 MeV. As shown in Figure 2.1, neutron scattering from protons has the highest cross section; therefore, scattering with protons is the best method for detecting these fast neutrons.

For an ideal detector, all of the kinetic energy of the neutron would be transferred to the detector via the scattering processes. Consider a single scattering of the neutron from a nucleus in the detector in the center of momentum (CM) reference frame. In

the center of momentum reference frame, the relative speed after scattering, ρ between the neutron and nucleus can be expressed as

$$\rho^2 = |\vec{v}' - \vec{V}|^2 = v'^2 + V^2 - 2v'V \cos(\theta_L) \quad (2.1)$$

where

$\vec{v}' \equiv$ neutron velocity in laboratory (L) reference frame

$\vec{V} \equiv$ nucleus velocity in laboratory reference frame

θ_L lab angle between motions.

The center of momentum moves with respect to the lab reference frame with velocity, \bar{v} , given by

$$\bar{v}^2 = \left(\frac{A\vec{V} + \vec{v}'}{A+1} \right)^2 = \frac{(v'^2 + 2Av'V \cos \theta_L + A^2V^2)}{(A+1)^2} \quad (2.2)$$

where $A \equiv$ mass number of nucleus. Conservation of momentum and of kinetic energy determine the relation between the motions of the neutron and the nucleus. The magnitudes of the velocities in the center of momentum reference frame must remain unchanged by the scattering. Let \vec{v} and \vec{u} be the velocity vectors of the neutron after scattering in the laboratory and the center of momentum reference frames respectively. The velocity of the nucleus in the center of momentum is then $-\vec{u}/A$ with magnitude $u = A\rho/(A+1)$. For isotropic scattering, the velocity vector of the neutron can terminate with equal probability anywhere on the sphere of radius u which is centered about the center of momentum [3].

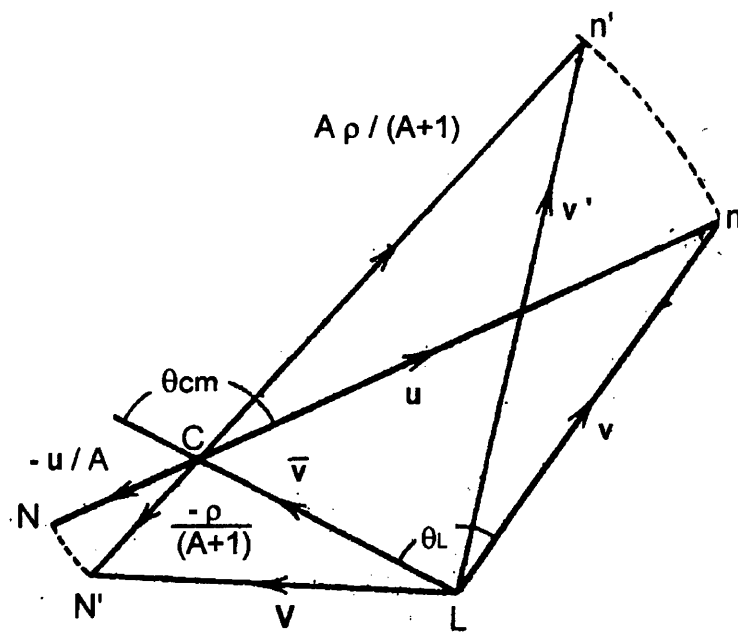


FIG. 2.2. Velocity vectors before and after scattering [reproduced from Figure 1.21 in [3]].

A neutron with energy on the order of 10 MeV is non-relativistic. The kinetic energy of the neutron is directly proportional to the square of the neutron velocity. Nuclei of solid targets have little motion compared to the motion of the MeV neutron ($V \ll v'$). To a good approximation, these nuclei can be treated as stationary. Equations 2.1 and 2.2 reduce to $\varrho \approx v'$ and $\bar{v} = v'/(A + 1)$ with this stationary nucleus approximation [3]. Applying the transformation geometry [see Figure 2.2] between the laboratory and center of momentum reference frames to the results of the non-relativistic neutron and stationary target approximations yields two important relations. The first is the relation between the scattering angle of the neutron in the laboratory and in the center of momentum reference frames:

$$\cos \theta_L = \frac{A \cos \theta_{CM}}{\sqrt{A^2 + 1 + 2A \cos \theta_{CM}}}. \quad (2.3)$$

The second is the relation between the ratio of the incident energy, E' , to the scattered energy, E of the neutron in the laboratory reference frame and the scattering angle of the neutron in the center of momentum reference frame:

$$\frac{E}{E'} = \left(\frac{v}{v'}\right)^2 = \frac{A^2 + 1 + 2A \cos \theta_{CM}}{(A + 1)^2}. \quad (2.4)$$

Isotropic scattering means that all scattering angles are equally probable. The probability to scatter into a solid angle, $d\omega$ is directly proportional to the cosine of the azimuthal angle in the center-of-momentum reference frame:

$$\begin{aligned} P(d\omega) &= \frac{d\omega}{4\pi} = \frac{\sin \theta_{CM} d\theta_{CM} d\phi_{CM}}{4\pi} \\ &\propto \sin \theta_{CM} d\theta_{CM} \\ &\propto -d \cos \theta_{CM} \end{aligned} \quad (2.5)$$

where

$d\omega \equiv$ differential solid angle and
 $\phi_{CM} \equiv$ center of momentum azimuthal angle.

Differentiating equation 2.4 yields the relation

$$\begin{aligned} d\left(\frac{E}{E'}\right) &= d\left[\frac{A^2 + 1 + 2A \cos \theta_{CM}}{(A + 1)^2}\right] \\ \frac{dE}{E'} &= \frac{2A}{(A + 1)^2} d \cos \theta_{CM} \\ dE &= \frac{2AE'}{(A + 1)^2} d \cos \theta_{CM} \propto P(d\omega). \end{aligned} \quad (2.6)$$

Since $P(d\omega)$ is equal for all $d\omega$, all allowed scattered neutron energies are equally probable [30]. The range of possible energies of the scattered neutron is found by applying the bounds on the cosine in equation 2.4.

$$\left(\frac{A - 1}{A + 1}\right)^2 E' \leq E \leq E'. \quad (2.7)$$

Conservation of energy requires that the recoiling nucleus carries the energy difference, $E_r = E' - E$; therefore,

$$0 \leq \frac{E_r}{E'} \leq \frac{4A}{(A + 1)^2}. \quad (2.8)$$

As seen in equation 2.8, protons ($A=1$) provide the largest maximum value of recoil energy. Since the ionizations produced by the recoil nuclei are what is directly detected, protons are the best neutron detector material. A detector consisting only of protons would have a single-valued response to mono-energetic neutrons that undergo scattering only once before exiting the detector. Multiple scattering of the neutrons

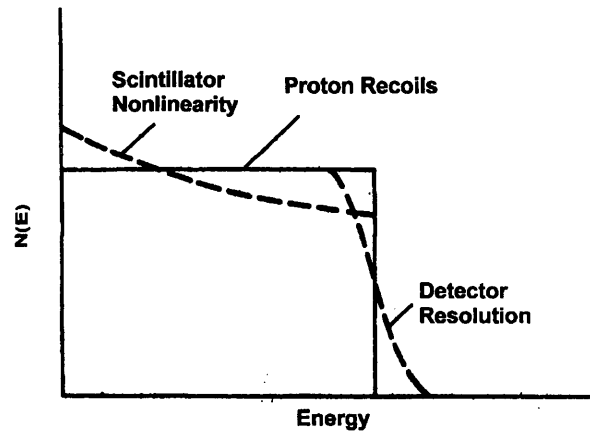


FIG. 2.3. Recoil energy spectrum for protons [reproduced from Figure 1.11 in [4]].

within the detector, finite energy resolution of the detector, and other non-linear effects distort the real detector spectrum [4]. [see Figure 2.3]

2.2 Pulse Shape Discrimination

Neutrons from reactions of interest are often accompanied by a high background of γ photons. Pulse shape discrimination is a method for separating the signal of the recoil protons due to neutrons from the signal of the Compton electrons produced by γ photons. Different particles have different specific ionizations within a scintillator. The specific ionization determines the time evolution of the fluorescence of the scintillator. Measuring the shapes of the fluorescent pulses produced by particles forms the basis of the pulse shape discrimination (PSD) technique [31].

Two common methods of pulse shape discrimination exist. Both methods exploit the fact that the fluorescent pulses contain “fast” and “slow” components with decay

constants of τ_f and τ_s . The photomultiplier current is given by

$$I(t) = I_f \exp(-t/\tau_f) + I_s \exp(-t/\tau_s). \quad (2.9)$$

The pulse shape depends on the amplitudes, I_f and I_s , and on the decay time constants, τ_f and τ_s . The first method of PSD measures the ratio of the charge produced by either the fast or the slow component to the total charge produced in the pulse [32, 33]. The second method measures a characteristic time of the pulse. The time may either be the time to reach maximum (the rise time) or the time to decay from that maximum to a fixed percentage (constant fraction) of that maximum [31, 29].

Although the amplitudes of the pulses vary with energy for any given species, both the charge ratio and the timing methods of PSD are ideally independent of pulse amplitudes. In practice, results do vary with varying pulse amplitude. The variations are generally acceptable over a large dynamic range of pulse amplitudes (100:1 or more). The variations produce distributions in the time measured in the timing methods of PSD. For any given particle species, the distribution is centered about a given time, t , and has a certain full width - half maximum, W . The effectiveness of the PSD technique to separate particle species "a" from particle species "b" is measured by the figure of merit, M [6, 5]:

$$M = \frac{t_b - t_a}{W_b + W_a} = \frac{T}{W_b + W_a}. \quad (2.10)$$

The parameters t_a , t_b , W_a , W_b , and T are shown in Figure 2.4. Since pulse amplitude is related to the energy of the incident particle, a large dynamic range is desirable for PSD. A value of $M \geq 1.5$ will theoretically allow complete separation of species "a" and "b" [5]. The energy range over which $M \geq 1.5$ defines the dynamic range.

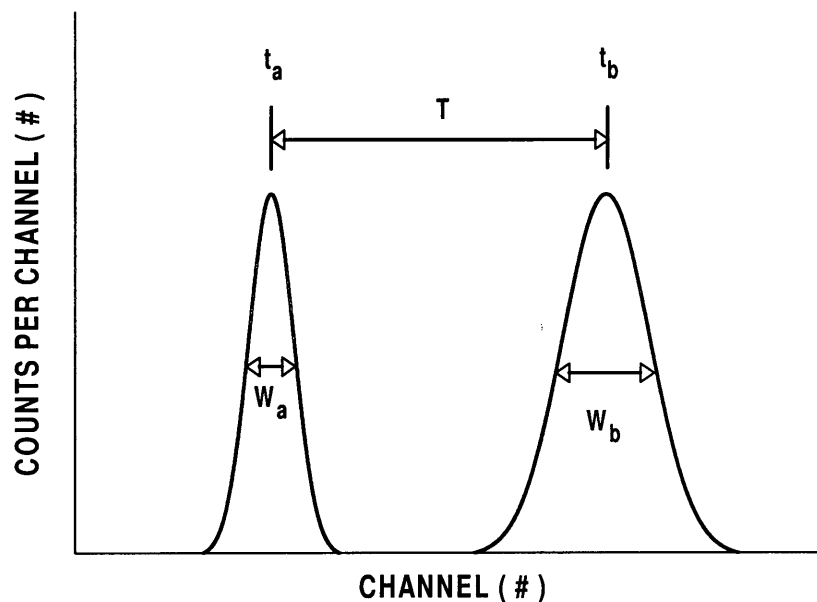


FIG. 2.4. Figure of Merit [5, 6]

Compton electrons generally produce a larger ratio of the fast decay component to the slow decay component than do recoil protons. Observations indicate that this difference in ratio decreases nonlinearly with increasing recoil proton energy [34, 35, 36]. As a result, the separation between neutrons and gamma's decreases with increasing neutron energy as measured by the fluorescent decay time method. This effectively limits the dynamic range of the PSD system [36]. The upper limit on the dynamic range can often be extended by collecting a multidimensional spectrum [29]. Recording the amplitude (energy) and the timing information of an event produces a marked improvement in the neutron - γ separation. [See Figure 2.5.] Notice that in the projection onto the time axis some of the neutrons are incorrectly identified as gammas.

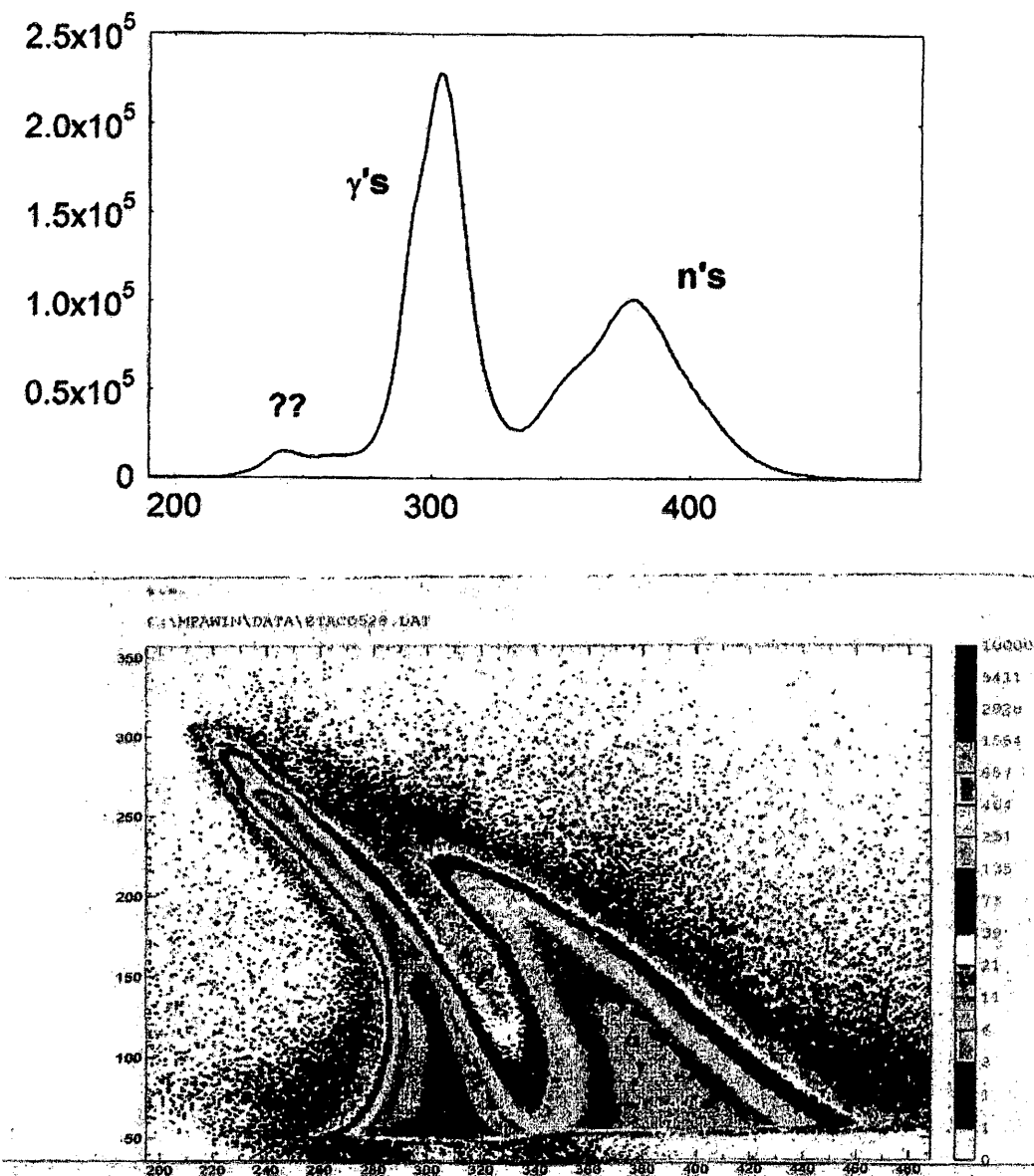


FIG. 2.5. Comparison of effectiveness of one-dimensional (Time only) and two dimensional (Energy vs Time) pulse shape discrimination. Top: Projection of counts onto time axis, Bottom: Typical Energy (Vertical) - Time (horizontal) - Counts (color) graph.

Chapter 3

INSTRUMENTATION

3.1 The Pulse Shape Discriminator

Neutrons and γ photons produced scintillations in a 6" x 6" cylindrical detector filled with the organic liquid scintillator Bicron BC-501A. A photomultiplier collected the scintillation light. The anode signal typically is used to measure the scintillation decay times. A plutonium - beryllium source produces neutrons of energy within the planned operational energy range of the detector. Tests with the plutonium - beryllium source indicated that better energy resolution was attainable with no effect on the timing resolution when energy was measured from the anode signal. The anode signal was connected to an Ortec 571 Amplifier and then delayed an appropriate time to arrive at the analog to digital converter (ADC) within the same gated interval as the timing signal.

The dynode signal was amplified before entering into an Ortec 552 Pulse Shape Analyzer (PSA). The PSA was set to the zero-crossing mode. In the zero-crossing mode, the PSA divides the signal into two signals. The leading edge of the first separated signal triggers a pulse in the "START" branch of the timing electronics. This pulse arrives at an Ortec 566 Time-to-Amplitude-Converter (TAC) that begins storing charge. The second signal in the PSA is first integrated and then doubly differentiated. The zero-crossing time of the resulting bipolar pulse is proportional to the decay time of the original signal produced by the neutron or γ . The zero-crossing triggers a pulse in the "STOP" branch of the timing electronics. This pulse stops the

storage of charge in the TAC. The total charge stored by the TAC is then proportional to the decay time of the original scintillation event in the detector. This charge is converted to a voltage by the TAC [6]. The voltage is then sent to input one of the ADC. [Input one corresponds to the horizontal axis in two dimensional plots.]

Incident particle energy is not the only factor that can affect the timing measurements. The detection electronics can also affect the measurements. Three common effects due to the electronics are :

1. a shift in the photomultiplier gain with particle energy,
2. signal pile-up at high count rates, and
3. time walk in the signal due to finite thresholds of the electronics [see Figure 3.1].

The effect of time walk is greatest for small amplitude (low energy) pulses [29]. The zero-crossing of two pulses due to the same type but different energy particles is shown in Figure 3.1. Note the difference in the time of the crossing. The smaller pulse takes longer to cross.

A charged particle monitor was fixed at a lab angle of 90 degrees. The particle monitor, a silicon surface barrier (SSB) detector, provided the reference to determine the relative cross sections used to calculate the absolute deuteron-induced proton transfer cross sections. The signal from the SSB was independently collected at input three of the ADC. a schematic of the electronics appears in Figure 3.2.

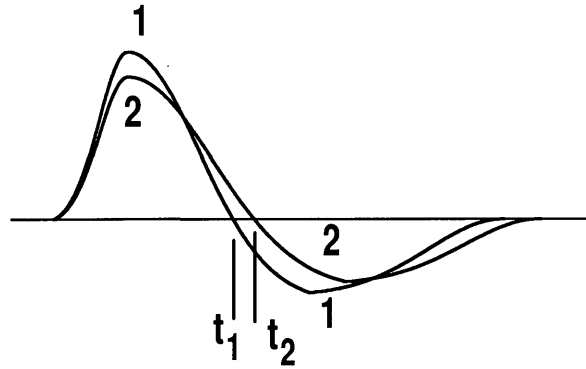


FIG. 3.1. Effect of electronics on time walk in zero-crossing method.

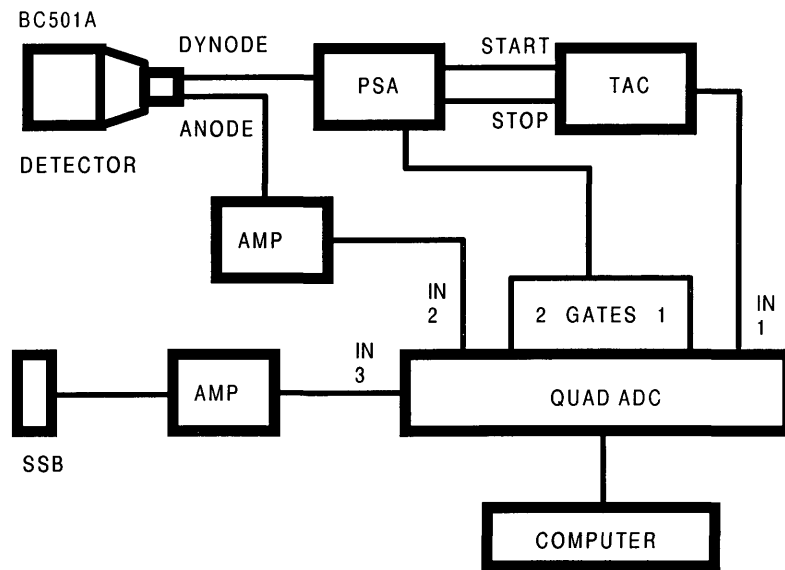


FIG. 3.2. Block diagram of the pulse shape discriminator. [See Appendix A for greater detail.]

3.2 Accelerator

3.2.1 Requirements

All accelerators have three common traits :

1. production of projectiles (an ion source),
2. energy transfer to the projectiles (acceleration), and
3. transport of projectiles to the target (beam steering and focusing).

When a particle of charge q passes through a voltage difference ΔV , the energy of that particle increases by the amount $E = q\Delta V$. The basic electrostatic accelerator consists of an ion source and of the mechanism to produce a large electrostatic potential difference through which the ion is accelerated [4].

3.2.2 Cockcroft-Walton Design

Schenkel and Greinacher designed a voltage multiplier circuit that transformed a high frequency alternating current into a high-potential constant-voltage source. In the design, a transformer of maximum voltage $\equiv u$ drives two capacitors. Two rectifiers switch the capacitors between charging in parallel and discharging in series. One point in the circuit reaches a steady-state potential of twice the maximum transformer voltage ($2u$). On the opposite side of a rectifier from the steady-state potential, the voltage varies between zero and twice the maximum transformer voltage. The time-varying voltage across that rectifier serves as the source for another set of capacitor-rectifier pairs. This second stage then feeds a third and so on. [see Figure 3.3] The stacking of stages produces a final terminal voltage, V_{out} , equal to the

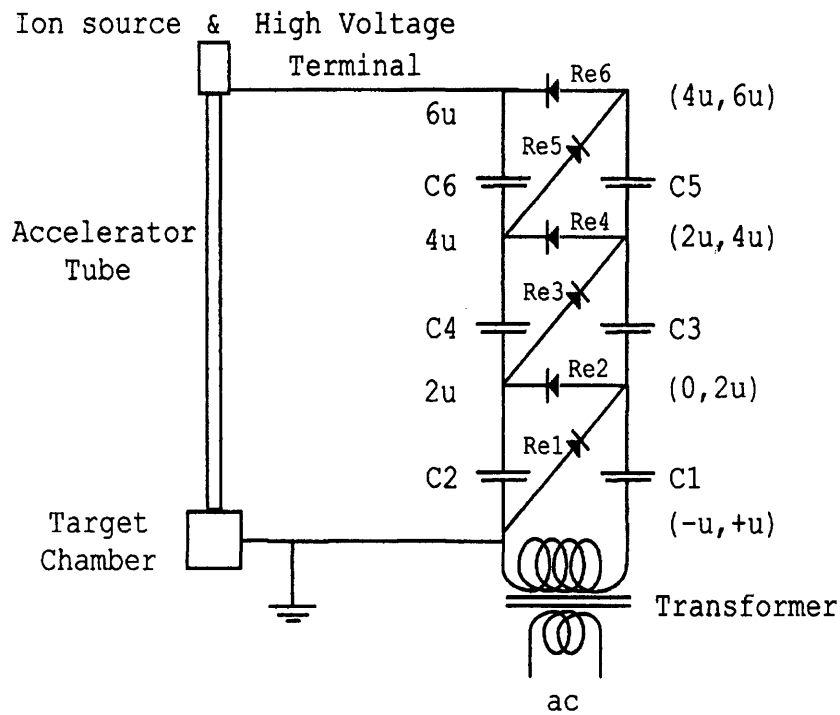


FIG. 3.3. Basic Cockcroft-Walton Accelerator.

number of stages, n , times twice the maximum transformer voltage [34]:

$$V_{out} = 2un. \quad (3.1)$$

Cockcroft and Walton used this voltage multiplier design as the high voltage source for the accelerator named for them. When connected to an external load, such as in an accelerator, the performance of the voltage multiplier is affected. The true voltage obtained is less than the ideal voltage under no-load conditions [equation 3.1]. The actual voltage at the terminal depends on the transformer frequency, f , on the number of capacitors, N , on the value of each capacitor, C , and on the current

drain, i , of the load [4, 37]:

$$V_{out} = Nu - \frac{i}{fC} \left(N^3 + \frac{9}{4}N^2 + \frac{1}{2}N \right) = 2nu - \frac{i}{fC} (8n^3 + 9n^2 + n).$$

Differentiating the terminal voltage with respect to the number of stages yields the optimum number of stages:

$$\begin{aligned} \frac{dV_{out}}{dn} &= 2u - \frac{i}{fC} (24n^2 + 18n + 1) = 0 \\ 2u &= \frac{i}{fC} \left(2n^2 + \frac{3}{2}n + \frac{1}{12} \right) \\ u &\approx \frac{in^2}{fC} \\ n_{opt} &= \sqrt{\frac{fCu}{i}}; n \gg 1 \end{aligned} \quad (3.2)$$

Converting alternating current into direct current results in a variation, ΔV , in the terminal voltage:

$$\Delta V = n(n+1) \left(\frac{i}{2fC} \right). \quad (3.3)$$

This ripple voltage and the deviation from the no-load condition are minimized by using a high frequency transformer and large-valued capacitors. Typical transformer frequencies range from 0.5 to 10 kHz. Capacitances range from 10^{-9} to 10^{-3} Farads [34]. The General Ionex Model 1545 accelerator at the Colorado School of Mines provides a very stable beam with a total voltage variation of approximately 20 V at an operating voltage of 150 kV [38].

3.2.3 Accelerator Details

The Colorado School of Mines accelerator uses a duoplasmatron gas source. A valve releases gas into the source chamber. Electrons are released from the filament. These electrons receive a boost in energy from a 100 to 150 volt potential. The energetic electrons collide with the gas atoms, ionizing the gas. The magnetic field which constrains the electrons produces more collisions per electron, increasing ionization efficiency. The ions are extracted by a 20 kV potential [38].

An Einsel lens focuses the extracted ions before they pass through a 90° bending magnet. The 90° magnet is tuned to select only ions with the desired charge to mass ratio. [see Figure 3.4] Contaminants in the system will be deflected out of the beam. The ions then pass through the acceleration column which is attached to the high voltage source. A gridded lens provide a final focusing of the ions.

The ions pass through a 30° bending magnet before entering the target chamber. The 30° magnet serves two purposes. First, the magnet provides one last filter to contaminants in the beam. At the pressures of 10^{-6} to 10^{-7} Torr maintained in the accelerator, some atmospheric atoms and molecules remain in the accelerator. There is a small yet finite chance that the projectile ions may ionize these remaining atmospheric particles through collisions. The ionized atmospheric particles would be accelerated through the remaining of the accelerating column. Tuning the 30° magnet deflects these contaminants out of the beam before they reach the target. Second, solid targets are used for these experiments. Ions striking these targets liberate electrons from the targets. These secondary electrons would travel along the beam in a direction opposite to the direction of the ions and affect accelerator performance. The 30° magnet bends these electrons out of the beam. A schematic of the accelerator is shown in Figure 3.5.

The accelerator is brought to operating vacuum pressures in two stages. First, a mechanical roughing pump evacuates the accelerator to a pressure on the order of 10^{-3} Torr. Two turbomolecular pumps then take the accelerator down to its operational pressure range of 10^{-6} to 10^{-7} Torr where it is maintained [38].

Two target chambers were used. The target was positioned in the first target chamber before the chamber was sealed and brought down to vacuum. The second chamber had a transparent top and a target holder that was rotatable via a handle that passed through the transparent top. The SSB detector was mounted inside the chambers. The neutron detector was placed outside the chambers since neutrons could pass through the chamber walls. A schematic of the second chamber is shown in Figure 3.6.

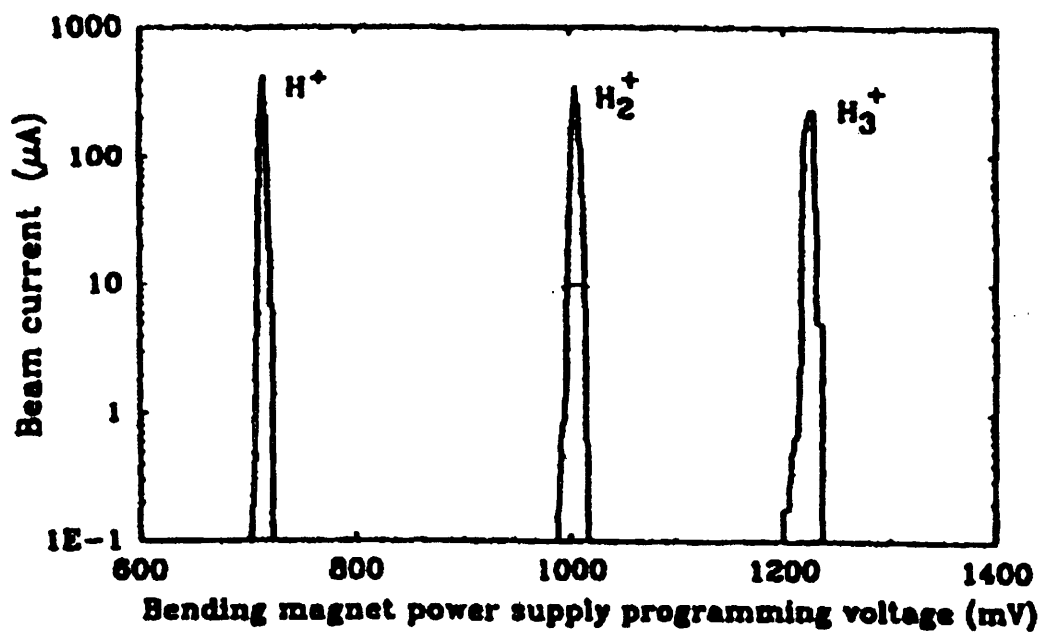


FIG. 3.4. Example of the excellent ion species selection attainable with the 90 degree bending magnet. The beam current is directly proportional to the number of ions successfully passing through the magnet. [reproduced from [7]]

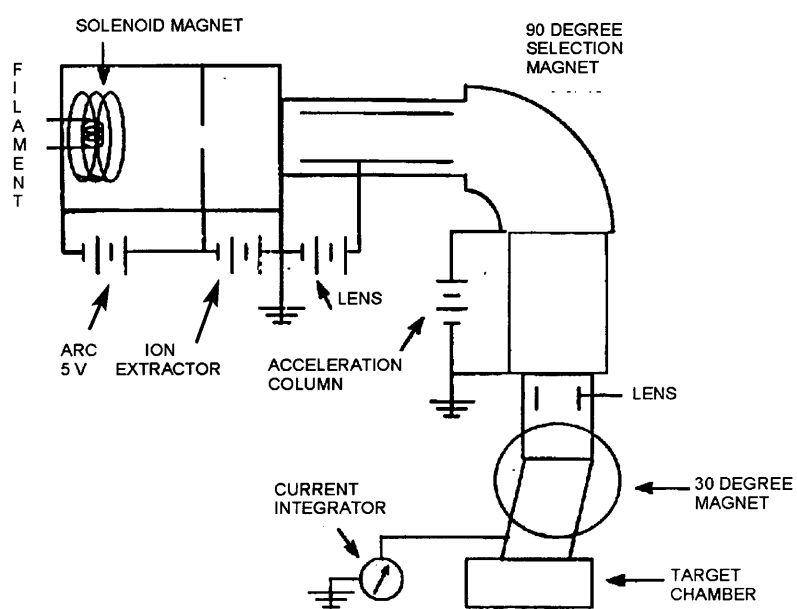


FIG. 3.5. Colorado School of Mines Accelerator Schematic.

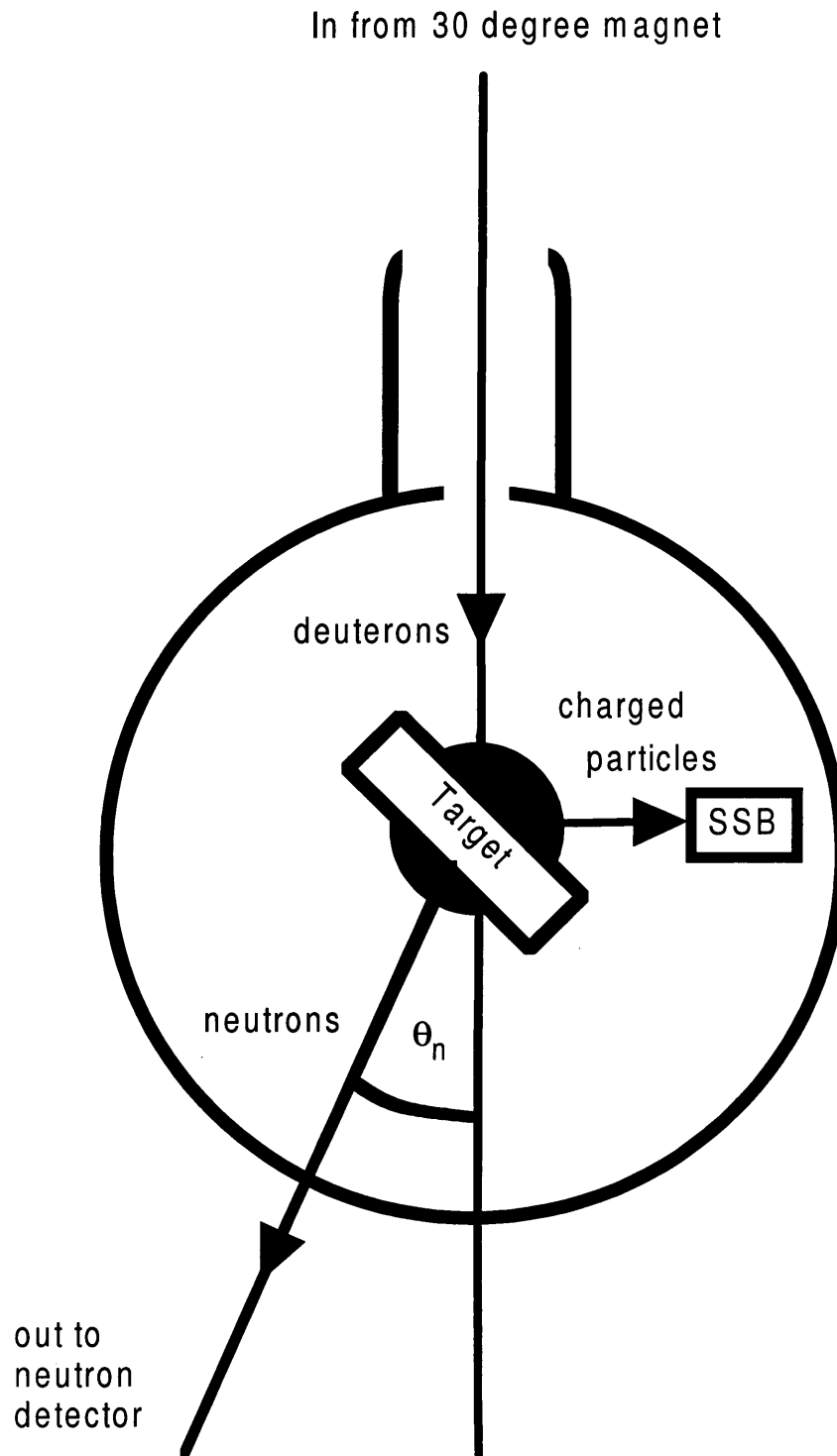


FIG. 3.6. Schematic of scattering chamber on the Colorado School of Mines Accelerator.

Chapter 4

THE DETECTOR

Bicron BC-501A provides excellent neutron- γ separation when used for pulse shape discrimination. This liquid scintillator was deoxygenated with nitrogen gas and sealed in an aluminum 6" x 6" cylindrical detector.

4.1 Response of Bicron BC-501A to MeV photons

Liquid scintillators easily fill large volume or odd shaped detectors. This advantage often outweighs the disadvantage that these scintillators produce no well-defined peaks. Extracting useful results from the raw data requires understanding the response of the BC-501A to radiations. An organic liquid scintillator is typically characterized by the response of the scintillator to MeV photons. The response of the BC-501A was measured for photons from 0.6 MeV to 2.7 MeV [see Table 4.1] for photomultiplier tube voltages from 700 to 900 volts.

4.1.1 Data collection

The sources listed in Table 4.1 provided the photons. Each source was placed at a known distance from the detector. The solid angle was determined. Isotropy of the source was assumed. The time of and activity at production of each source was known. From that information, the activity at the time of data collection was calculated [4]:

$$A = A_0 \exp(-\lambda t) \quad (4.1)$$

where

$$\begin{aligned}
 A &\equiv \text{Activity at time } t, \\
 A_0 &\equiv \text{Initial activity (} t=0 \text{)}, \\
 \lambda &\equiv \text{decay constant} &= \ln 2/t_{1/2}, \\
 t_{1/2} &\equiv \text{half-life.}
 \end{aligned}$$

For example, consider the ^{137}Cs source with a half-life of $t_{1/2} = 30.17$ years and initial activity, $A_0 = 1.34 \mu\text{Ci}$, on 01 March 1973. Then

$$\begin{aligned}
 A &= A_0 \exp(-\lambda t) \\
 &= (1.34 \mu\text{Ci}) \exp\left(\frac{-26.15 \text{ years} \cdot \ln(2)}{30.17 \text{ years}}\right) \\
 &\approx 0.735 \mu\text{Ci}.
 \end{aligned}$$

The true count rate, R , for photons entering the detector was then calculated for the known activity, A , and solid angle, $d\Omega$:

$$R = \frac{d\Omega}{4\pi} A. \quad (4.2)$$

For the ^{137}Cs example with the source at the face of the detector,

$$\begin{aligned}
 R &= \frac{2\pi}{4\pi} (0.735 \mu\text{Ci}) (3.7 \times 10^{10} \text{ disintegrations / second}) \\
 &= 13598 \text{ counts/second.}
 \end{aligned}$$

Data collection periods lasted 300 seconds for each combination of source, distance, and photomultiplier tube voltage. The measured counts were used to calibrate the energy and decay time responses of the detector-electronics combination and to calculate efficiencies for measuring γ photons.

Table 4.1. Activities of γ sources

Source	γ - energy (MeV)	A_0 μ Ci)	Date	A (μ Ci)
^{137}Cs	0.662	1.34	01 Feb 1973	0.735
^{207}Bi	0.570	0.10	19 Jan 1990	0.085
^{60}Co	1.17	0.800	12 Aug 1992	0.337
	1.33			
^{22}Na	1.27	1.0	Jan 1991	0.10
^{40}K	1.46	background		
^{214}Bi	1.12	background		
	1.24			
^{208}Tl	2.61	background		

4.1.2 Energy calibration

Different methods exist to calibrate the energy response of liquid scintillators. In one method, the channel of maximum counts in a spectrum is taken as the Compton edge energy. An uncertainty in the exact position of the Compton edge, due to finite detector resolution, exists. In a second calibration method, the channel of 1/2-maximum counts [the upper half-width half-maximum channel] is set to 104% of the Compton edge energy to lessen the effect of the finite detector resolution [39]. [See Figure 4.1.] This method yielded nonlinear results over the energy range of interest. The method chosen for calibration of the BC-501A used the channel of maximum counts at the Compton edge as the full photon energy. Calibration by this method produced very linear results for all photomultiplier tube voltages.[See Figure 4.2.]

Varying the photomultiplier tube voltages from 700 to 900 volts produced changes in the slopes and intercepts of the energy calibration curves. An increase in the photomultiplier tube voltage resulted in a lower low-end cut-off energy and a smaller energy per channel. [See Figure 4.2]

4.1.3 γ -Efficiency

Birks [33] defines the γ -efficiency of a liquid scintillator as the number of counts in the upper-half width-half maximum (UHWHM) of the Compton edge divided by the true number of counts. [See Figure 4.3.]

The efficiency measured with this technique changed with photon energy. One variation on the technique of Birks multiplies the number of channels in the UHWHM of the Compton edge by the number of counts at the channel that is one channel beyond the UHWHM channel. The number of counts from that multiplication is then subtracted from the total number of counts under the UHWHM of the Compton edge. The resulting counts are then divided by the true number of counts to determine the efficiency. This variation produced consistent efficiency within the energy range of interest for each tube voltage. [See Figure 4.4]

4.1.4 Time axis calibration

Calibration of the time axis was done by measuring the time interval between the start and stop signals from the pulse shape analyzer. Using a γ source, the time interval between the start and stop was measured on an oscilloscope and the corresponding channel on the time axis recorded. A delay was introduced in the stop signal and the time interval between the start and delayed stop signals measured. The corresponding channel on the time axis was recorded for this stretched time interval.

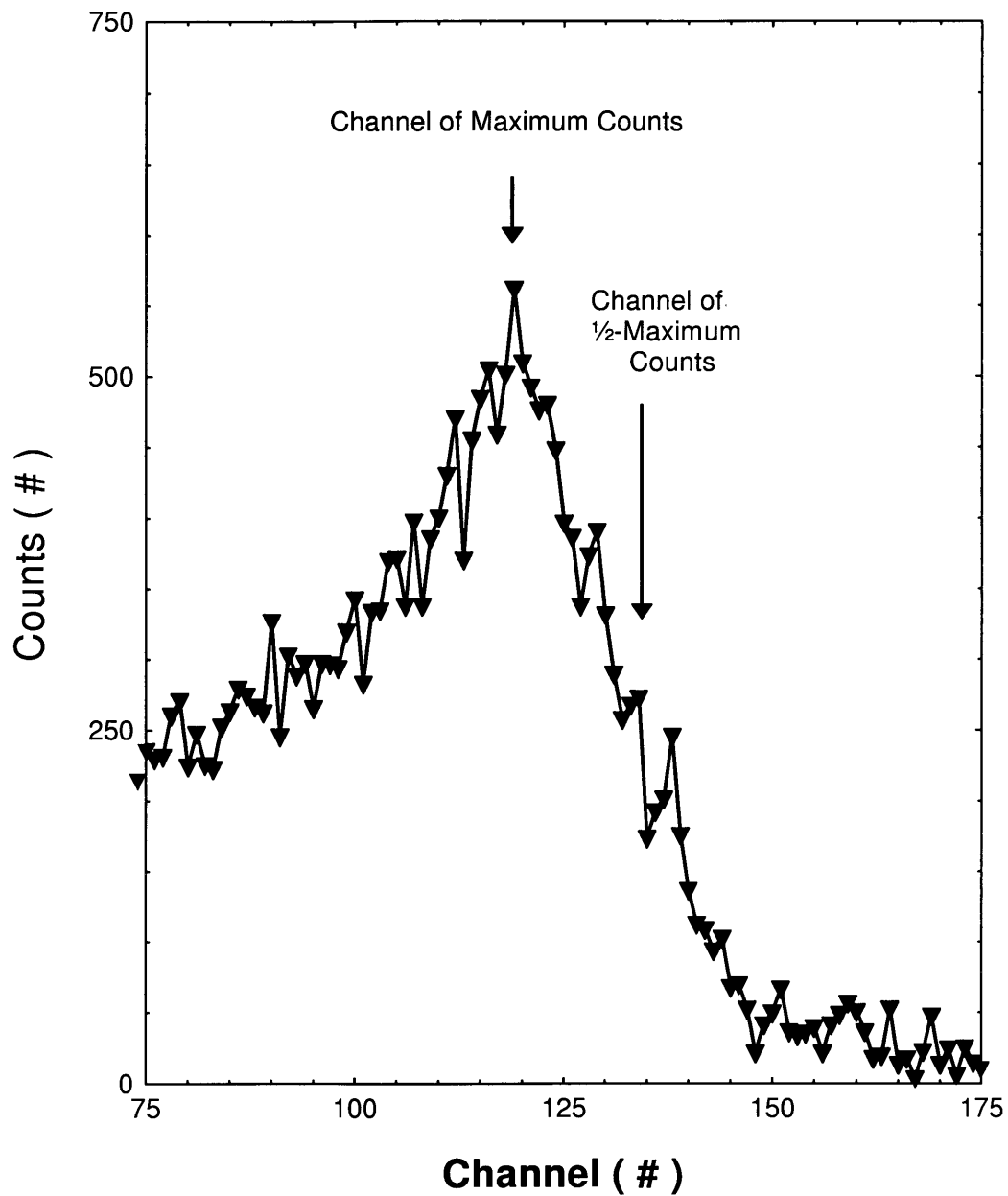


FIG. 4.1. Points used for gamma photon energy calibration. Channel of maximum counts is set equal to the Compton edge in one method and equal to the full energy of the photon in another method. The channel of 1/2-maximum is set equal to 104% of the Compton energy in a third method.

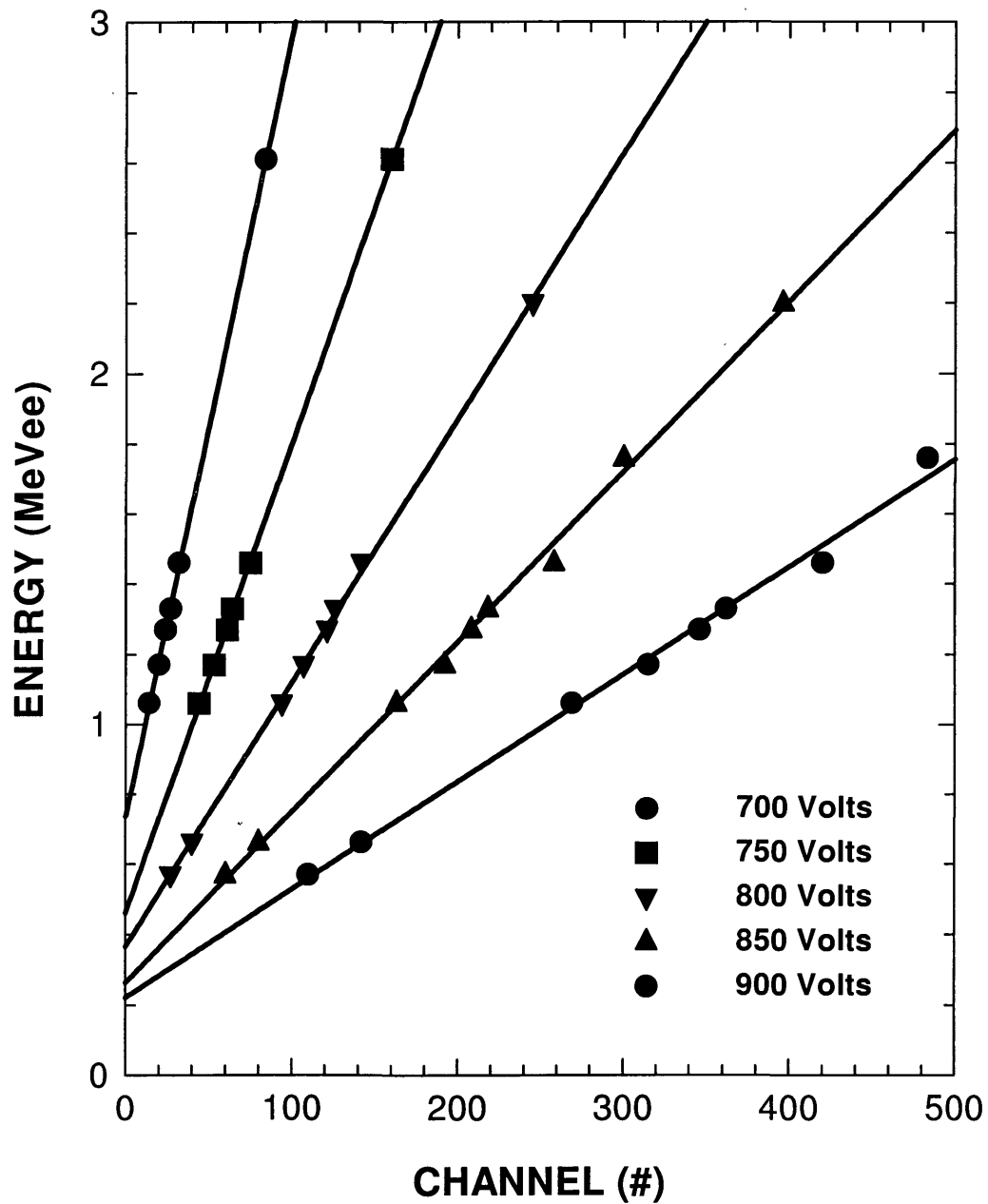


FIG. 4.2. Gamma energy calibration for tube voltages from 700 to 900 volts. Results are for the method that uses the Compton edge as the full photon energy.

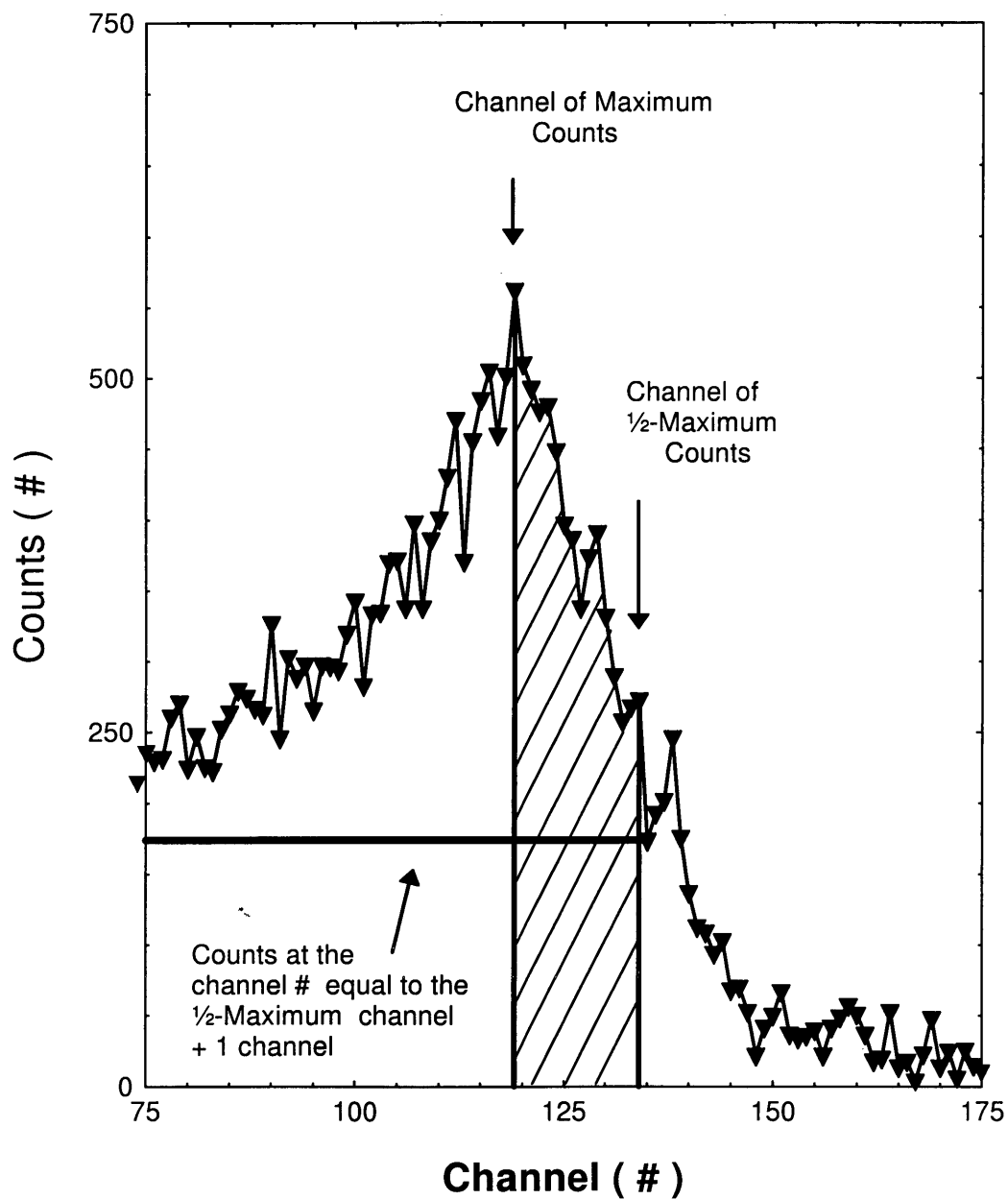


FIG. 4.3. Gamma photon detection efficiency methods. Counts in the Upper Half-Width Half-Maximum [UHWHM - the striped section] are summed to determine the efficiency via the UHWHM method. In the modified UHWHM method, the counts at the (1/2-maximum + 1) channel are subtracted from each channel before summing.

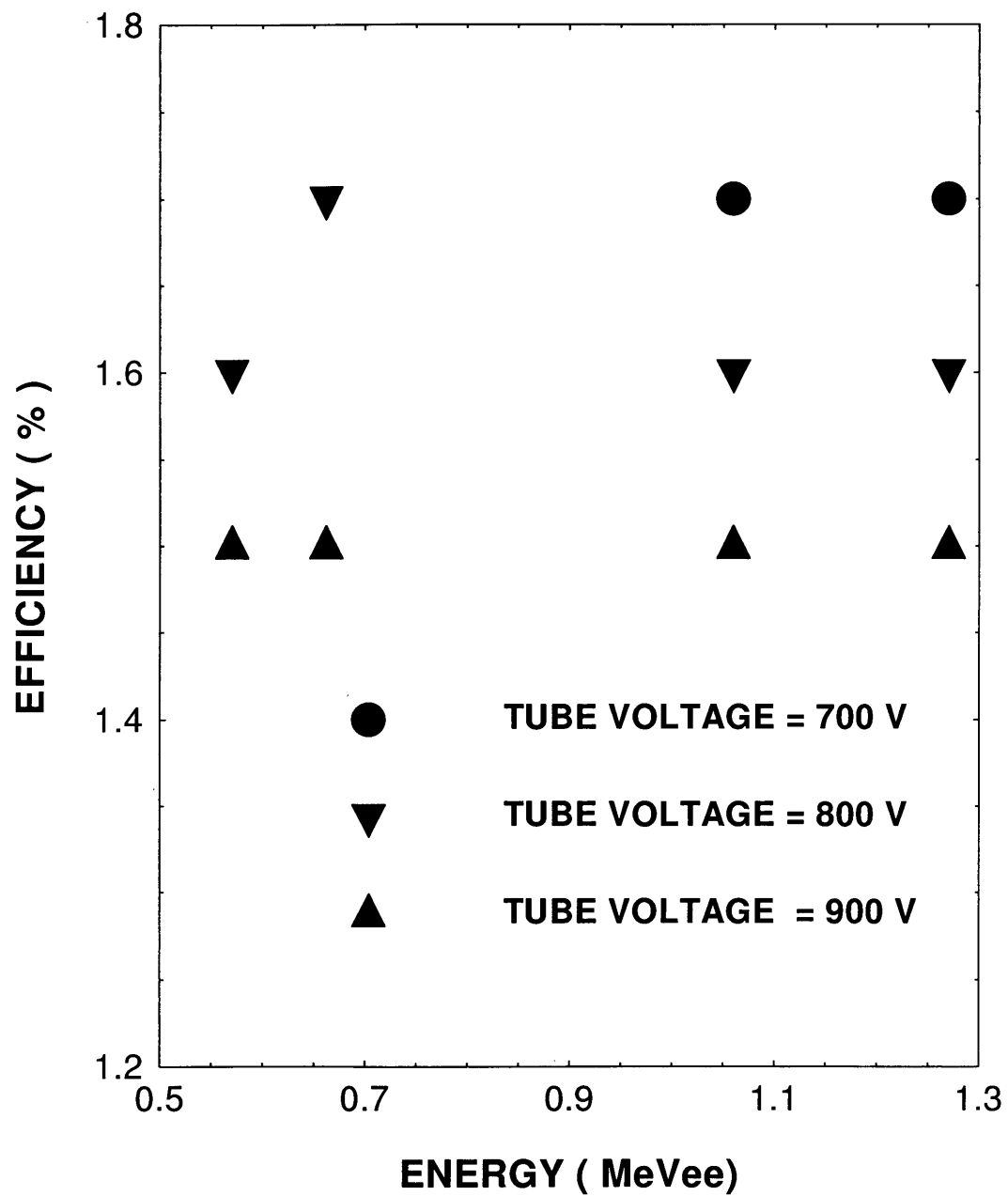


FIG. 4.4. Gamma photon detection efficiencies for sample of tube voltages using the modified Upper-Half-Width Half-Maximum method.

The delayed stop signal process was repeated a second time. The calibration was calculated with a linear curve fit to the three data points for time vs channel. [See Figure 4.5.]

4.2 Response of BC-501A to neutrons

The same techniques used to measure the response of BC-501-A to photons can be applied to neutrons. Unlike the linear energy response to photons, BC-501A does not respond linearly to neutrons. Recall that neutrons result in recoil protons and that γ photons result in Compton electrons within the detector. These charged particles produce the scintillations that the photomultiplier tube detects. The recoil proton energy, E_p [MeV], required to produce the same light in BC-501A as an electron of given energy, E_e [MeV], is defined as the electron-equivalent energy [MeVee].

$$E_e = a_1 E_p - a_2 \left[1.0 - \exp \left(-a_3 E_p^{a_4} \right) \right], \quad (4.3)$$

where $a_1 = 0.83$, $a_2 = 2.82$, $a_3 = 0.25$, and $a_4 = 0.93$ [40]. More recent results [41] give the following values for the coefficients for BC-501A: $a_1 = 0.81$, $a_2 = 2.80$, $a_3 = 0.20$, and $a_4 = 1.0$. The nonlinear energy response of BC-501A to neutrons requires a large number of calibration energies to determine a functional form for the efficiency. The number of available sources and the relative high cost of standard neutron sources restrict the useful range of the modified UHWHM efficiency determination technique.

An alternative to the modified UHWHM technique is to model the interactions within BC-501A. The Kent State University Neutron Detection Efficiency code uses Monte Carlo simulations of neutron interactions with scintillators to determine efficiencies. Five improvements over previous codes were incorporated into the Kent State code [42].

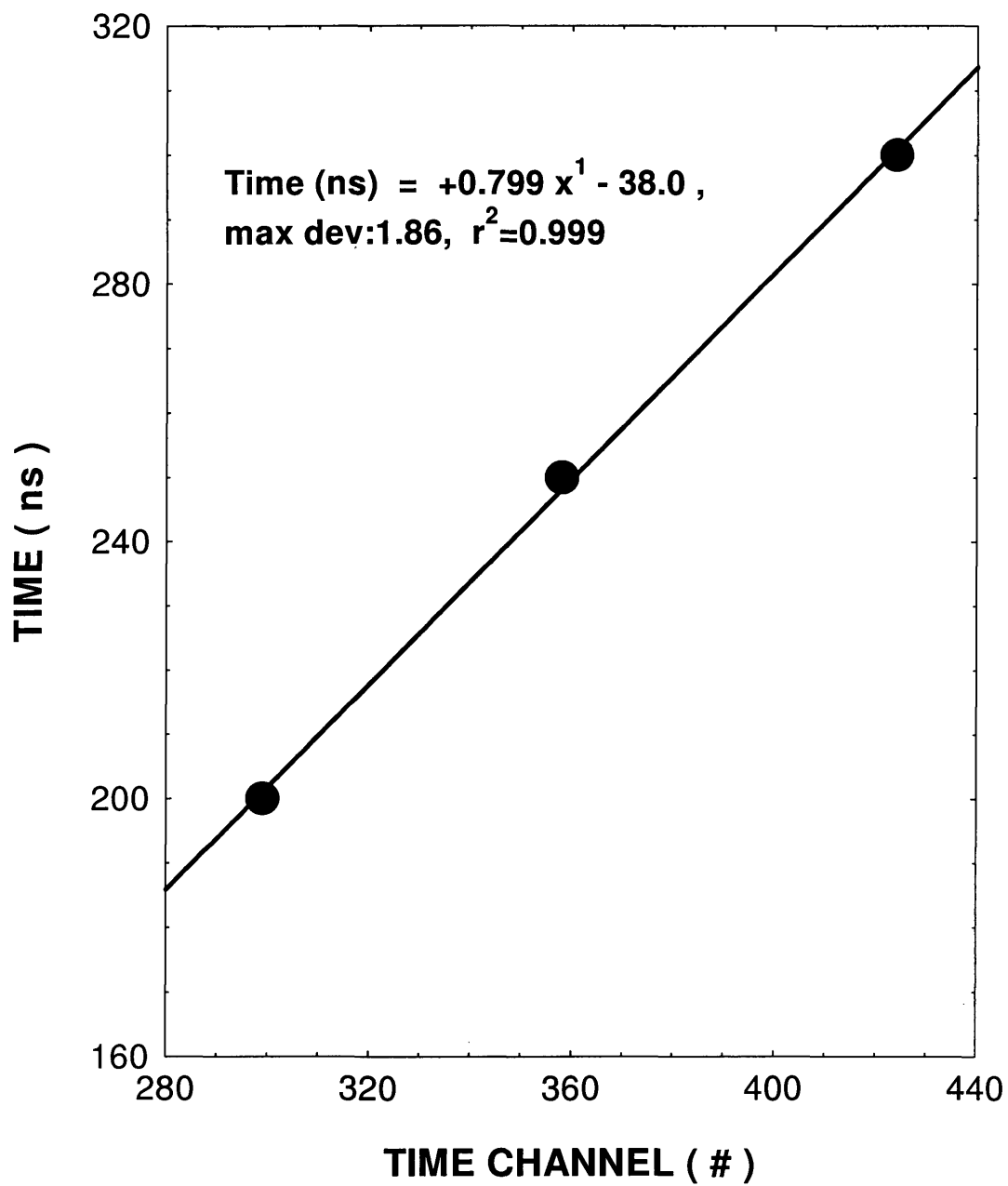


FIG. 4.5. Calibration of time axis of pulse shape discriminator.

1. Improvements in inelastic scattering cross sections and kinematics.
2. Use of relativistic kinematics for all reaction channels.
3. Finite detector sizes accounted for.
4. Incorporation of better light response functions.
5. Incorporation of multiple scattering of a neutron within detector.

The Kent State code was chosen for these improvements and the flexibility of the code to accommodate different scintillators. The code can calculate efficiencies for rectangular and cylindrical detectors.

The Kent State code requires information about the physical properties of the detector and about the response of the detector to γ 's. The code uses the physical detector size, scintillator density, and the hydrogen to carbon ratio to determine the mean free paths of neutrons and recoil protons, which reaction channel occurs, and whether or not the particles escape from the detector after a collision.

The light output coefficients for protons and for α 's determine the scintillation light produced by and the electron equivalent energies [recall equation 4.3] for those particles. These coefficients are user determined parameters that are specific to the scintillator. The values listed earlier from reference [41] were used in all of the calculations for the BC-501A detector. The electronics of the pulse shape discriminator affect the detector efficiency. The binwidth [energy / channel] and the bias [low energy cut-off], measured in electron equivalent MeV [MeVee], are the user determined parameters that account for the effect of the electronics [43]. The choice and performance of the photomultiplier tube that is coupled to the detector will also affect efficiency. The number of photoelectrons released at the cathode per keV characterizes the performance of the photomultiplier tube [6, 29]. The Kent State code requires

the inverse of this parameter - the energy [in MeVee] required to release one photoelectron - as input. This one photoelectron level determines the quantum statistics in the Kent State code and becomes important for small signals [low energies] [44].

The Kent State code models the neutron flux at the detector as either uniform or a point illumination. The illumination point is chosen by the rectangular Cartesian coordinates (x,y,z) with reference to the center of the illuminated portion of the detector as (0,0,0). The direction cosines are chosen to match the angle of incidence of the neutrons. The cylinder may be illuminated from the side or on the face. The neutrons can have a distribution of energies. The distribution is modeled as a Gaussian of width ΔE_n about the central energy, E_n [43].

Typical settings [see Appendix C] for uniform illumination of the detector face with monoenergetic neutrons from the reaction ${}^6\text{Li}(d,n){}^7\text{Be}$ at zero degrees produced the integral efficiency curve of Figure 4.6. An integral efficiency represents the percent of neutrons incident on the BC-501A detector that deposit energy between the corresponding channel for the given efficiency and the channel corresponding to the actual neutron energy [the “maximum” channel]. Subtracting the integral efficiency at channel (n-1) from that at channel n produces the differential efficiency curve. The differential efficiency for the reaction ${}^9\text{Be}(d,n_0){}^{10}\text{B}$ agrees well with that portion of the measured ${}^9\text{Be}(d,n_0+n_1){}^{10}\text{B}$ spectrum to which the (d,n₁) reaction channel does not contribute. [See Figure 4.7.]

The angle subtended by the detector varied from ± 10 degrees to ± 15 degrees as viewed from the target. To test the effects of nonuniform illumination on the calculated efficiencies, point illumination calculations were performed for the ${}^6\text{Li}(d,n){}^7\text{Be}$ reaction at the same deuteron energy ($E_{d,lab} = 145$ keV) as for the uniform illumination example. [Point illumination is the flux of neutrons arriving at a single location

on the surface of the detector.] The errors attributed to each efficiency calculation were purely statistical [42]. The energy spread for the neutrons, ΔE_n , was assumed to be negligible for all the calculations. As seen in Figure 4.6 for different point illuminations over the face of the detector, only the point illumination corresponding to an angle of incidence of 1.25° on the detector face produced results distinguishable from the uniform illumination case.

The preliminary results indicated that the Kent State Neutron Detection Efficiency code produced accurate efficiency values for the $6'' \times 6''$ cylindrical BC-501A detector.

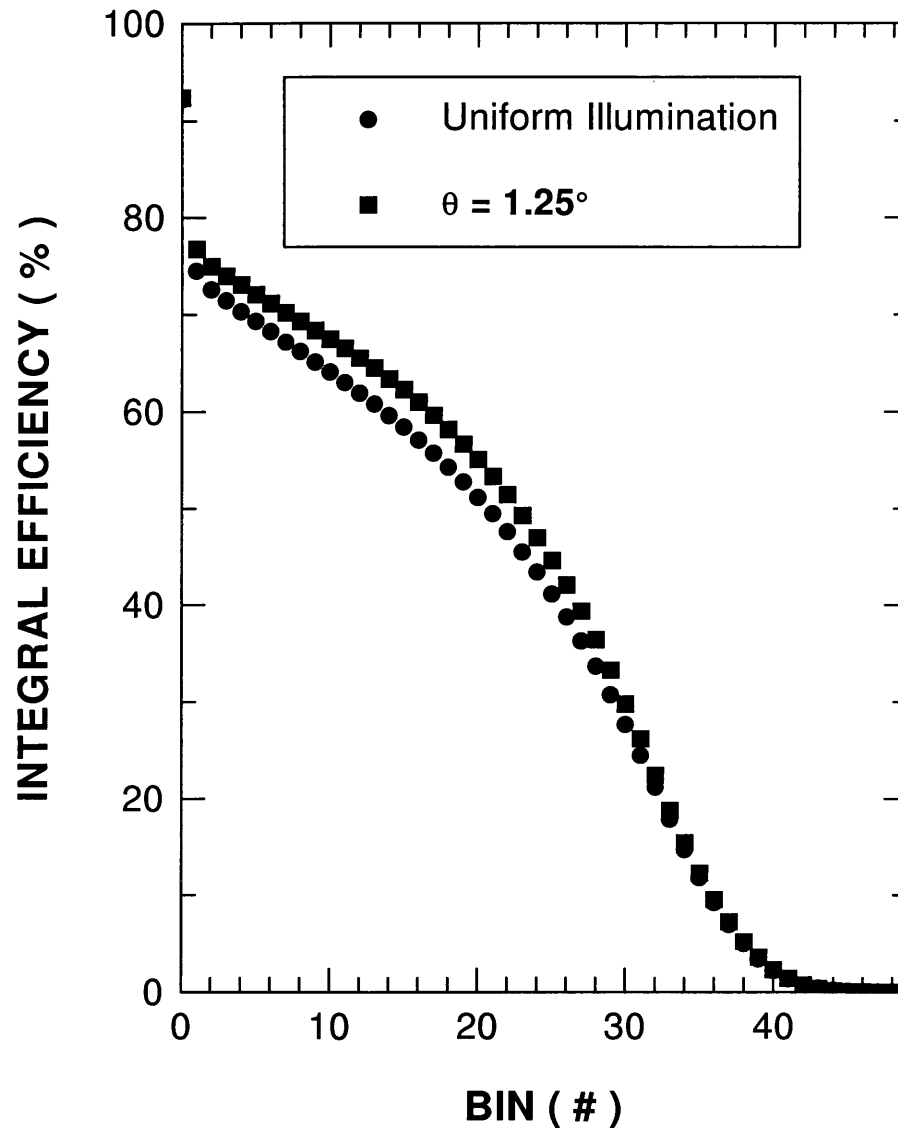


FIG. 4.6. Integral efficiency curves predicted by Kent State detection code for uniform illumination and for point illuminations corresponding to various locations [hence angles] along the face of the detector. Only the point illumination corresponding to an angle of 1.25° produced a discernable difference from the uniform detector illumination.

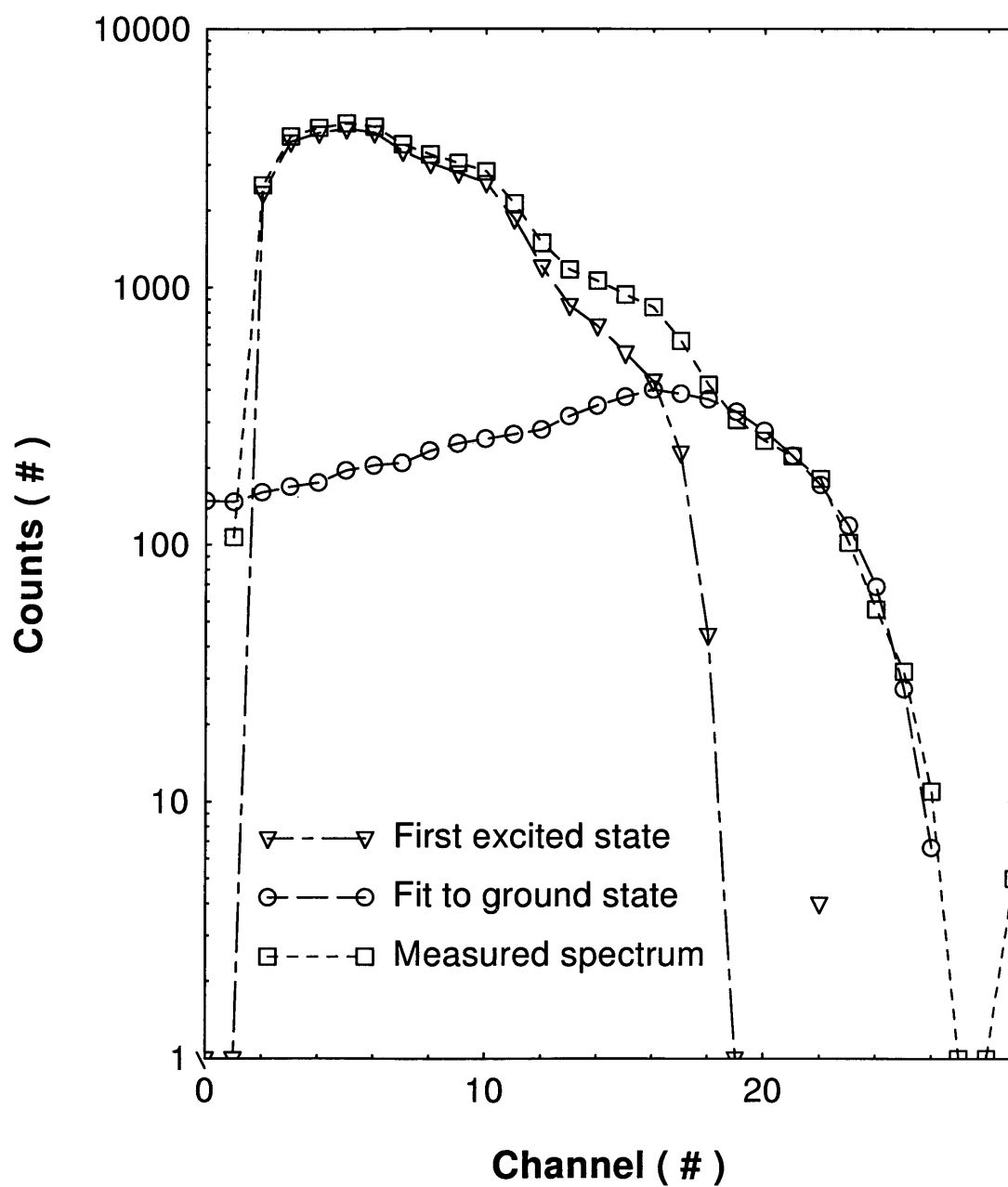


FIG. 4.7. Comparison of differential efficiency curve predicted by Kent State code to the measured spectrum for deuteron-induced proton transfer reactions on ${}^9\text{Be}$. The first excited state is determined by subtracting the Kent State differential fit to the ground state from the measured spectrum.

Chapter 5

THEORY OF REACTIONS AND CROSS SECTIONS

5.1 Reaction Yields

Detectors count the number of particles that enter them. For any given reaction, the number of detected product particles can be expressed as the yield per incident projectile, ΔY . For thin targets, this yield can be expressed in terms of the reaction cross section [37]:

$$\Delta Y = \sigma n \Delta x \quad (5.1)$$

where

- $\sigma \equiv$ cross section for reaction,
- $n \equiv$ number of active nuclei per unit volume,
- $\Delta x \equiv$ target thickness.

A charged particle loses energy via collisions with the material it is penetrating. The two main collision mechanisms are

1. inelastic collisions with atomic electrons and
2. elastic collisions with nuclei.

The linear stopping power, SP, equals the average energy loss of a projectile per unit length penetration into a target:

$$SP = \left| \frac{dE}{dx} \right| = -\frac{dE}{dx}. \quad (5.2)$$

Bragg's rule weights the effect of each element in a target on the stopping power [29]. The subscripts "a" and "i" in the following equation refer to the "active" element [the element participating in the reaction of interest] and to the "inactive" elements [all other elements in the target].

$$\frac{1}{\rho_a} \frac{dE}{dx} = \frac{w_a}{\rho_a} \left(\frac{dE}{dx} \right)_a + \sum_i \frac{w_i}{\rho_i} \left(\frac{dE}{dx} \right)_i \quad (5.3)$$

where

$\rho_i \equiv$ mass volume density of element i,

$w_i \equiv$ weighting factor for element i,

$$= \frac{n_i A_i}{\rho_i \sum_j n_j A_j},$$

$n_i \equiv$ number of element i, and

$A_i \equiv$ Atomic mass number of element i.

The masses are approximated by the equivalent mass numbers. The stopping cross section, ε , equals the stopping power divided by the number of nuclei, n :

$$\varepsilon = SP/n. \quad (5.4)$$

Application of equation 5.4 to the effective stopping power produces the effective stopping cross section.

$$\varepsilon_{eff} = \varepsilon_a + \sum_i \left(\frac{n_i}{n_a} \right) \varepsilon_i \quad (5.5)$$

If the target thickness is expressed in energy units, Δ_{eff} , the thin target yield can be expressed as

$$\Delta Y = \frac{\sigma \Delta_{eff}}{\varepsilon_{eff}} \quad (5.6)$$

where

$$\Delta_{eff} = \Delta x \cdot SP = \Delta x \varepsilon_{eff} n .$$

For thick targets, the energy loss of the projectile is non-negligible. Integration of the thin target yield gives the thick target yield, $Y(E_0)$ [45]:

$$Y(E_0) = \int_{E_0-\Delta}^{E_0} \frac{\sigma(E)}{\varepsilon(E)} dE . \quad (5.7)$$

The targets used for this research were sufficiently thick to stop all of the projectiles ($\Delta = E_0$).

The measured yield is defined as the measured number of counts per incident projectile. Three factors primarily affect the measured yields.

1. A detector is not 100% efficient. ($\eta < 1$)
2. A detector occupies a finite solid angle, $d\Omega$.
3. The reaction products exit the target with some angular distribution, $W(\theta, \phi)$.

The measured yield, Y_m and thick target yield are related by

$$Y_m = n_d \eta \frac{d\Omega}{4\pi} W(\theta, \phi) Y(E_0) \quad (5.8)$$

where n_d is the number of incident projectiles.

5.2 Nonresonant Cross Sections and the Astrophysical S-Factor

The cross section for a given reaction is a measure of the relative probability for that reaction to occur for a given flux of incident projectiles on a target of known areal density [4]. Classically, the projectile and target must make physical contact for a reaction to occur. Rutherford approximated nuclear radii by $r_n = r_0 A^{1/3}$ where $r_0 = 1.2 \times 10^{-13}$ cm. The hard sphere approximation of nuclei results in nuclei with circular apparent geometric areas. The sum of the apparent geometrical areas of the projectile and target nuclei defines the classical cross section, σ_{cl} [37]:

$$\begin{aligned} \sigma_{cl} &= \pi (r_t^2 + r_p^2) \\ &\approx 10^{-24} \text{ cm}^2 \\ &\equiv 1 \text{ barn.} \end{aligned} \quad (5.9)$$

Due to the nature of matter, the reaction cross sections must be explained via quantum mechanics. DeBroglie originally proposed standing waves to explain the stability of Bohr orbitals for atomic electrons. This wave concept has been extended to all matter [46]. The deBroglie wavelength is given by

$$\lambda = \frac{h}{p} \quad (5.10)$$

where

$h \equiv$ Planck constant and

$p \equiv$ particle momentum.

Quantum mechanical interactions are proportional to the square of the deBroglie wavelength; therefore, the cross section is directly proportional to the square of the deBroglie wavelength, $\sigma \propto \pi\lambda^2$. Energy is directly proportional to the square of the momentum for nonrelativistic particles; therefore, the cross section is inversely proportional to the energy [47]:

$$\begin{aligned}\sigma &\propto \pi\lambda^2 \\ \sigma &= \pi h^2 \left(\frac{1}{p^2} \right) \\ \sigma &\propto \frac{1}{E}.\end{aligned}\tag{5.11}$$

Nuclei possess charge. The projectile and target experience a mutual repulsion described by the Coulomb potential energy, V :

$$V = \frac{Z_p Z_t e^2}{4\pi\epsilon_0 r}.\tag{5.12}$$

Classically, the projectile will approach the target until the point at which the Coulomb potential energy equals the initial kinetic energy, E , of the projectile. This distance of closest approach, R_C , must be no more than the nuclear radius of the target nuclei or the reaction is classically forbidden [48].

$$\begin{aligned}E &= V \\ &= \frac{Z_p Z_t e^2}{4\pi\epsilon_0 R_C}\end{aligned}$$

$$R_C = \frac{Z_p Z_t e^2}{4\pi\epsilon_0 E} \quad (5.13)$$

\equiv Coulomb radius.

The resulting Coulomb barrier has a thickness of $R_C - r_n$. [See Figure 5.1.]

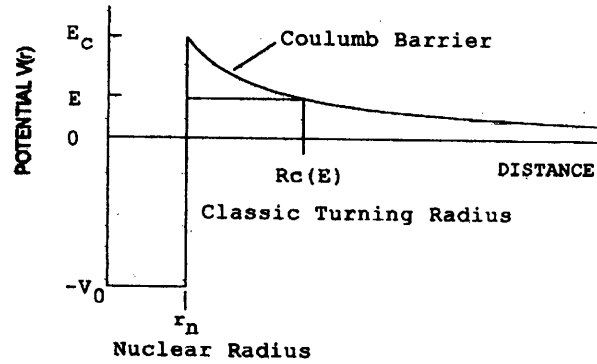


FIG. 5.1. Coulomb barrier

In quantum mechanics, the square of the wavefunction of a particle, $|\Psi(r)|^2$, is a measure of the probability of finding the particle between positions r and $r + dr$. The value of $|\Psi(r)|^2$ at the nuclear radius, r_n , is non-zero and finite. Quantum mechanics permits that which classical mechanics forbids - barrier penetration [37].

The square of the transmission coefficient, $|T|^2$ is the probability of penetrating the barrier. For a square well, this probability is given by

$$P = |T|^2 = \frac{16k^2\kappa^2 \exp(-4\kappa L)}{|(\kappa - ik)^2 - (\kappa + ik)^2 \exp(-4\kappa L)|^2} \quad (5.14)$$

where

$$\begin{aligned} k &= \sqrt{2mE}/\hbar, \\ \kappa &= \sqrt{2m(V-E)}/\hbar, \text{ and} \\ L &\equiv \text{half width of barrier.} \end{aligned}$$

An arbitrarily shaped barrier (such as the Coulomb barrier) can be represented by a series of thin square barriers of width $\Delta x_i = 2L$. For thin barriers, $\exp(-4\kappa L) \rightarrow 1$ in the denominator of equation 5.14. The probability for penetrating any single thin barrier is then

$$P_i \approx \exp(-2\kappa\Delta x_i). \quad (5.15)$$

Each thin barrier penetration probability exists independently of the others. Ignoring multiple reflections at barrier surfaces, the probability for complete barrier penetration is given by the product

$$P = \prod_i P_i \exp(-2\kappa\Delta x_i) = \exp\left(-2 \sum_i \kappa\Delta x_i\right).$$

In the limit of infinitely thin barriers ($\Delta x_i \rightarrow 0$), the summation becomes an integral.

$$P = \exp\left(-2 \int_{R_C}^{r_n} dx \sqrt{2m(V-E)}/\hbar\right). \quad (5.16)$$

The Coulomb potential energy at any distance from the nucleus can be expressed in terms of the initial kinetic energy, the Coulomb radius, and the distance from the

nucleus. Recall that $V(R_C) = E$. Then

$$\begin{aligned}
 V(r) &= \frac{Z_p Z_t e^2}{4\pi\epsilon_0 r} \\
 &= \left(\frac{Z_p Z_t e^2}{4\pi\epsilon_0 R_C} \right) \left(\frac{R_C}{r} \right) \\
 &= V(R_C) \left(\frac{R_C}{r} \right) \\
 &= E \left(\frac{R_C}{r} \right);
 \end{aligned}$$

therefore,

$$P \approx \exp \left[\left(-\frac{2}{\hbar} \right) \sqrt{2mE} \int_{r_n}^{R_C} dr \sqrt{\frac{R_C}{r} - 1} \right]. \quad (5.17)$$

If $R_C \gg r_n$, that is if $V \gg E$, then

$$\begin{aligned}
 P &\approx \exp \left[\sqrt{\frac{Z_p Z_t e^2 m r_n}{4\pi\epsilon_0}} - \left(\frac{4\pi}{\hbar} \right) \left(\frac{Z_p Z_t e^2}{4\pi\epsilon_0} \right) \sqrt{\frac{m}{E}} \right] \\
 &= \exp \left[\sqrt{\frac{Z_p Z_t e^2 m r_n}{4\pi\epsilon_0}} \right] \exp \left[-4.980 Z_p Z_t \sqrt{\frac{m}{E}} \right] \\
 &= A \exp \left[-\sqrt{\frac{E_G}{E}} \right]
 \end{aligned} \quad (5.18)$$

where the exponential is known as the Gamow factor and E_G is the Gamow energy expressed in keV [49]. The cross section has been shown to depend on the deBroglie wavelength and on the Gamow energy for energies less than the Coulomb potential of the reactants. The nuclei consist of nucleons that interact via the nuclear force [48]. In the cross section, the astrophysical S-factor, $S(E)$, contains all of the nuclear effects and absorbs all of the constants of proportionality. The energy dependent

cross section is thus given by [37]:

$$\sigma(E) = \frac{S(E) \exp\left[-\sqrt{\frac{E_G}{E}}\right]}{E}. \quad (5.19)$$

Although the cross section strongly depends on the energy, the S-factor is a slowly varying function of energy.

5.3 Effective energy and relative cross sections

In thick targets, reactions occur at energies ranging from the incident projectile energy, E_0 , to the incident energy minus the target thickness in energy units, $E_0 - \Delta$. The effective energy is defined as the single energy, \bar{E} , for which the thin target cross section would be equal to the measured thick-target cross section [37]. The value of the effective energy is determined from the thick target yield equation [equation 5.7]. The yield due to all the reactions that occur at energies less than the effective energy must equal the yield due to all the reactions at energies greater than the effective energy:

$$\int_{E_0 - \Delta}^{\bar{E}_{CM}} dE \frac{\sigma(E)}{\varepsilon(E)} = \int_{\bar{E}_{CM}}^{E_0} dE \frac{\sigma(E)}{\varepsilon(E)} = \frac{1}{2} \int_{E_0 - \Delta}^{E_0} dE \frac{\sigma(E)}{\varepsilon(E)}. \quad (5.20)$$

The pressed powder and foil targets stopped all projectiles; therefore, the target thicknesses in energy units equaled or exceeded the incident projectile energies, $E_0 \geq \Delta$. Recalling equation 5.19 for the cross section, assuming a constant S-factor, and simplifying gives

$$\int_0^{E_0} dE \frac{\exp[-31.29 Z_p Z_t \sqrt{\mu/E}]}{E \varepsilon(E)} = 2 \int_0^{\bar{E}_{CM}} dE \frac{\exp[-31.29 Z_p Z_t \sqrt{\mu/E}]}{E \varepsilon(E)} \quad (5.21)$$

Equation 5.21 was evaluated for each reaction-energy pair and the results are sum-

Table 5.1. Energy relations for the deuteron-induced proton transfer reactions

Target	$E_{d,lab}$ (keV)	E_{CM} (keV)	\bar{E}_{CM} (keV)	$\bar{E}_{d,lab}$ (keV)
^2H	60	30	24	48
	105	52.5	40.2	80.4
^6Li	140	105	94.3	126
^7Li	70.0	54.4	50.0	64.4
	120	93.2	83.5	108
	145	113	100	129
^9Be	145	119	109	133
^{10}B	145	121	111	133
^{11}B	145	123	112	133

marized in Table 5.1.

The true accumulated charge may differ from the measured accumulated charge. The deuterons have enough energy that they free electrons from the surface of the solid targets. The freed electrons produce an increase in the measured charge over the true charge. The difference introduces uncertainty in the measured yield per incident deuteron. That uncertainty can be removed by measuring the yield of the (d,n) reaction relative to a (d, charged particle) yield from the SSB detector fixed at 90° . Recall that for a thin target, the yield per incident particle can be expressed as $\Delta Y = \sigma n \Delta x$. [Refer to equation 5.1.] As previously defined, the effective energy for a thick target corresponds to the single energy for a thin target that produces the same measured cross section. Recall that the yield, Y , is the measured counts, N , of a reaction product divided by the number of projectiles, n_d , and by the detector efficiency, η . Substituting N , n_d , and η into equation 5.1, relabelling the target number

density n as n_t , and rearranging gives

$$N = \sigma n_d n_t \eta \Delta x. \quad (5.22)$$

Consider two reactions with the same projectiles and which have measured product counts of N_n and N_p respectively. The target densities are $n_{t,n}$ and $n_{t,p}$ respectively. Differences in detector sizes and placements may result in different solid angles - Ω_n and Ω_p for the measurements. Application of equation 5.22 to and inclusion of solid angles for both reactions gives the ratio of the measured counts for the two reactions:

$$\frac{N_n}{N_p} = \frac{\sigma_n n_d n_{t,n} \Delta x \eta_n \Omega_n}{\sigma_p n_d n_{t,p} \Delta x \eta_p \Omega_p}. \quad (5.23)$$

Solving for the unknown cross section, σ_n in terms of the known cross section, σ_p , gives

$$\sigma_n = \sigma_p \frac{N_n n_{t,p} \eta_p \Omega_p}{N_p n_{t,n} \eta_n \Omega_n}. \quad (5.24)$$

The target densities are equal when the entrance channels to the two reactions are identical. For this condition, equation 5.24 simplifies to

$$\sigma_n = \sigma_p \frac{N_n \eta_p \Omega_p}{N_p \eta_n \Omega_n}. \quad (5.25)$$

As shown in equations 5.24 and 5.25, the charge dependence [expressed as the projectile density, n_d] has been eliminated. This method of relative cross section requires prior knowledge of the absolute cross section of one of the reactions to determine the absolute cross sections of the second reaction. The absolute cross sections for deuteron-induced charged-particle-as-product reactions have been determined by the Colorado School of Mines nuclear group [7, 20] and others [26, 9]. The charged

particle cross section results were applied to the relative cross sections in this thesis to determine the absolute cross sections for the deuteron-induced proton transfer reactions.

Chapter 6

THE REACTIONS

6.1 Validation of the Kent State University Neutron Detection Efficiency Code with the known reaction ${}^2\text{H}(\text{d},\text{n}){}^3\text{He}$

Deuterium and tritium are supposed to power fusion reactors. Consequently, the ${}^2\text{H}(\text{d},\text{n}){}^3\text{He}$ has been thoroughly investigated [26, 27]. This reaction was used to validate the application of the relative cross section method to determine absolute cross section for the deuteron-induced proton transfer reactions and the accuracy of the Kent State University Neutron Detection Efficiency code. The relative angular distributions at 60 keV and 105 keV deuteron bombarding energies were measured. [These corresponded to effective center-of-momentum energies of 24 keV and 40 keV, respectively.] Deuterons from the accelerator collided with an aluminum block placed in the target chamber of the accelerator. The charge dependence of the Coulomb barrier suppressed the reactions of the deuterons with the aluminum. The non-reacted deuterons accumulated in the aluminum. Those accumulating deuterons formed the target for the ${}^2\text{H} + \text{d}$ reactions. The silicon surface barrier [SSB] detector fixed at 90° monitored the production of charged particles. The SSB was 100% efficient.

The BC-501A neutron detector was not 100% efficient. The Kent State University Neutron Detector Efficiency computer code produced tables of integral efficiencies for the operating conditions of the detector. Those integral efficiencies represented the percent of neutrons incident on the BC-501A detector that were detected when the counts were summed from the maximum energy channel associated with the incident

neutron energy down to the chosen low-end channel.

The true neutron counts were extracted from the raw neutron spectra in three steps. First, neutrons from reactions other than ${}^2\text{H}(\text{d},\text{n}){}^3\text{He}$ were subtracted from the raw spectrum. The number of neutrons to be subtracted from each channel was determined by extending a curve fit into the region of channels of interest. The curve fit went from some higher channel to one channel above the channel of maximum energy of the reaction. The best curve for the set of reactions was determined by minimizing the χ^2 of the curve fit equation. The remaining neutrons were taken to be the neutrons from the ${}^2\text{H}(\text{d},\text{n}){}^3\text{He}$ reaction. Although neutrons from the reaction chain ${}^2\text{H}(\text{d},\text{p}){}^3\text{H} \rightarrow {}^3\text{H}(\text{d},\text{n}){}^4\text{He}$ from the build-up of tritium was an initial concern, the total background was determined to be negligible compared to the counts in the ${}^2\text{H}(\text{d},\text{n}){}^3\text{He}$ reactions and so was ignored. Figure 6.1 demonstrates the low background in a typical neutron spectrum for the ${}^2\text{H}(\text{d},\text{n}){}^3\text{He}$ reaction.

Next, the counts in the neutron spectrum from the maximum reaction channel to each lower channel were summed. These sums at each channel were divided by the corresponding integral efficiencies for each channel as determined by the Kent State code. Ideally, the number resulting from the preceding steps would be the same for every channel and equal the total neutron counts that entered the detector. In reality, variations in that number occurred from channel to channel as shown in Figure 6.2.

The third step quantified those variations. The total neutron counts from a representative sample of channels were averaged. That average was taken to be the true neutron counts, N_n/η_n , for a neutron detector of unit efficiency, $\eta_n = 1$. The variance of the true neutron counts was defined as the average of the differences between the true neutron counts and the extrema of the sampled channels. This variance was used in the propagation of errors through quadrature.

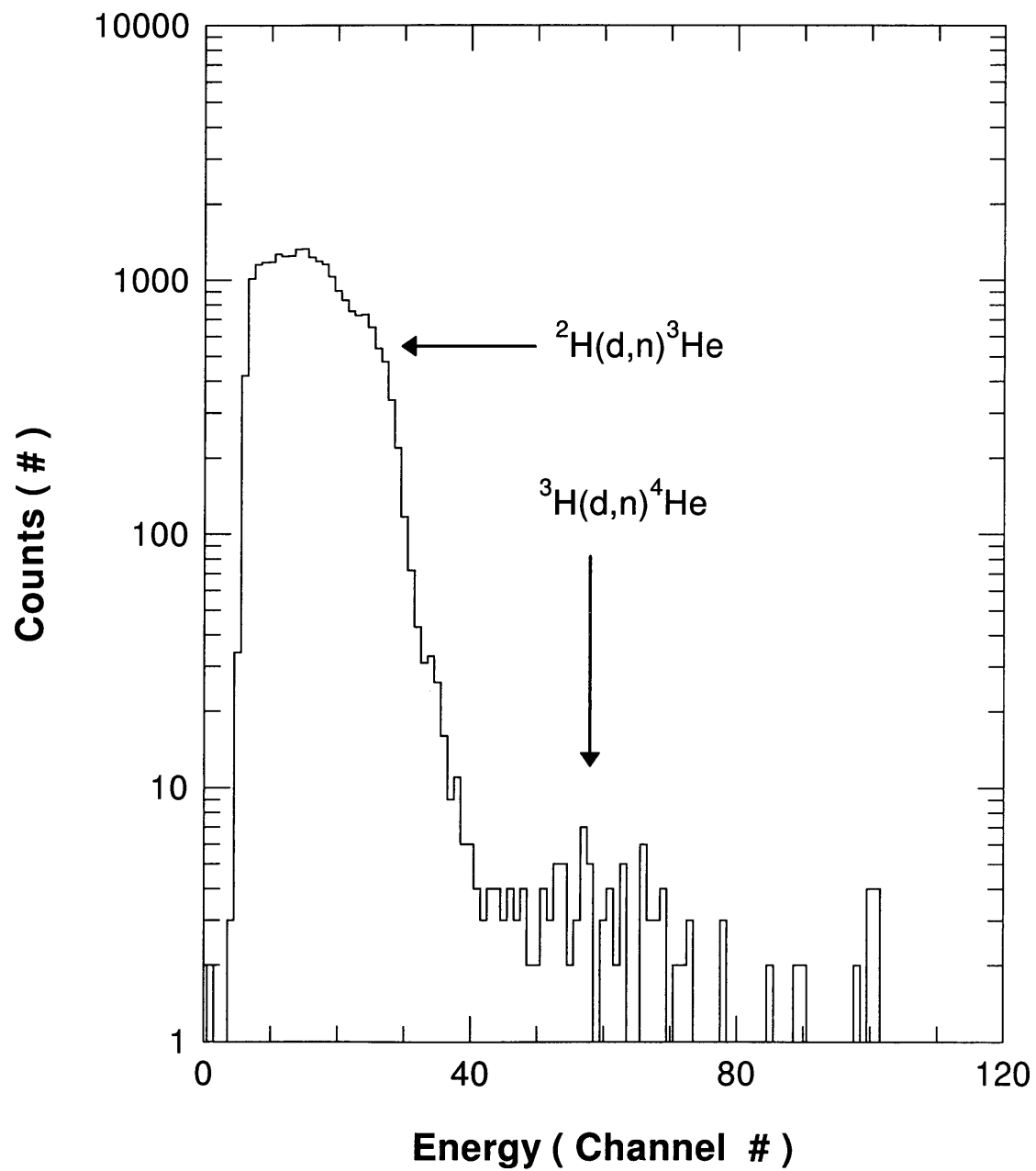


FIG. 6.1. Typical neutron spectrum for the ${}^2\text{H}(d,n){}^3\text{He}$ reaction.

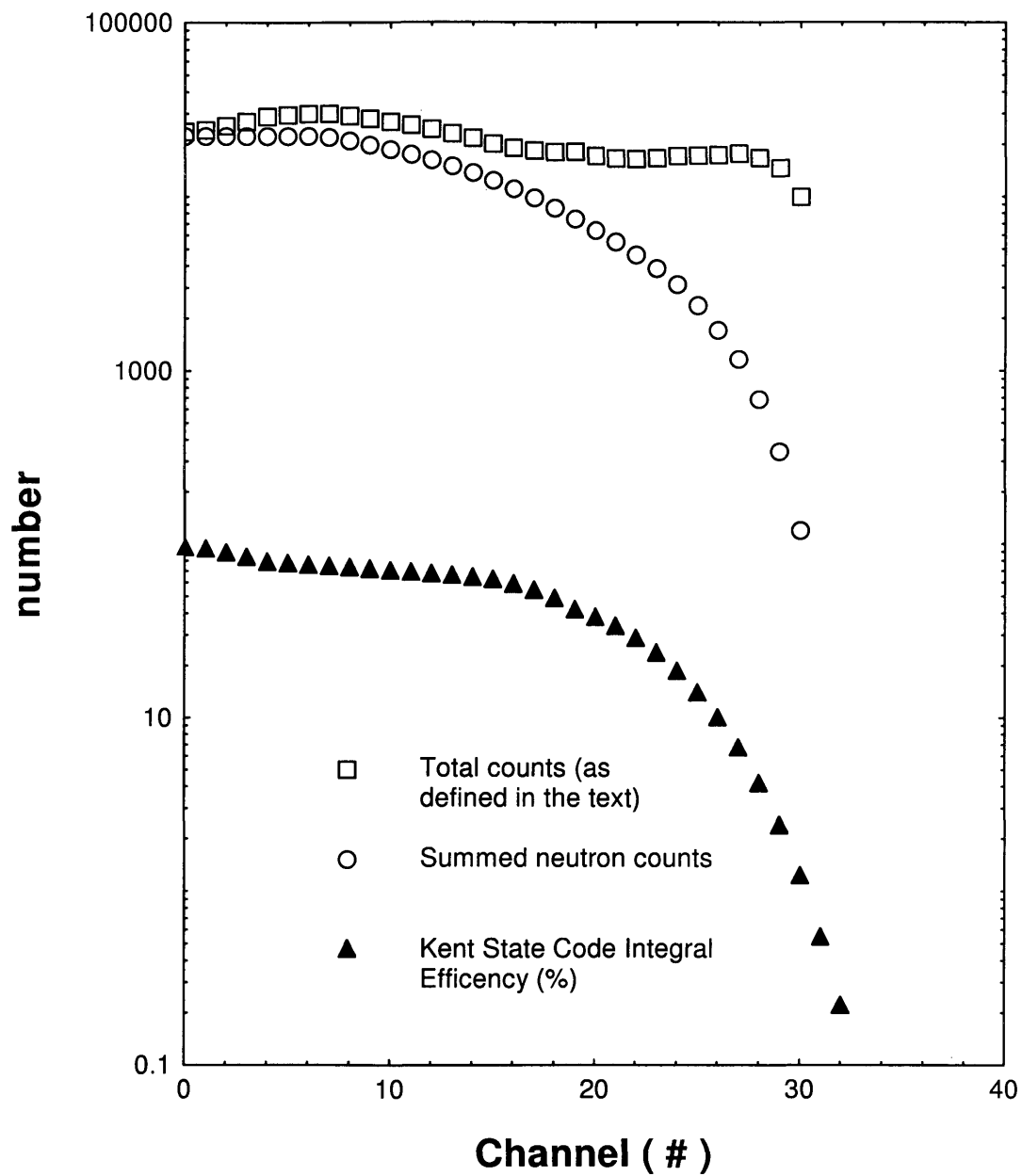


FIG. 6.2. Graphical representation of the method for determining the true neutron counts for the ${}^2\text{H}(d,n){}^3\text{He}$ reaction.

Due to different physical detector sizes and placements, different solid angles were subtended by the SSB and neutron detectors as seen from the target. To compare the relative yields, the counts from each detector were normalized by those solid angles.

Consider the ${}^2\text{H}(\text{d},\text{n}){}^3\text{He}$ reaction at the laboratory energy of 105 keV and at one angle, say 0° . The counts were summed for channels 15 to 30, channels 20 to 30, and channels 25 to 30. Consider the channels 15 to 30. The sum over these channels equaled 12295 counts. The efficiency determined by the Kent State code equaled 61.35%. The solid angle subtended by the neutron detector was 95.5 msr. The total neutron counts per steradian was determined to be

$$\begin{aligned}\frac{N_n}{\Omega_n \eta_n} &= \frac{12295 \text{ counts} * 100 \%}{95.5 \text{ msr} * 61.35 \%} \\ &= 209.9 \text{ counts/msr} \\ &\approx 210 \text{ counts/msr}\end{aligned}$$

The results for the total neutron counts for channels 20 to 30 and for channels 25 to 30 were 178 counts/msr and 182 counts/msr, respectively. The true value and variance were (190 ± 20) counts/msr.

Figure 6.3 shows the particle spectrum collected by the SSB detector. The ${}^2\text{H}(\text{d},\text{p}){}^3\text{H}$ peak is clearly visible over channels 101 to 120. Negligible background counts appeared in the these channels. The total counts in the ${}^2\text{H}(\text{d},\text{p}){}^3\text{H}$ peak equaled 5958. The angle subtended by the SSB detector as seen from the target equaled 51.6 msr. The counts per steradian for the ${}^2\text{H}(\text{d},\text{p}){}^3\text{H}$ reaction was determined to be 116 counts / msr.

$$\begin{aligned}\frac{N_p}{\Omega_p \eta_p} &= \frac{5958 \text{ counts} * 100 \%}{51.6 \text{ msr} * 100 \%} \\ &= 116.07 \text{ counts/msr} \approx 116 \text{ counts/msr}\end{aligned}$$

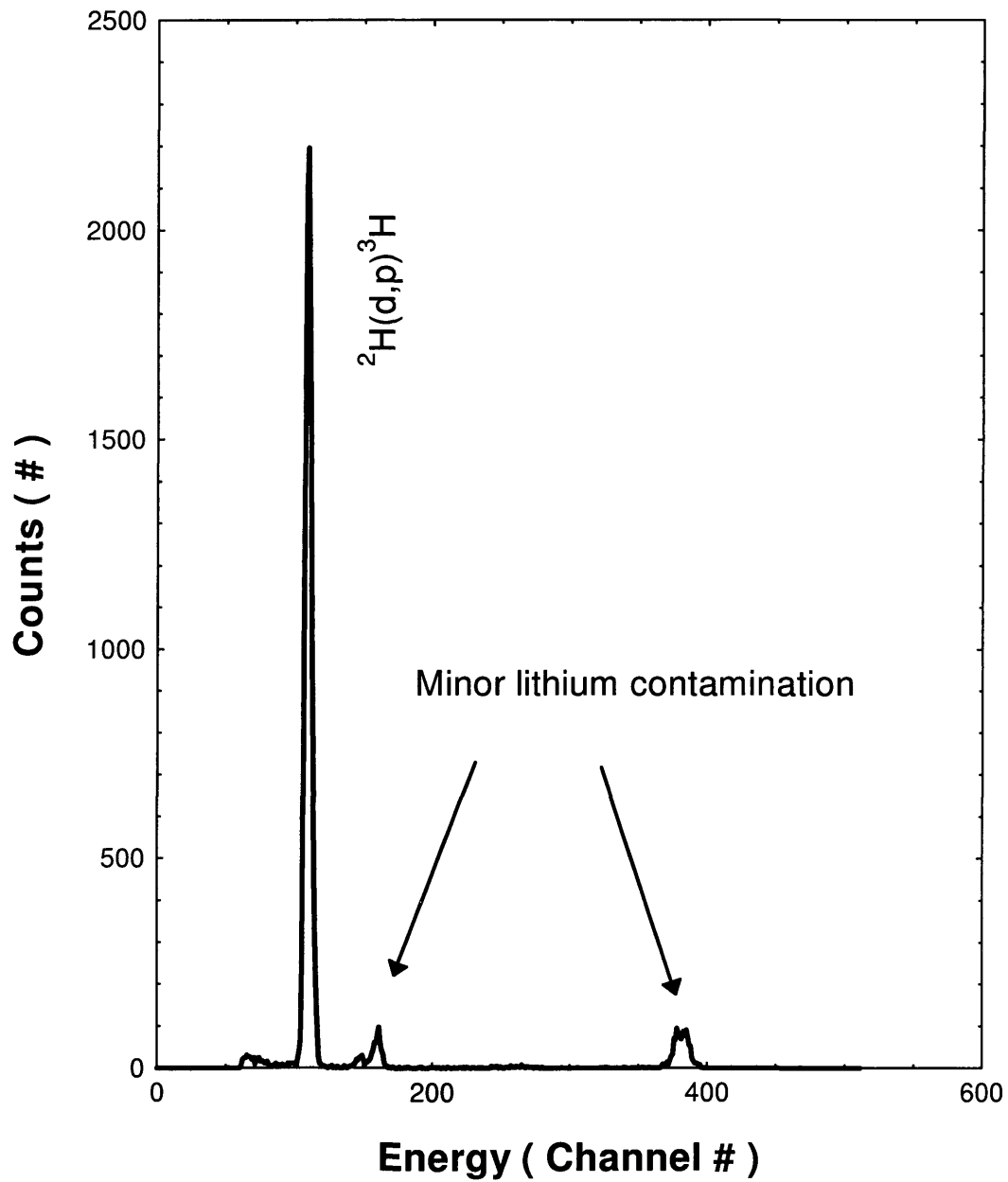


FIG. 6.3. Typical charged particle spectrum for the deuteron-induced reaction on deuterium.

Table I in the paper by Brown and Jarmie [27] gives the differential cross section for the ${}^2\text{H}(d,n){}^2\text{H}$ reaction at a laboratory deuteron energy of 80 keV and a detector angle of 90° as $\sigma(E_d = 80\text{keV}, \theta_{CM} = 90^\circ) = 0.753 \text{ mb/sr}$. Relative errors of $< 2\%$ are quoted. Application of equation 5.25 to the current example gives an absolute differential cross section of $(1.23 \pm 0.17) \text{ mb/sr}$ as shown in the following calculation.

$$\begin{aligned} \sigma(\bar{E}_d = 80 \text{ keV}, \theta_{n,CM} = 0^\circ) &= \left[\frac{(190 \pm 20) \text{ counts/msr}}{116 \text{ counts/msr}} \right] (0.753 \text{ mb/sr}) \\ &= (1.233 \pm .130) \text{ mb/sr} \\ &\approx (1.23 \pm 0.13) \text{ mb/sr}. \end{aligned}$$

The absolute differential cross sections for all angles at both energies are given in Table 6.1.

Table 6.1. Experimental differential cross sections for the reaction ${}^2\text{H}(d,n){}^3\text{He}$

Center-of-Momentum Effective Energy (keV)	Center-of-Momentum Angle (degrees)	Differential Cross Section (mb / sr)
24	0	0.770 ± 0.047
	31.4	0.697 ± 0.026
	62.5	0.505 ± 0.023
	92.4	0.460 ± 0.022
40	0	1.23 ± 0.13
	31.8	1.02 ± 0.13
	63.2	0.833 ± 0.064
	93.6	0.683 ± 0.085

The integrated absolute cross sections were determined by integrating the curve fits to the differential absolute cross sections. A differential cross section is modeled as the square of the sum of a series of Legendre polynomials. [This technique is known as the method of partial waves.] Following spectroscopic notation, the first

three Legendre polynomial contributions are known as s-wave, p-wave, and d-wave. Legendre polynomials consist of powers of cosines; therefore, the differential data were fit with curves that had powers of cosine for terms. The target and the projectile are identical particles for the deuteron on deuterium reactions. The angular distribution of the cross section for identical particle reactions is symmetric about 90° in the center-of-momentum frame. Only even powers of cosine match this symmetry criterion; therefore, the angular distribution of the ${}^2\text{H}(\text{d,p}){}^3\text{H}$ reaction was fit to a curve of the form $\sigma(E, \theta_{CM}) = a + c \cos^2(\theta_{CM})$. Table 6.7 contains the curve fit coefficients for the ${}^2\text{H}(\text{d,p}){}^3\text{H}$ reaction and all other reactions contained in this thesis. Figure 6.4 shows the data set and curve fits to the current work and Figure 6.5 shows the excellent agreement of this data set with that of Brown and Jarmie [27]. The horizontal bars in Figure 6.4 and all subsequent figures of differential cross sections represent the angles subtended by the detector as viewed from the target. These finite angles affect the measured number of counts. The effect depends on the trend of the data for angles around the central angle of the detector measured with respect to the incoming ion beam. For example, in Figure 6.4, the effect about the central angle of 0° is to lower the measured counts below the true value. The absolute integrated cross sections for this reaction and all other reactions in this thesis are listed in Table 6.8 along with the associated statistical and systematic errors.

Error was propagated through the curve fits by varying the values of the differential cross section data points through their errors and then fitting curves to those variations. The curves generated by this method were then integrated to obtain the variations in the integrated cross sections. The minimum and maximum values obtained with this method overestimated the effects of individual errors on the differential coefficients and on the integrated cross sections. Taking an average

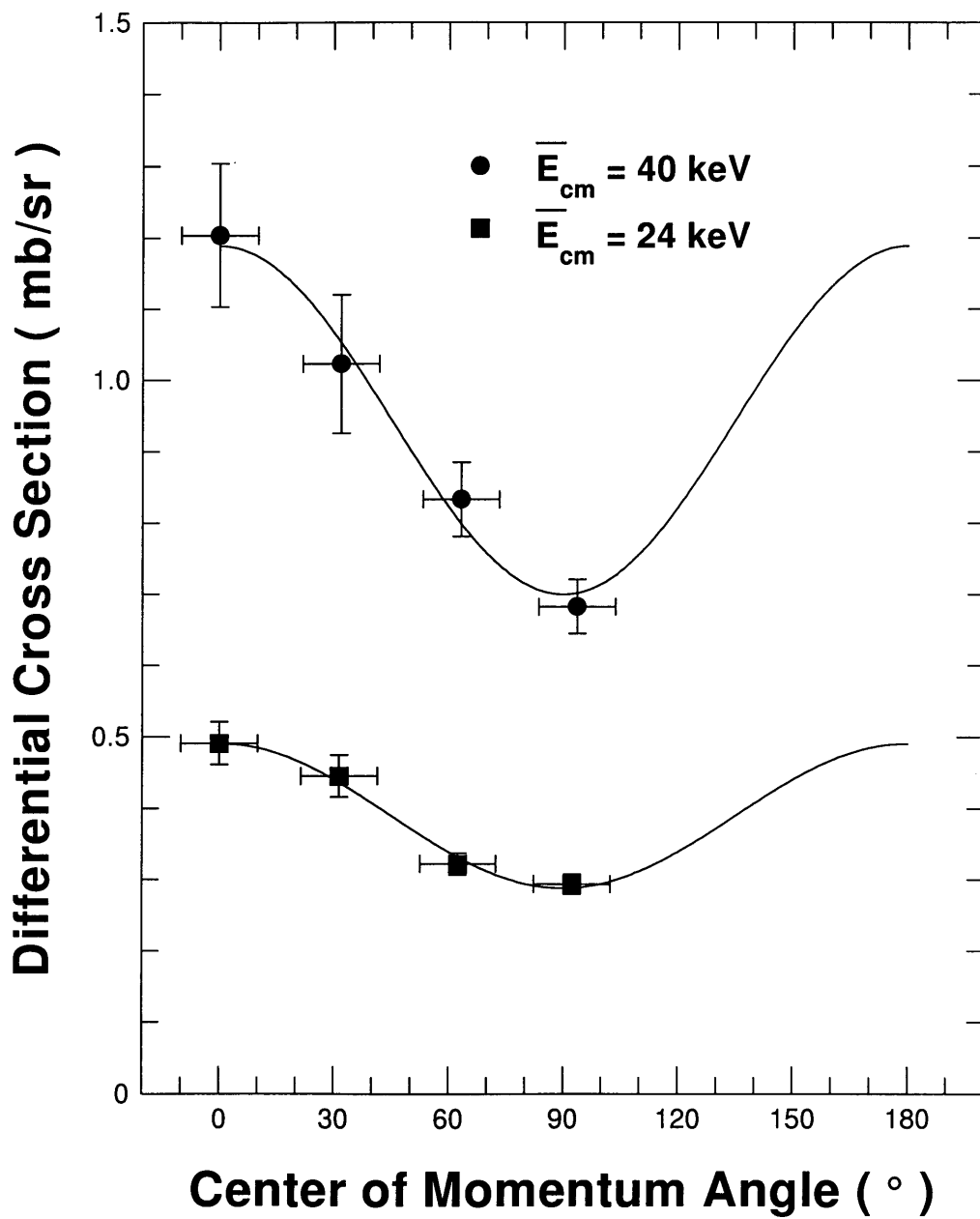


FIG. 6.4. Differential absolute cross sections for the ${}^2\text{H}(d,n){}^3\text{He}$ reaction in the center-of-momentum reference frame.

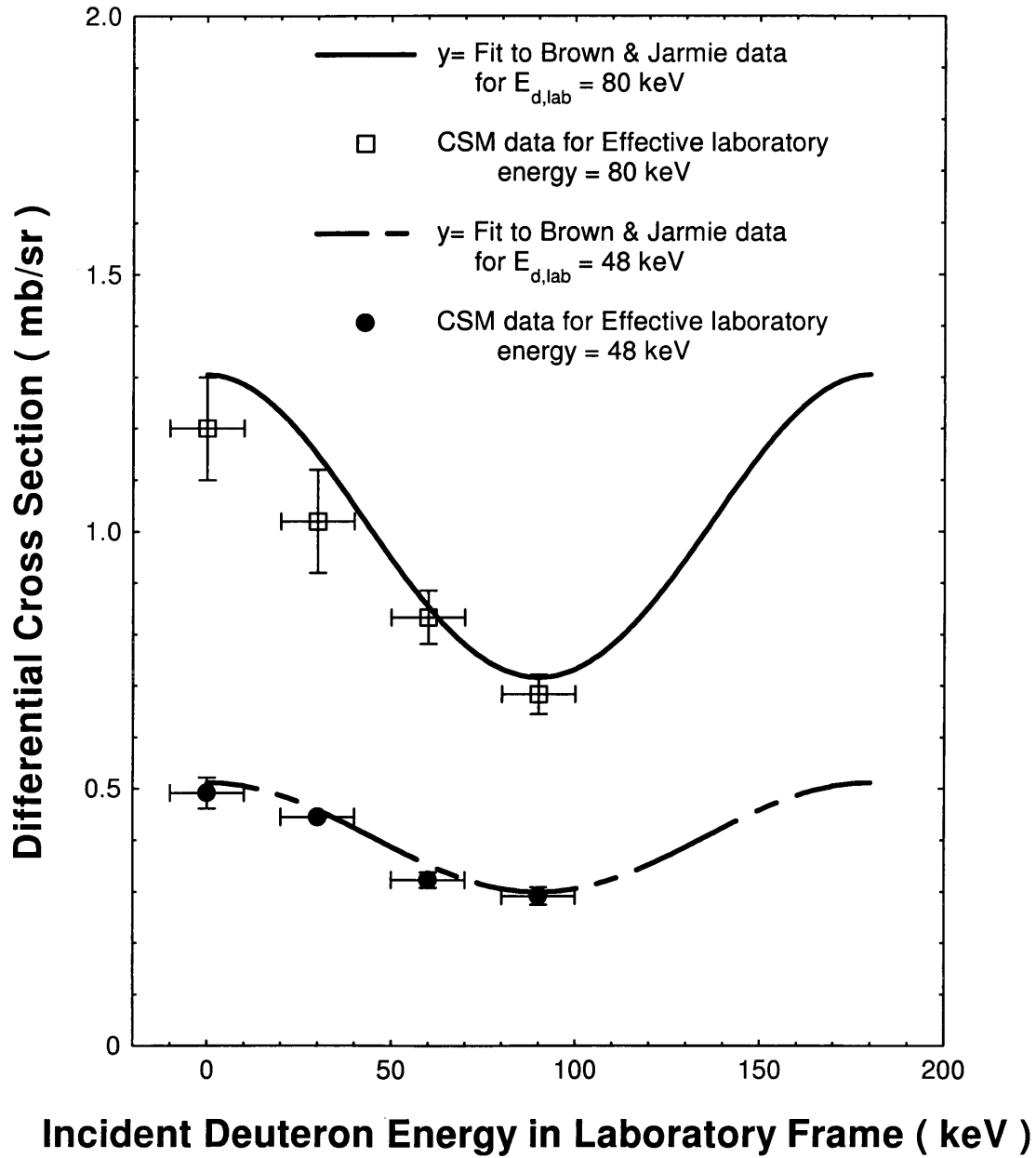


FIG. 6.5. Comparison of measurements of the differential cross sections for the ${}^2\text{H}(d,n){}^3\text{He}$ reaction at an effective center-of-momentum energy = 40 keV.

of the variations in the curve fit coefficients over many combinations of the errors in the data reduced the overestimate in the errors. As expected, the cross section varies greatly with energy. [See Figure 6.6] The astrophysical S-factor factors out the energy dependences of the Coulomb barrier and of the deBroglie wavelength. The remaining nuclear effects vary slowly with energy. Solving the thin target cross section equation [equation 5.19] for the S-factor gives

$$S(E) = \sigma(E) E \exp\left(\sqrt{E_G/E}\right). \quad (6.1)$$

Application of equation 6.1 to the absolute integrated cross section produced the S-factor, as shown in the following calculation for an effective center-of-momentum energy = 40 keV:

$$\begin{aligned} S(40 \text{ keV}) &= (10.8 \pm 0.50) \text{ mb} * 40 \text{ keV} * \exp\left[-31.29 * 1 * 1 * \sqrt{1.007051/40}\right] \\ &= 61887 \pm 2865 \text{ keV} - \text{mb} \\ &\approx 61.9 \pm 2.9 \text{ keV} - \text{b}. \end{aligned}$$

S-factor values calculated from the cross sections of this research and from published cross sections are shown in Figure 6.7 for the ${}^2\text{H}(\text{d},\text{n}){}^3\text{He}$ reaction.

The agreement of this research with the published data of Brown and Jarmie validated the use of the Kent State Neutron Detection Efficiency code with the method of relative cross sections. The method was applied to the remaining reactions in the current research.

INTEGRATED CROSS SECTION vs ENERGY for ${}^2\text{H}(d,n){}^3\text{He}$

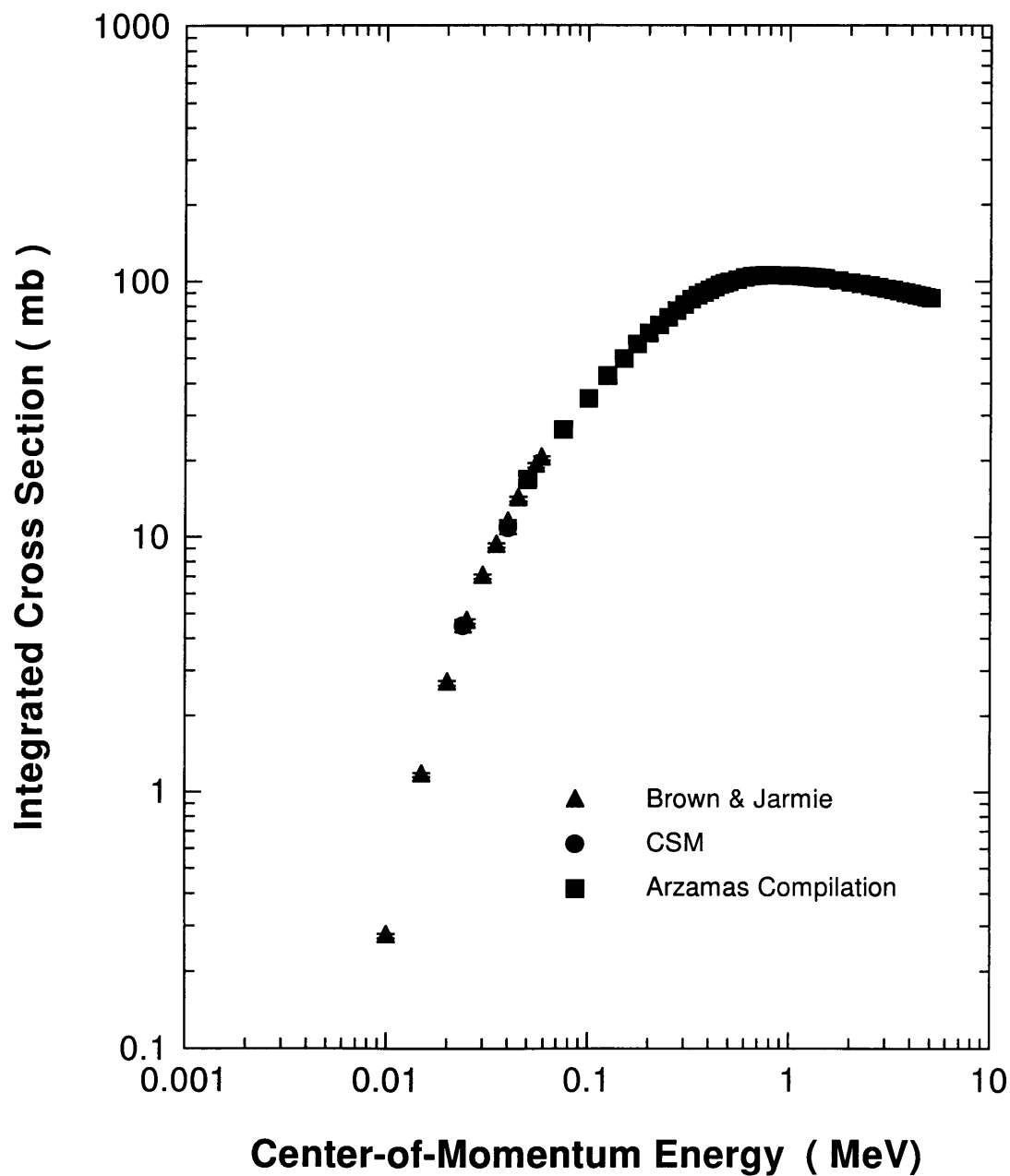


FIG. 6.6. Variation of the integrated cross section with energy for the ${}^2\text{H}(d,n){}^3\text{He}$ reaction in the center-of-momentum reference frame. Information regarding the cross section compilation by Arzamas can be found in reference [8].

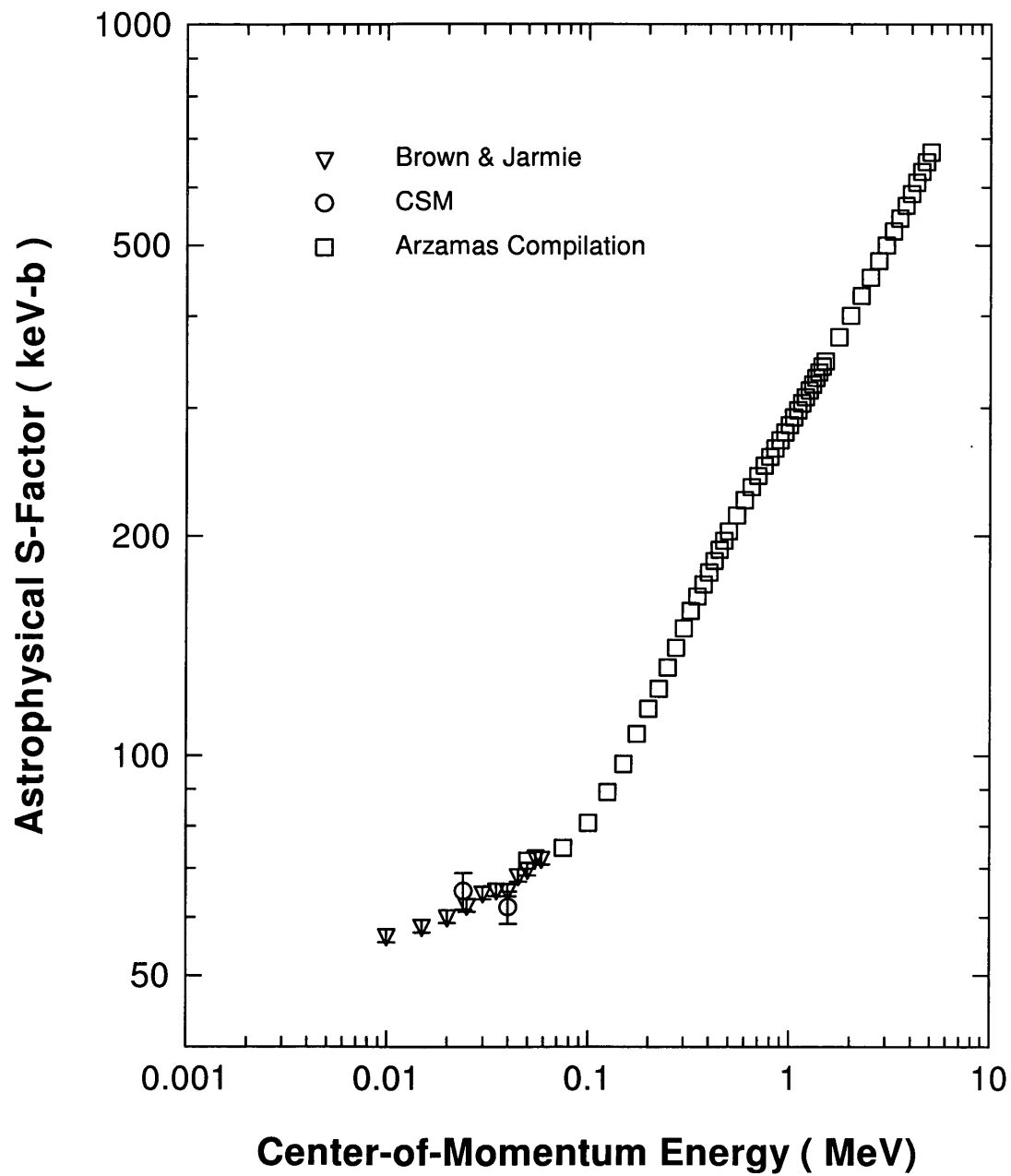


FIG. 6.7. Variation of the astrophysical S-factor with energy for the ${}^2\text{H}(d,n){}^3\text{He}$ reaction in the center-of-momentum reference frame.

6.2 ${}^6\text{Li}(d,n){}^7\text{Be}$ - an improved measurement at low energy

Elwyn, et al. [9] completed a very thorough examination of the (d,n) and (d,p) reactions on ${}^6\text{Li}$. The (d,n) reactions were performed at laboratory effective energies as low as 204 keV. The (d,p) reactions were performed at effective laboratory energies as low as 118 keV. In the current research, the laboratory effective energy was extended to 126 keV for the (d,n) reaction. (This corresponds to a center of momentum effective energy of 94.4 keV.) Hirst, et al. [28] measured the total cross section down to an effective laboratory energy of 115 keV. The error quoted in the report was $\pm 15\%$. The objective in performing this reaction was to confirm the work of Hirst, et al. and improve on the reported error. The absolute differential and integrated cross sections were determined with the method of relative cross sections as had been done for the ${}^2\text{H}(d,n){}^3\text{He}$ reaction.

The neutron spectra was more complicated than the spectrum for the ${}^2\text{H}(d,n){}^3\text{He}$ reactions. Deuterium built up in the lithium foil just as it had in the aluminum block. The close proximity of the energies of neutrons from the ${}^2\text{H}(d,n){}^3\text{He}$ reaction to those from the ${}^6\text{Li}(d,n){}^7\text{Be}$ reaction [~ 2.9 MeV vs ~ 3.3 MeV for a neutron detector angle of 0°] contributed to the total neutron counts at lower channel numbers. This effectively set lower limits on the channels for extraction of the true neutron counts from the ${}^6\text{Li}(d,n){}^7\text{Be}$ reaction. In addition, the lithium foil was not 100% ${}^6\text{Li}$. The ${}^7\text{Li}(d,n){}^8\text{Be}$ reaction contributed non-negligible background counts to the observed neutron counts. The best fit curves to the background, as determined by finding the minimum χ^2 , were three-parameter exponential curves:

$$y_{\text{bkg}} = a \exp(bx) + c. \quad (6.2)$$

These effects of the deuterium and of the ${}^7\text{Li}$ are noted in the sample spectrum of Figure 6.8. Consider the ${}^6\text{Li}(d,n){}^7\text{Be}$ reaction at the laboratory energy of 140 keV and at one angle, say 30° . The background curve was fit over channels 41 to 82. The fit parameters were $a = 326$ counts, $b = -0.0333$ (channels) $^{-1}$ and $c = -14.2$ counts. The background-subtracted counts were summed for channels 28 to 40, channels 30 to 40, and channels 33 to 40. Consider the channels 30 to 40. The sum over these channels equaled 4342 counts. The efficiency determined by the Kent State code equaled 39.019%. The solid angle subtended by the neutron detector was 95.5 msr. The true neutron counts per steradian was determined to be

$$\begin{aligned} \frac{N_n}{\Omega_n \eta_n} &= \frac{4342 \text{ counts} * 100 \%}{95.5 \text{ msr} * 39.019 \%} \\ &= 155.02 \text{ counts/msr} \\ &\approx 155 \text{ counts/msr.} \end{aligned}$$

The results for channels 28 to 40 and for channels 33 to 40 were 151 counts/msr and 147 counts/msr respectively. The true value and variance were (151 ± 4) counts/msr.

Figure 6.9 shows the particle spectrum collected by the SSB detector. The ${}^6\text{Li}(d,p_0+p_1){}^7\text{Be}$ double-peak spans channels 144 to 177. The entire double peak sits on top of an α -particle continuum from the ${}^7\text{Li} + d$, 3-body final state reactions. The contribution from that continuum to the total counts was negligible. The total counts in the ${}^6\text{Li}(d,p_0+p_1){}^7\text{Be}$ double-peak equaled 3216. The angle subtended by the SSB detector as seen from the target equaled 51.6 msr. The counts per steradian for the ${}^6\text{Li}(d,p_0+p_1){}^7\text{Be}$ reaction was determined to be 62.3 counts/msr.

$$\begin{aligned} \frac{N_p}{\Omega_p \eta_p} &= \frac{3216 \text{ counts} * 100 \%}{51.6 \text{ msr} * 100 \%} \\ &= 62.33 \text{ counts/msr} \approx 62.3 \text{ counts/msr} \end{aligned}$$

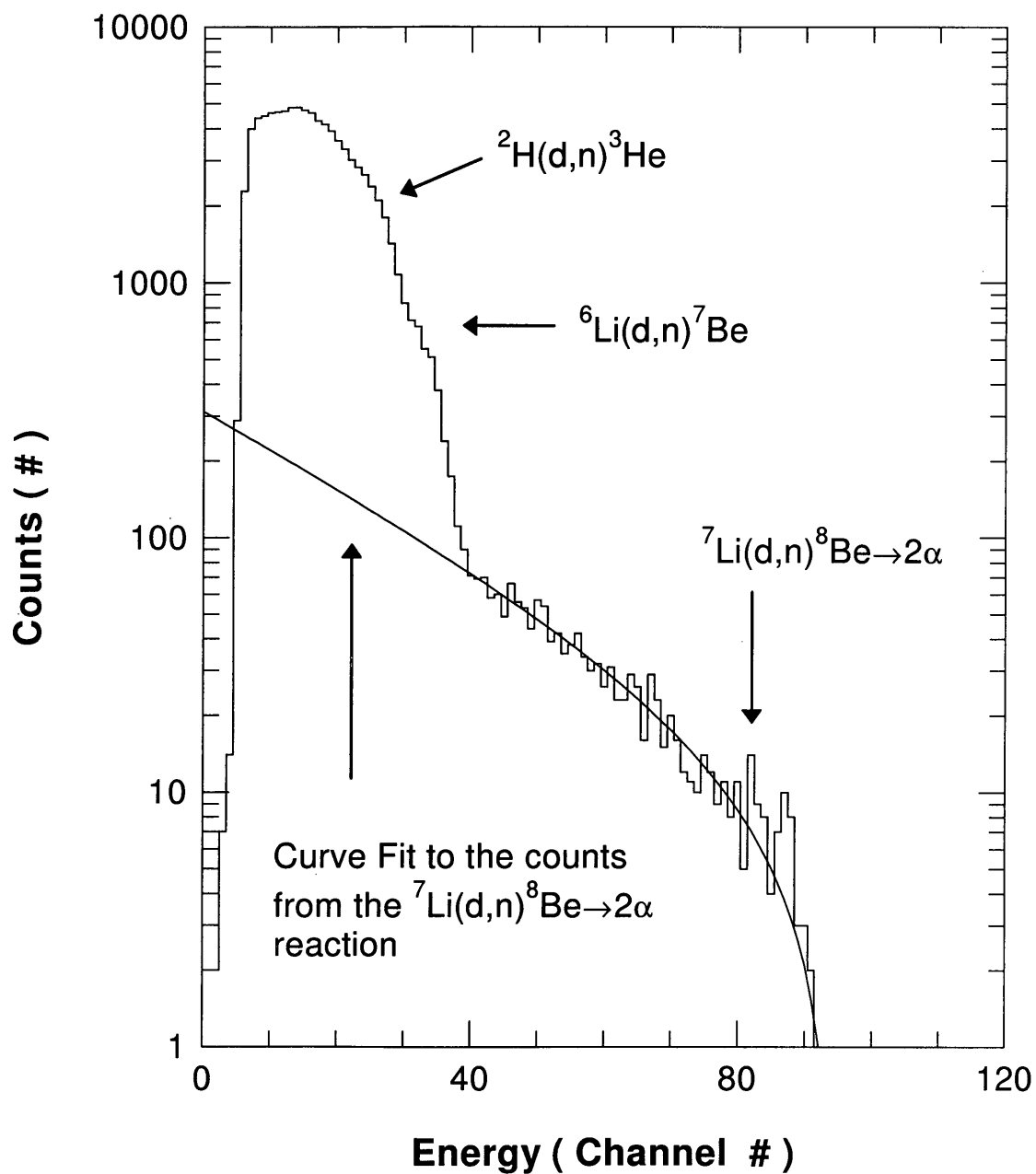


FIG. 6.8. Sample ${}^6\text{Li}(d,n){}^7\text{Be}$ neutron spectrum. Note the contribution (below channel 28) from the ${}^2\text{H}(d,n){}^3\text{He}$ reaction. The smooth curve is a best fit to the background neutrons from the ${}^7\text{Li}(d,n){}^8\text{Be}$ reactions.

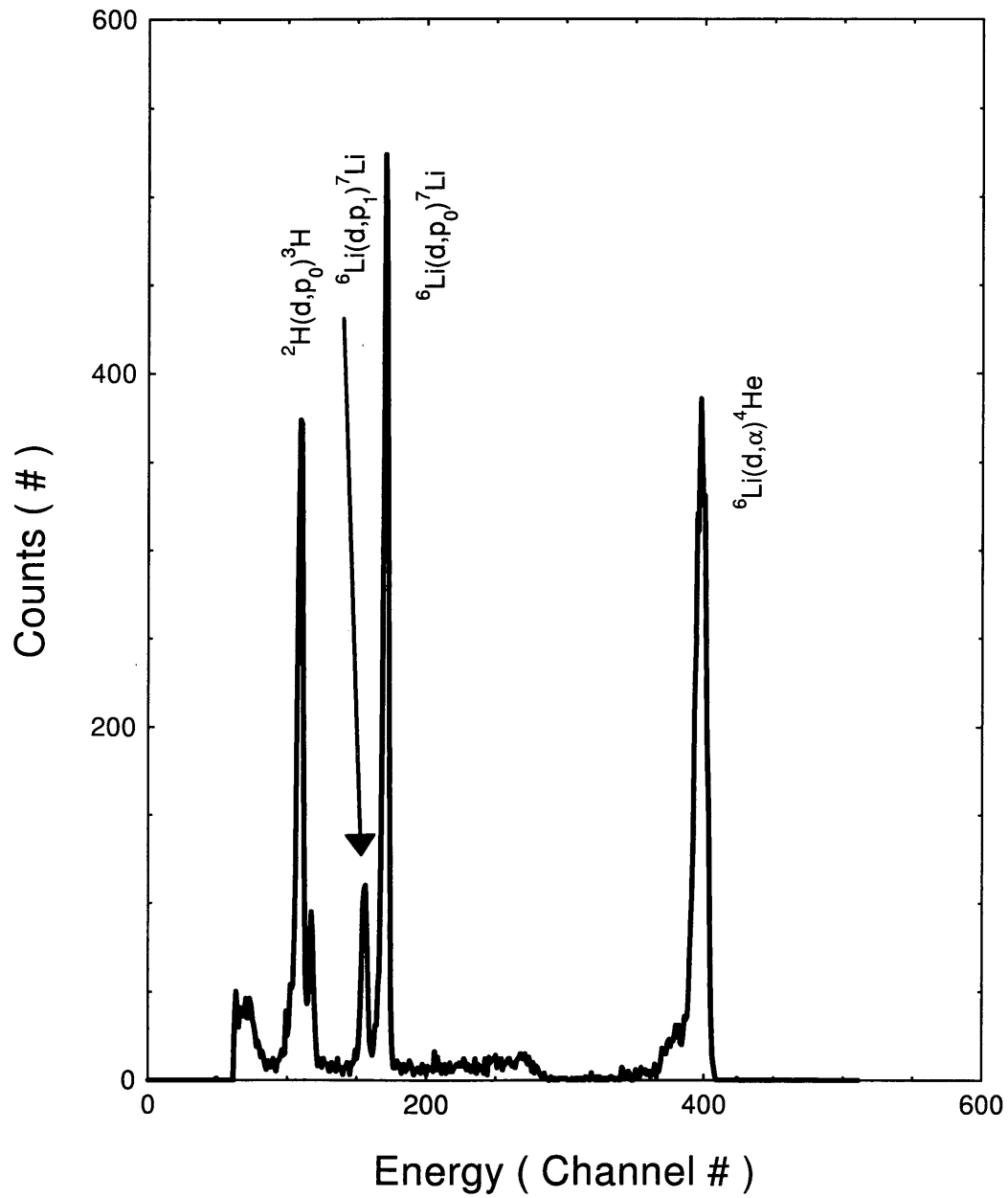


FIG. 6.9. Sample charged particle spectrum for deuterons on ${}^6\text{Li}$.

Table VI in the paper by Elwyn, et. al. [9] lists the absolute values for the differential cross sections. The listed effective energies in the laboratory frame bracket the 126 keV effective energy in the current research. The values of the cross sections for the ${}^6\text{Li}(d,p_0){}^7\text{Be}$ and ${}^6\text{Li}(d,p_1){}^7\text{Be}$ reactions at an effective energy of 126 keV was extracted from curve fits to the 90° data in that table. [See Figure 6.10.] The summed curve fit values for the differential cross sections at the detector angle of 90° was $\sigma(E_d = 126\text{keV}, \theta_{lab} = 90^\circ) = 0.108$ mb/sr. Relative errors in the angular distributions were not given for the data points. Coefficients for Legendre polynomial fits to the data were given in table IV [9] along with statistical-only errors. Those statistical errors were $\leq \pm 4\%$. The quoted error in the integrated cross sections varied between 13% and 16%. For the purposes of determining total error in the current data set, an error of $\pm 7.5\%$ in the extracted value of the differential cross section was assumed. [Note that the author believes this to be an overestimate of the actual error but favors too large rather than too small an error.] Application of equation 5.25 to the current example gives an absolute differential cross section of (0.262 ± 0.007) mb/sr as shown in the following calculation. The quoted error is purely statistical.

$$\begin{aligned} \sigma(\bar{E}_d = 126\text{keV}, \theta_{n,CM} = 93.6^\circ) &= \left[\frac{(151 \pm 4)\text{ counts/msr}}{62.3\text{ counts/msr}} \right] (0.108\text{ mb/sr}) \\ &= (0.2617 \pm 0.0069)\text{ mb/sr} \\ &\approx (0.262 \pm 0.007)\text{ mb/sr} \end{aligned}$$

The absolute differential cross sections for all angles is given in Table 6.2. The errors listed do not include the $\pm 7.5\%$ systematic error from the interpolation of the ${}^6\text{Li}(d,p_0){}^7\text{Li}$ plus ${}^6\text{Li}(d,p_1){}^7\text{Li}$ reactions. Since the experimental values for the differential cross sections overlap to within error, the differential cross section was fit to a constant of $\sigma(\bar{E}_{CM} = 94.3\text{keV}, \theta_{CM}) = 0.254 \pm 8$ mb/sr as shown in Figure 6.11.

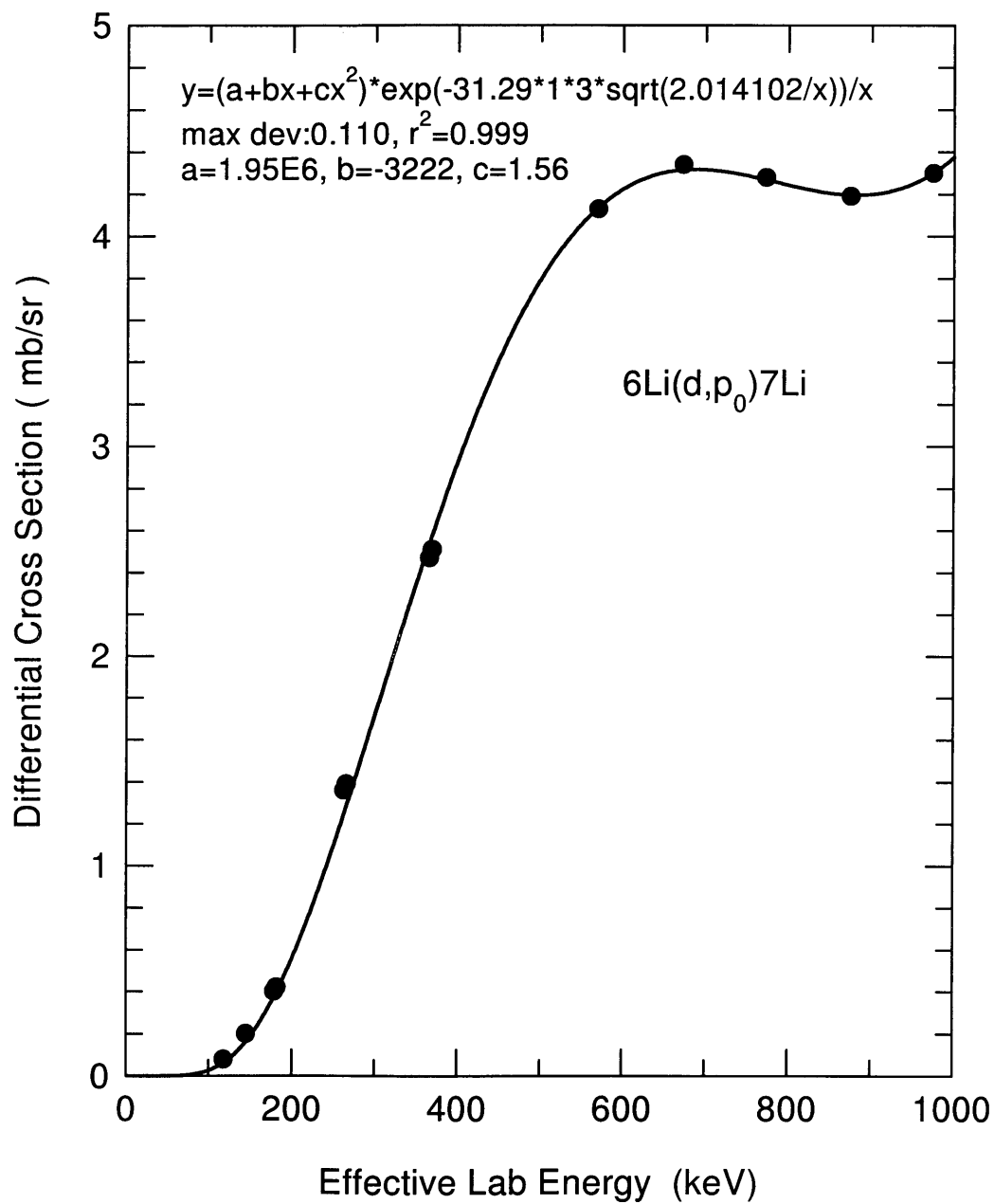


FIG. 6.10. Curve fit to the ${}^6\text{Li}(d,p_0){}^7\text{Li}$ 90° differential cross section data provided in table VI of the paper by Elwyn, et. al. [9].

Table 6.2. Experimental differential cross sections for the reaction ${}^6\text{Li}(d,n){}^7\text{Be}$. The quoted errors do not include the 7.5% systematic error.

Center-of-Momentum Effective Energy (keV)	Center-of-Momentum Angle (degrees)	Differential Cross Section (mb / sr)
94.3	0	0.250 ± 0.005
	31.0	0.262 ± 0.007
	61.8	0.249 ± 0.008
	92.1	0.253 ± 0.008

This implies negligible contributions from terms other than the s-wave. As a check, curve fits of higher order were tried. Those fits produced the same value for the constant. The coefficients of the higher order terms in those fits were approximately $\leq 1\%$ of the constant value. Integration of the differential cross section produced an absolute integral cross section of 3.17 ± 0.34 mb for the ${}^6\text{Li}(d,n){}^7\text{Be}$ reaction. This cross section agrees to within errors with the value of $2.7 \text{ mb} \pm 15\%$ given in Hirst, et. al [28]. Figure 6.12 shows the values from the current research and those published by Elwyn, et. al. [9] and by Hirst, et. al. [28]. Application of equation 6.1 to the absolute integrated cross sections of this research and to the cross sections cited in the literature produced the S-factor values shown in Figure 6.13 for the ${}^6\text{Li}(d,n){}^7\text{Be}$ reaction.

6.3 Cross sections for the direct decay reaction ${}^7\text{Li}(d,n){}^8\text{Be} \rightarrow 2\alpha$

The deuteron-induced neutron-producing reactions on ${}^7\text{Li}$ proceed through two channels to the final products of a neutron and two α -particles. The first of these channels, the direct decay, proceeds as ${}^7\text{Li}(d,n){}^8\text{Be} \rightarrow 2\alpha$. The second channel,

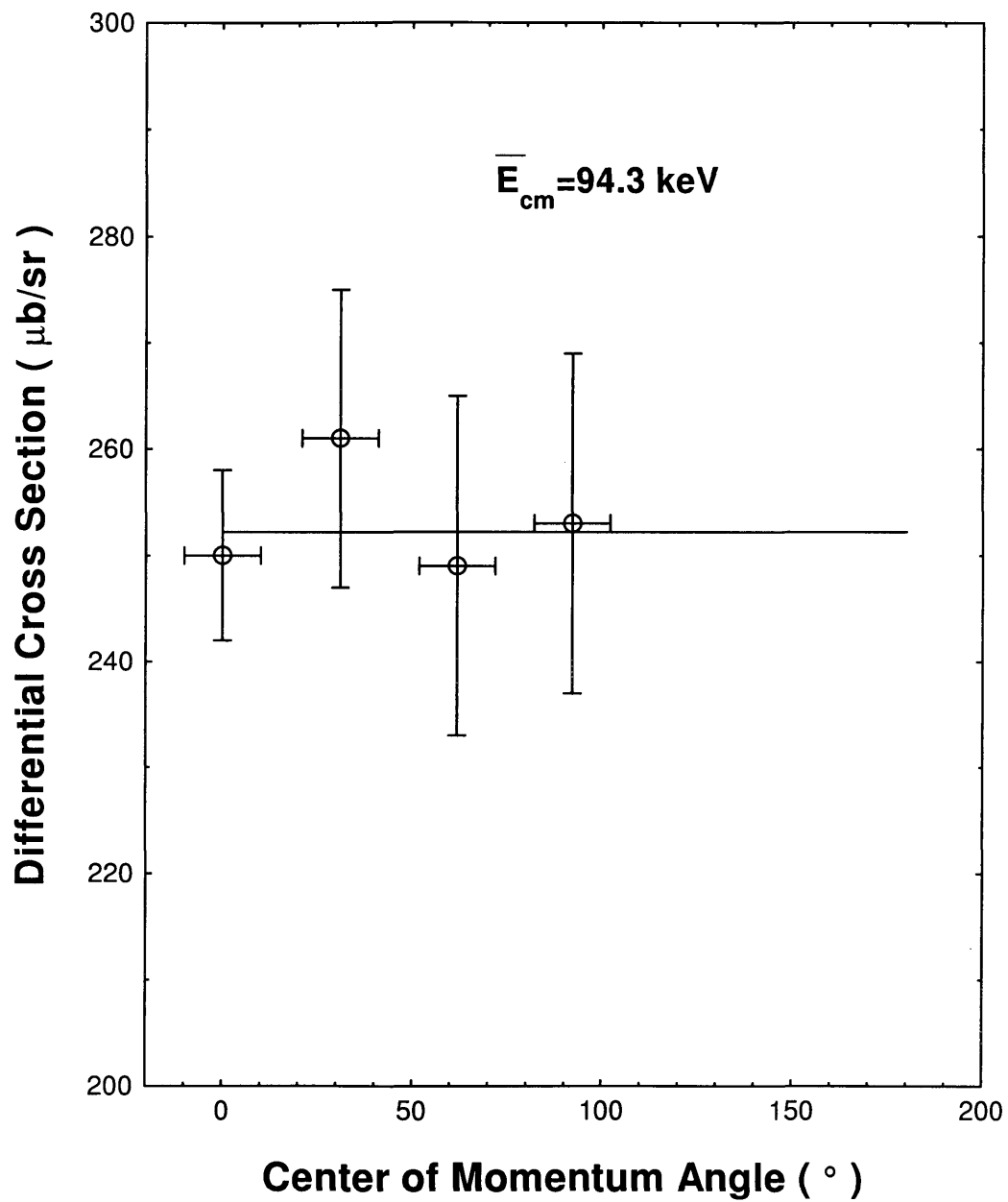


FIG. 6.11. Differential cross section for the ${}^6\text{Li}(d,n){}^7\text{Be}$ reaction. Note that the distribution is isotropic to within the errors, indicating pure s-wave contribution to the cross section.

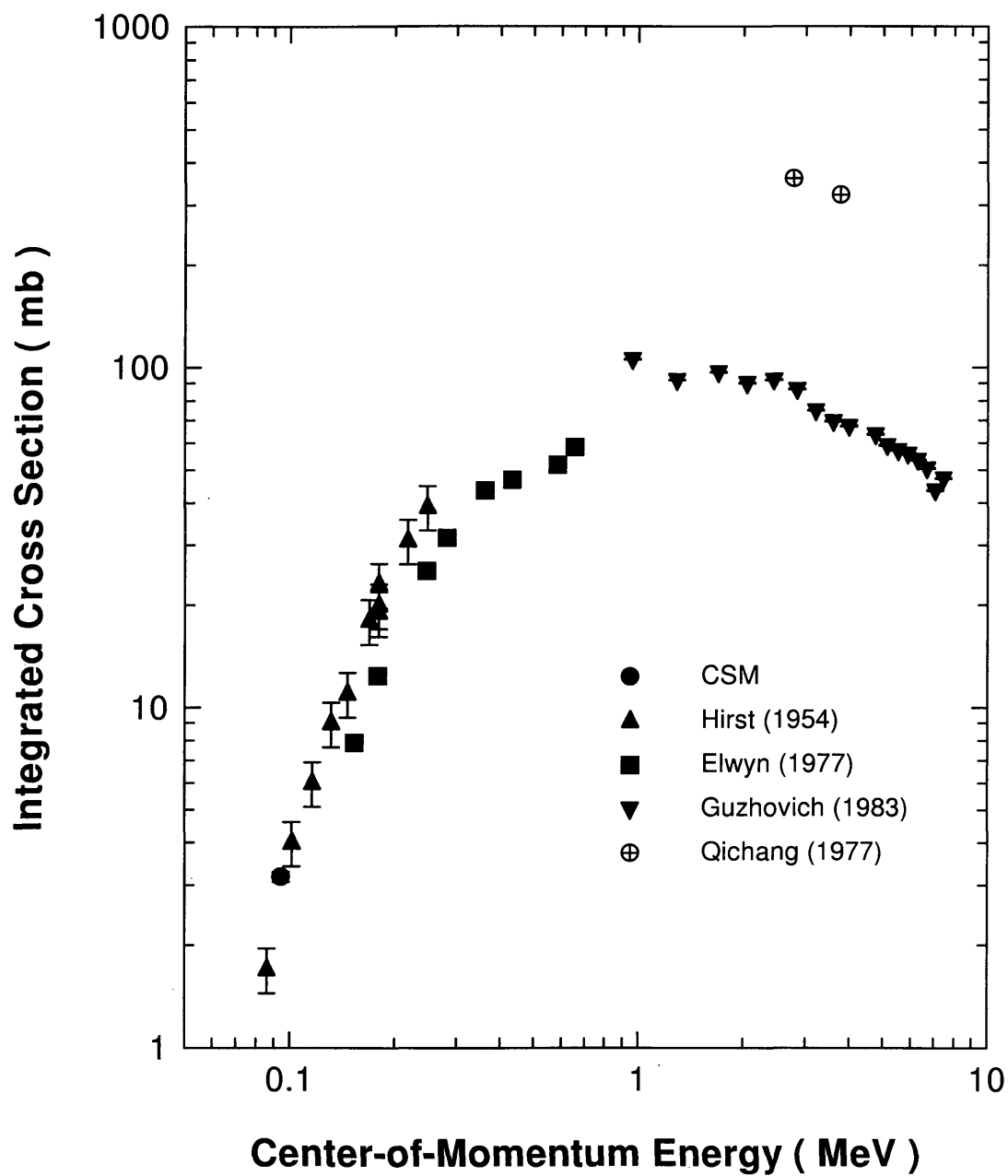


FIG. 6.12. Variation of the integrated cross section with energy for the ${}^6\text{Li}(d,n){}^7\text{Be}$ reaction in the center-of-momentum reference frame. Information regarding the data of Guzhovich and of Qichang can be found in [10] and in [11] respectively.

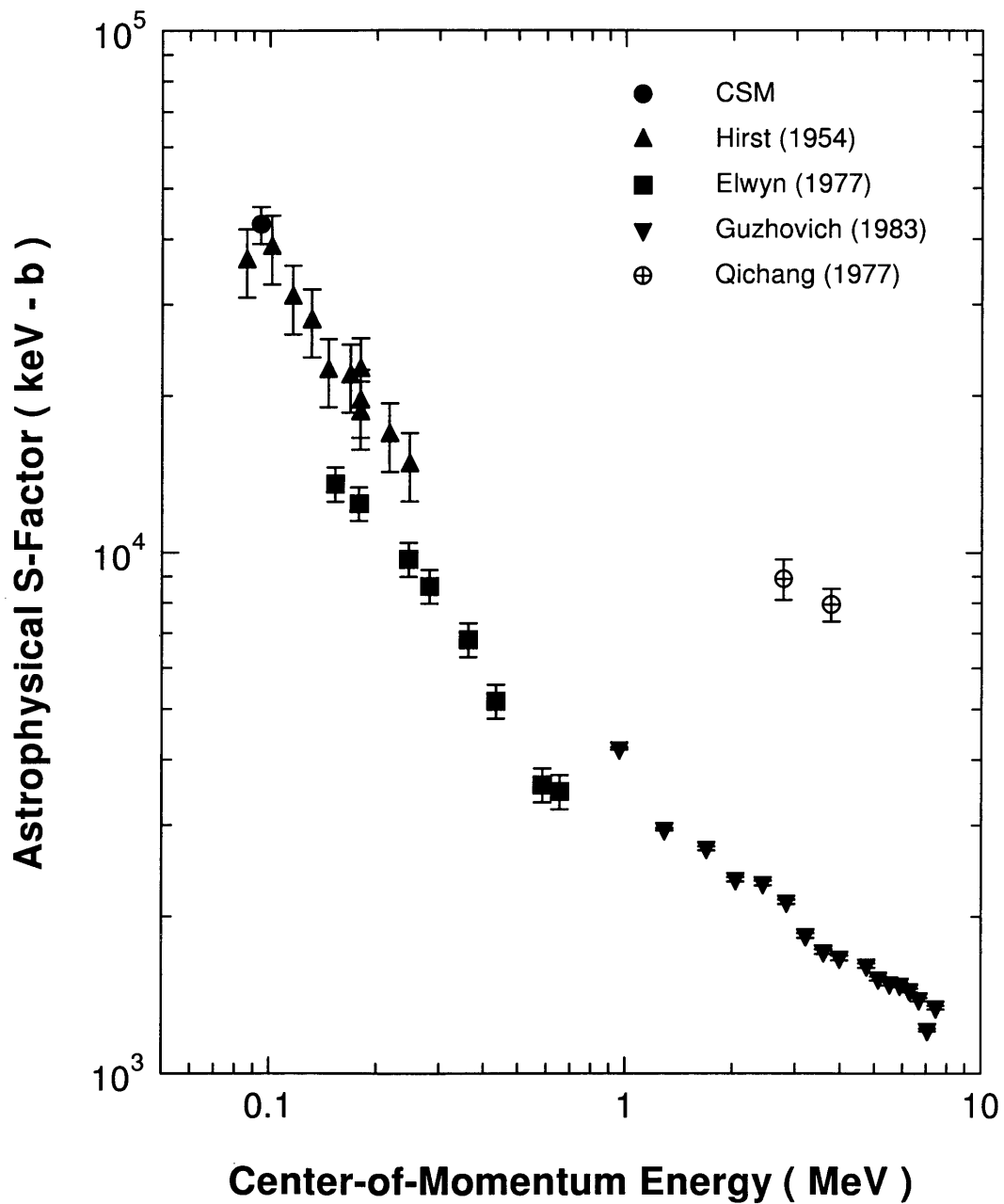


FIG. 6.13. Variation of the astrophysical S-factor with energy for the ${}^6\text{Li}(d,n){}^3\text{Be}$ reaction in the center-of-momentum reference frame.

sequential decay, proceeds as ${}^7\text{Li}(d,\alpha){}^5\text{He} \rightarrow n + \alpha$. Preliminary investigation into these reactions was completed in previous work at the Colorado School of Mines [20]. In that work, the α -particles were measured and the reaction cross sections deduced.

The charged particle spectra resulting from the direct and sequential decays were complex due to the nature of the decays. In addition, contributions from the naturally occurring ${}^6\text{Li}$ in the targets and from the deuteron accumulation in the targets complicated the spectra. The typical particle spectrum in Figure 6.14 shows these effects. Direct measurement of the neutrons circumvents the problems in extracting the cross sections from the particle spectra. In the current work, the neutrons were measured and the method of relative cross sections applied to determine the direct decay reaction cross sections.

The relative sizes of the Coulomb barriers suppresses the deuteron-induced cross sections on fluorine compared to those on lithium; therefore, pressed powder targets of lithium fluoride (LiF) were made. The natural lithium in the LiF consisted of 92.5% ${}^7\text{Li}$ and 7.5% ${}^6\text{Li}$. SRIM2000 [50] calculations of the stopping cross sections, ϵ , accounted for the presence of the fluorine and the mixture of lithium isotopes. The resulting effective stopping cross sections were used in the calculation of the effective energies as listed in Table 5.1.

As shown in the typical neutron spectrum of Figure 6.15, neutrons of energy higher than those from the deuteron + ${}^7\text{Li}$ reactions were nonexistent. The neutrons from the sequential decay reaction were not discernable in the spectra for the given neutron count statistics.

The true neutron counts for the direct decay reaction were determined in the same manner as for the ${}^2\text{H}(d,n){}^3\text{He}$ reactions. Consider the reaction at the deuteron laboratory energy of 145 keV [effective center-of-momentum energy of 100 keV] and

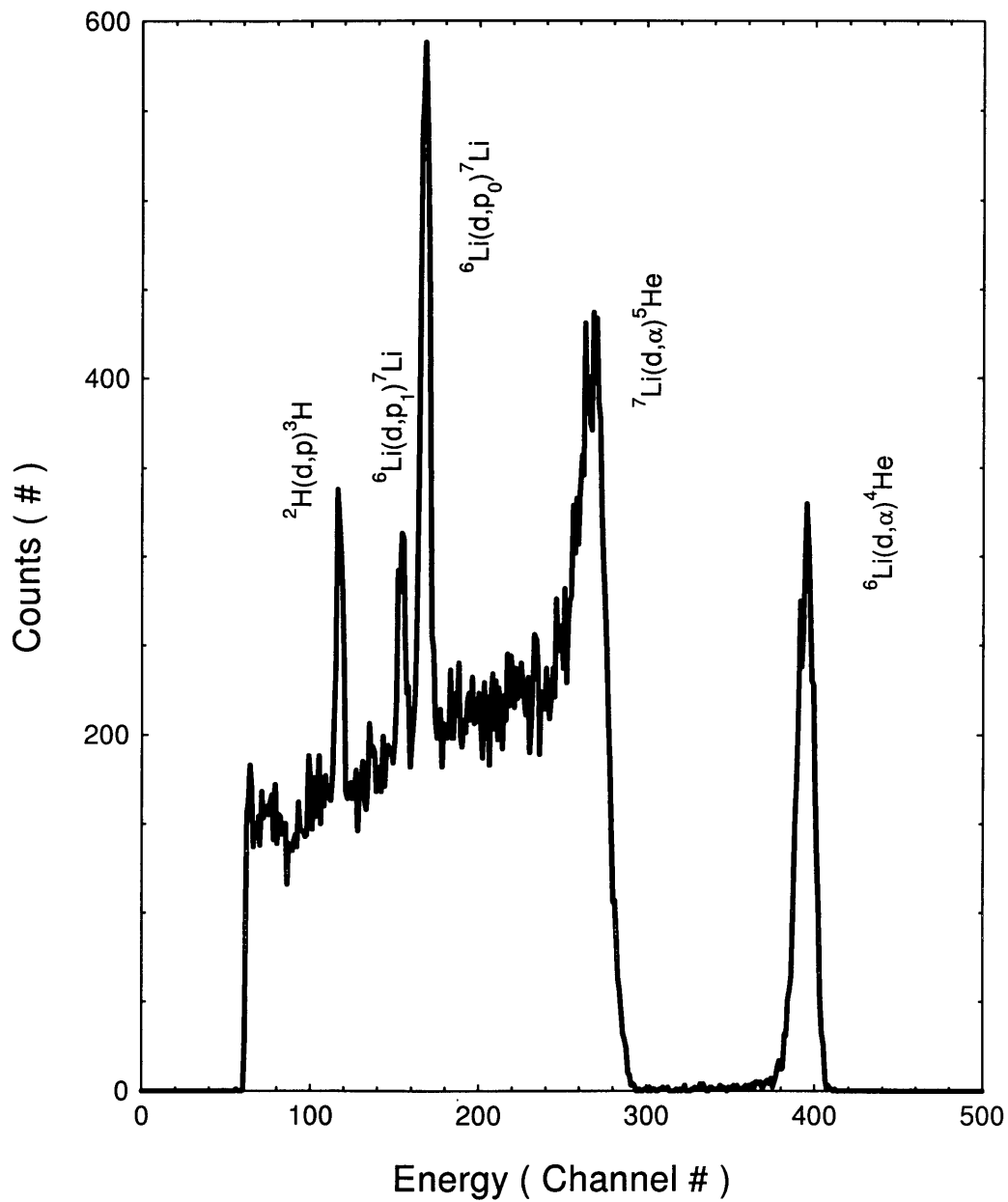


FIG. 6.14. Typical charged particle spectrum for the deuteron-induced reactions on ${}^7\text{Li}$. Note the reaction peaks from the natural abundance of ${}^6\text{Li}$ in the target.

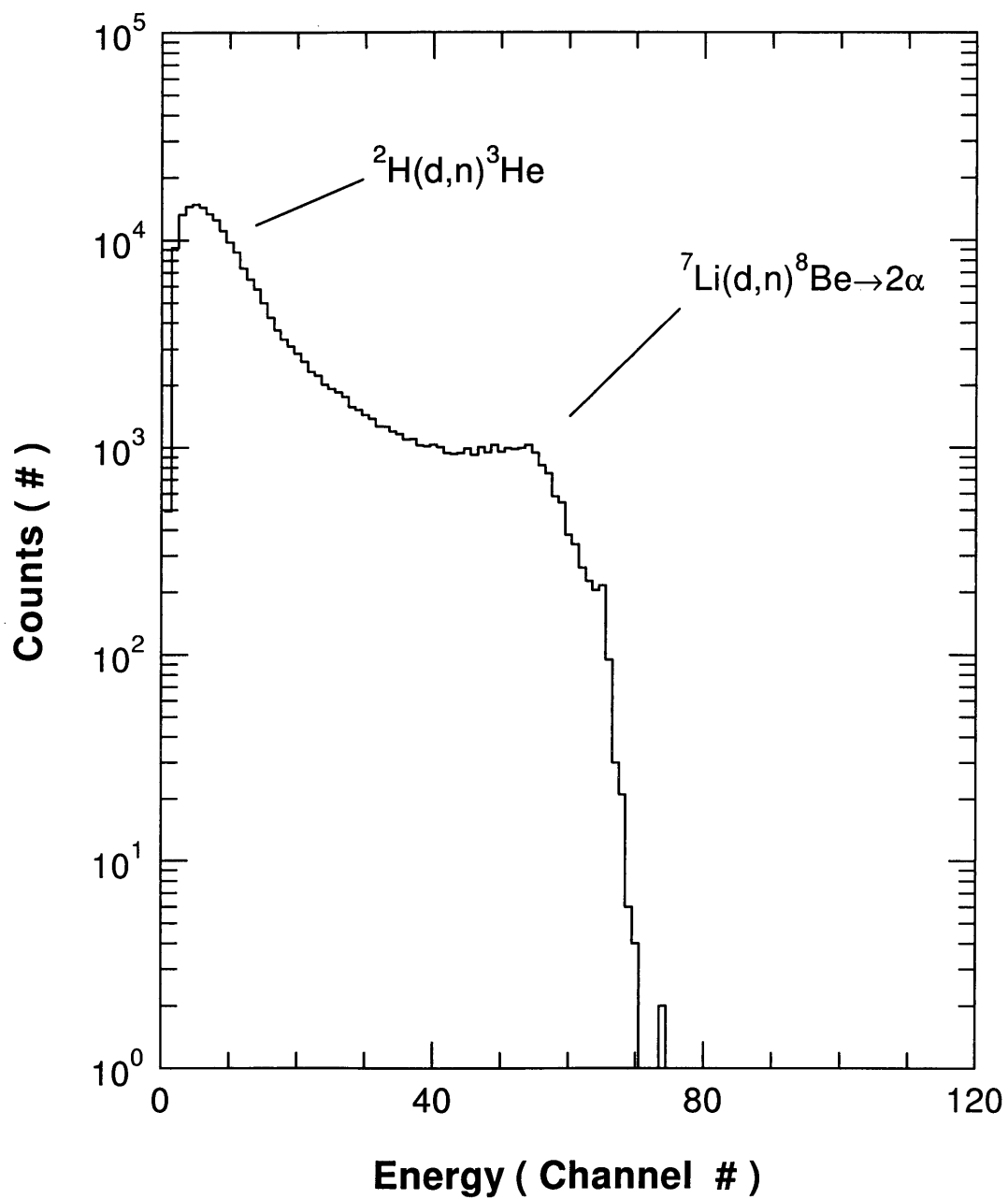


FIG. 6.15. Typical neutron spectrum for the direct decay reaction. Neutrons from the sequential decay reaction are not discernible in the spectrum.

at an angle of 0° . The maximum channel for the reaction neutrons was 62. A representative set of low-end channels consisted of all the channels from 34 to 45. The sum at each channel was divided by the corresponding integral efficiency for each channel as determined by the Kent State code. Figure 6.16 shows the summed neutron spectrum, the integral efficiency curve and the curve of neutron total counts resulting from that operation. The neutron total counts from that representative sample of channels were averaged. That average was taken to be the true neutron counts. The maximum deviation within the representative set from the average was taken to be the variance. For the current example, the average and variance were (106545 ± 4262) counts.

The relative cross section method requires known values of cross section for one reaction to determine the cross section values for the second reaction. The naturally occurring ${}^6\text{Li}$ in the target produced a ${}^6\text{Li}(d,\alpha){}^4\text{He}$ peak which had no interference from other reactions. The ${}^6\text{Li}$ produced another set of measurable reactions, the ${}^6\text{Li}(d,p_0+p_1){}^7\text{Be}$ double-peak. The α -particle continuum counts from the ${}^7\text{Li}(d,n){}^8\text{Be} \rightarrow 2\alpha$ reaction were modeled with a linear fit over the channels of the double-peak. Subtraction of the linear fit from the counts over the double-peak channels yielded the correct counts for the ${}^6\text{Li}(d,p_0+p_1){}^7\text{Be}$ reaction.

Recall the example at the deuteron laboratory energy of 145 keV [effective center-of-momentum energy of 100 keV] and at an angle of 0° . The SSB detector, which subtended a solid angle of 51.6 msr, collected the charged particle spectrum. The ${}^6\text{Li}(d,p_0+p_1){}^7\text{Be}$ double peak spanned channels 144 to 177. The linear curve fit to the α -particle continuum had a slope of 0.690 counts/channel and an intercept of 83.9 counts. The calculated α -particle continuum contributed 6621 counts to the total of 9681 counts over the ${}^6\text{Li}(d,p_0+p_1){}^7\text{Be}$ channels.

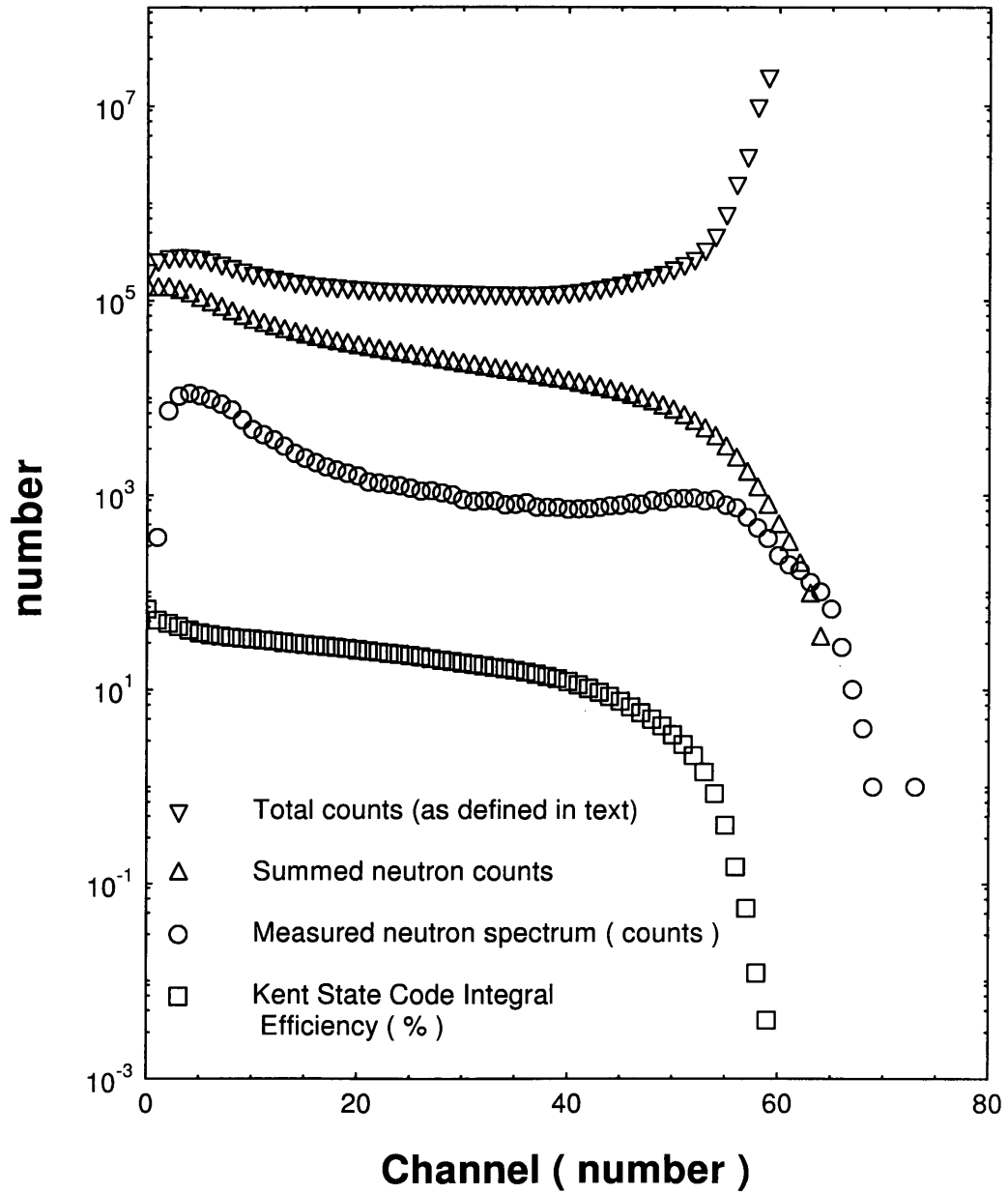


FIG. 6.16. Graphical representation of the method for determining the direct decay reaction neutron count.

The unequal abundances of ${}^6\text{Li}$ and ${}^7\text{Li}$ in the LiF target must be accounted for when calculating the cross sections for the ${}^7\text{Li}(d,n){}^8\text{Be} \rightarrow 2\alpha$ reaction. The individual isotopic number densities, $n_{6\text{Li}}$ and $n_{7\text{Li}}$, are directly proportional to the percent abundances, $n_{\%6\text{Li}}$ and $n_{\%7\text{Li}}$, of the isotopes. Substitution of these percent abundances for the target number densities into equation 5.24 gives

$$\sigma_{7\text{Li}} = \sigma_{6\text{Li}} \frac{N_{7\text{Li}} n_{\%6\text{Li}} \eta_{6\text{Li}} \Omega_{6\text{Li}}}{N_{6\text{Li}} n_{\%7\text{Li}} \eta_{7\text{Li}} \Omega_{7\text{Li}}}. \quad (6.3)$$

Returning to the example, there were $N_{7\text{Li}} = (106545 \pm 4262)$ neutron counts and $N_{6\text{Li}} = 3060$ proton counts. The detector efficiencies were already folded into these counts. The neutron detector and SSB detector subtended solid angles of 95.5 msr and 51.6 msr respectively. The isotopic abundances for ${}^6\text{Li}$ and ${}^7\text{Li}$ were 7.5% and 92.5% respectively. The absolute differential cross section for the ${}^6\text{Li}(d,p_0+p_1){}^7\text{Be}$ reaction at a laboratory angle of 90° [as interpolated from the curve fit to the data published by Elwyn et al. [9]] equaled 0.141 mb/sr. The absolute differential cross section with statistical error was $\sigma(\bar{E}_{CM} = 100 \text{ keV}, \theta_{CM} = 0^\circ) = (0.215 \pm 0.009)\text{mb/sr}$ as shown in the following calculation.

$$\begin{aligned} \sigma(100 \text{ keV}, 0^\circ) &= 0.141 \text{ mb} * \frac{(106545 \pm 4262) \text{ counts} * 7.5\% * 51.6 \text{ msr}}{3060 \text{ counts} * 92.5\% * 95.5 \text{ msr}} \\ &= (0.2151 \pm 0.0086) \text{ mb} \\ &\approx (0.215 \pm 0.009) \text{ mb}. \end{aligned}$$

The absolute differential cross sections for all angles is shown in given in Table 6.3. The errors in the table are purely statistical and do not include the 7.5% systematic error from interpolation of the ${}^6\text{Li}(d,p_0 + p_1){}^7\text{Li}$ cross section data.

Table 6.3. Experimental differential cross sections for the reaction ${}^7\text{Li}(d,n){}^8\text{Be} \rightarrow 2\alpha$. Values include statistical error only. The systematic error was 7.5%.

Center-of-Momentum Effective Energy (keV)	Center-of-Momentum Angle (degrees)	Differential Cross Section ($\mu\text{b} / \text{sr}$)
50	0	15.2 ± 0.84
	30.2	18.0 ± 0.74
	60.5	13.2 ± 0.55
	90.6	9.90 ± 0.46
83.5	0	93.0 ± 3.8
	30.3	109 ± 3.4
	60.6	113 ± 4.9
	90.7	162 ± 9.4
100	0	215 ± 8.6
	30.4	$270 \pm 11.$
	60.7	346 ± 8.1
	90.8	383 ± 8.8

The differential data were fit with curves of the form

$$\sigma(\bar{E}_{CM}, \theta_{CM}) = a + b \cos(\theta_{CM}) + c \cos^2(\theta_{CM})$$

and statistical errors were determined with the same variational method as used for the ${}^2\text{H}(d,n){}^3\text{He}$ reactions. The minimum and maximum values obtained with this method overestimated the effects of individual errors on the differential coefficients. Averaging a sample of the variations in the curve fit coefficients over combinations of the errors in the data reduced the overestimate in this propagation of the errors. The resulting differential cross section coefficients are given in Table 6.7. The values of and curve fit to the differential cross section data are shown in Figure 6.17 and 6.18.

The differential cross sections for each energy were integrated over solid angle to

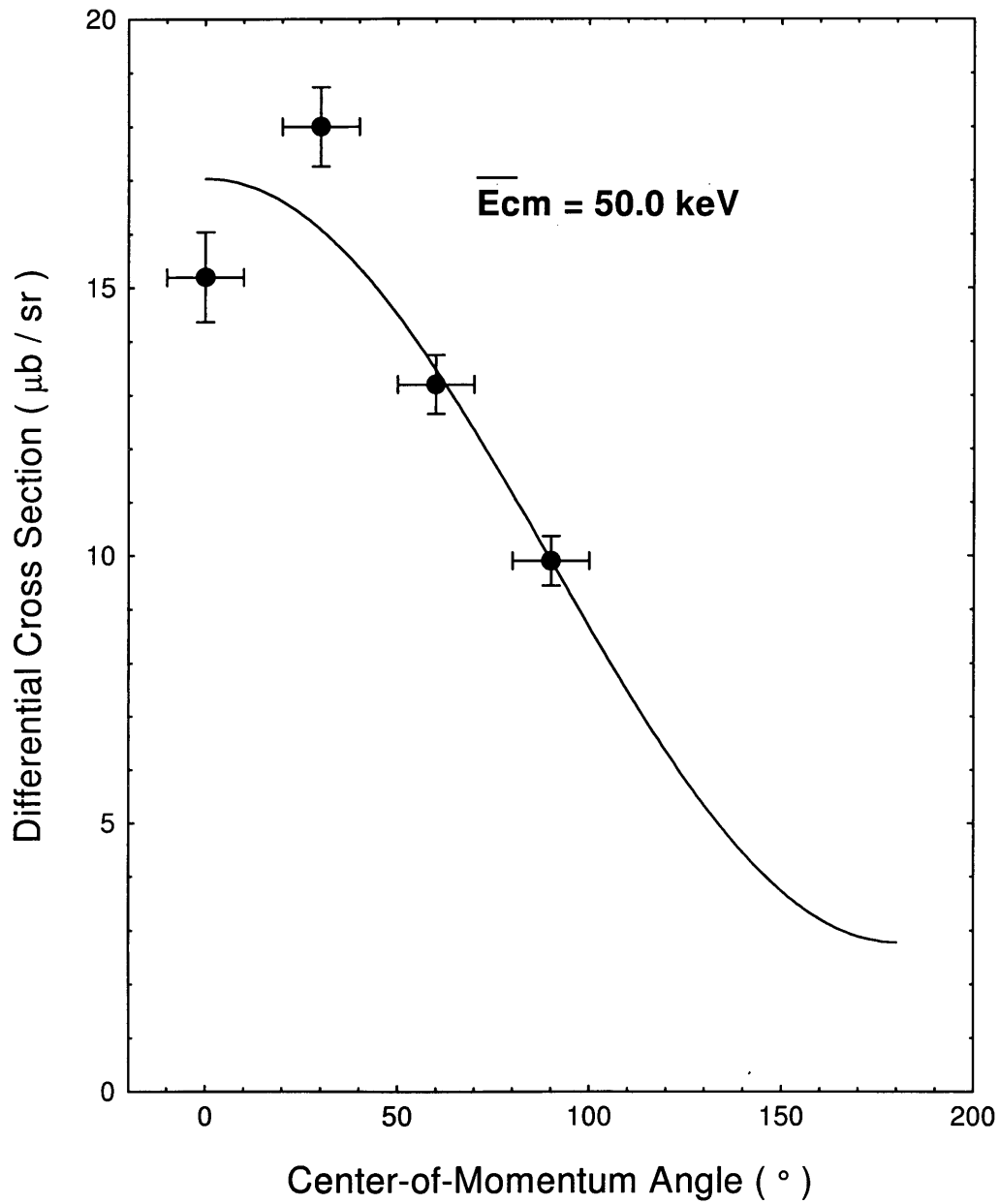


FIG. 6.17. Differential cross section for the direct decay reaction ${}^7\text{Li}(d,n){}^8\text{Be} \rightarrow 2\alpha$.

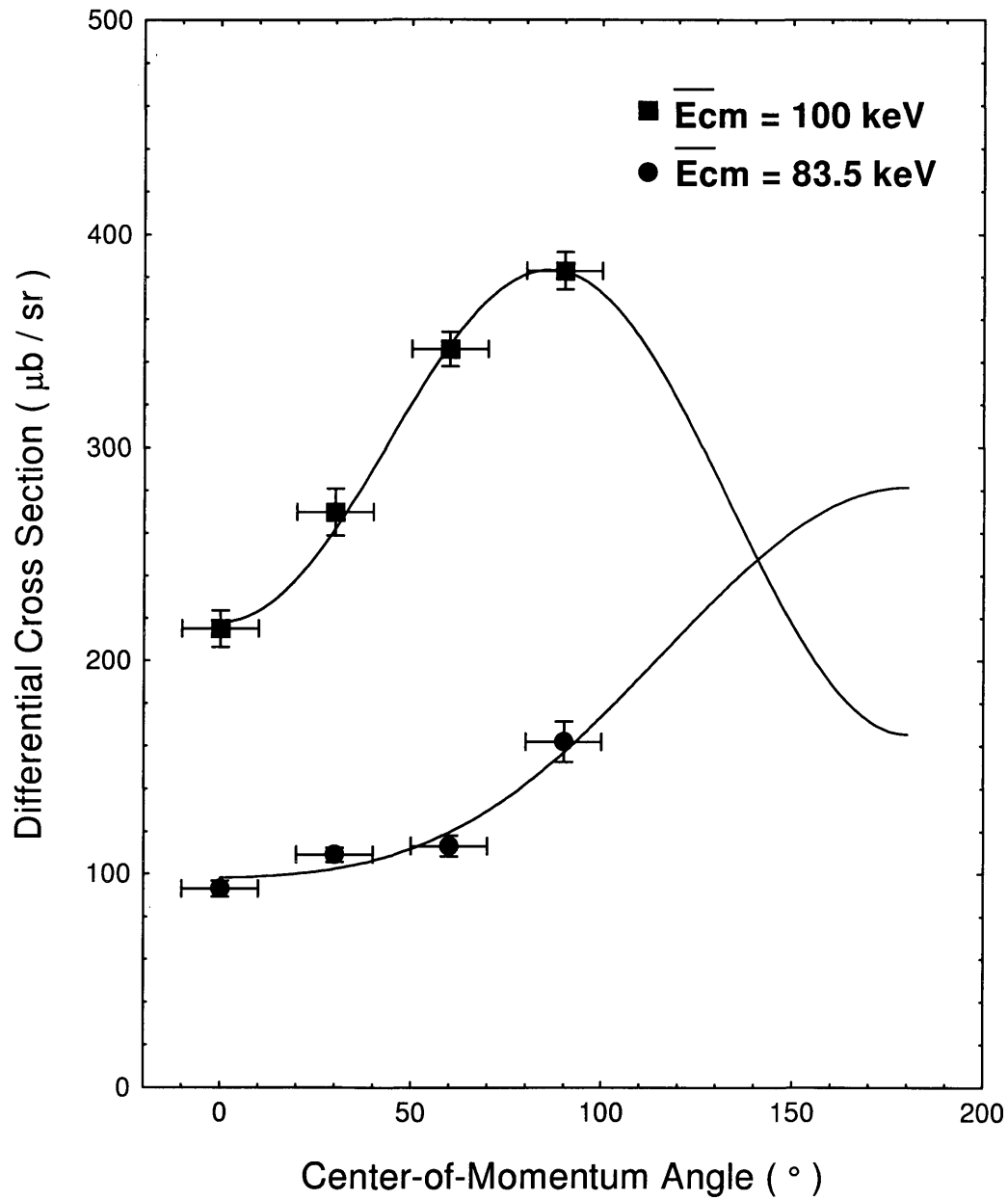


FIG. 6.18. Differential cross sections for the direct decay reaction ${}^7\text{Li}(d,n){}^8\text{Be} \rightarrow 2\alpha$.

obtain the absolute integral cross sections. The sample of differential curves used to determine the errors in the differential cross sections were integrated. The average of the minimum and maximum variance in the resulting values at each energy was designated the statistical error in the absolute cross section at each energy. The results for the integrated cross sections are listed in Table 6.8. Figure 6.19 compares the values from the current work with previously published cross sections of others. Note the approximate factor of two difference between the data in the Los Alamos report [accession # LA4851, Jarmie and Seagrove, editors] and the current work. The data was collected from a graph in a secondary source [51]. The original report was unavailable for comparison; therefore, possible differences due experimental methods could not be ascertained.

Application of equation 6.1 to the integrated cross sections of this work and other published values produced the S-factors shown in Figure 6.20.

6.4 The $^{10}\text{B}(\text{d},\text{n})^{11}\text{C}$ reaction

Yan [20] completed an examination of the (d, α) and (d,p) reactions on ^{10}B . The current work investigated the analog (d,n) reaction. The neutron spectra produced by the $^{10}\text{B}(\text{d},\text{n})^{11}\text{C}$ reaction resembled the spectra for the $^6\text{Li}(\text{d},\text{n})^7\text{Be}$ reactions. Deuterium accumulated in the pressed boron powder targets just as it had in the lithium foils. The higher energies of the neutrons from the $^{10}\text{B}(\text{d},\text{n})^{11}\text{C}$ compared to those from the $^6\text{Li}(\text{d},\text{n})^7\text{Be}$ reaction [~ 8.1 MeV vs ~ 3.3 MeV for a neutron detector angle of 0°] lessened the effect of the deuterium accumulation on the measurement of the neutron counts for the $^{10}\text{B}(\text{d},\text{n})^{11}\text{C}$ reaction as compared to the $^6\text{Li}(\text{d},\text{n})^7\text{Be}$ reaction. The isotropically enriched boron powder contained 90% ^{10}B and 10% ^{11}B . The $^{11}\text{B}(\text{d},\text{n})^{12}\text{C}$ reaction contributed non-negligible background counts to the observed

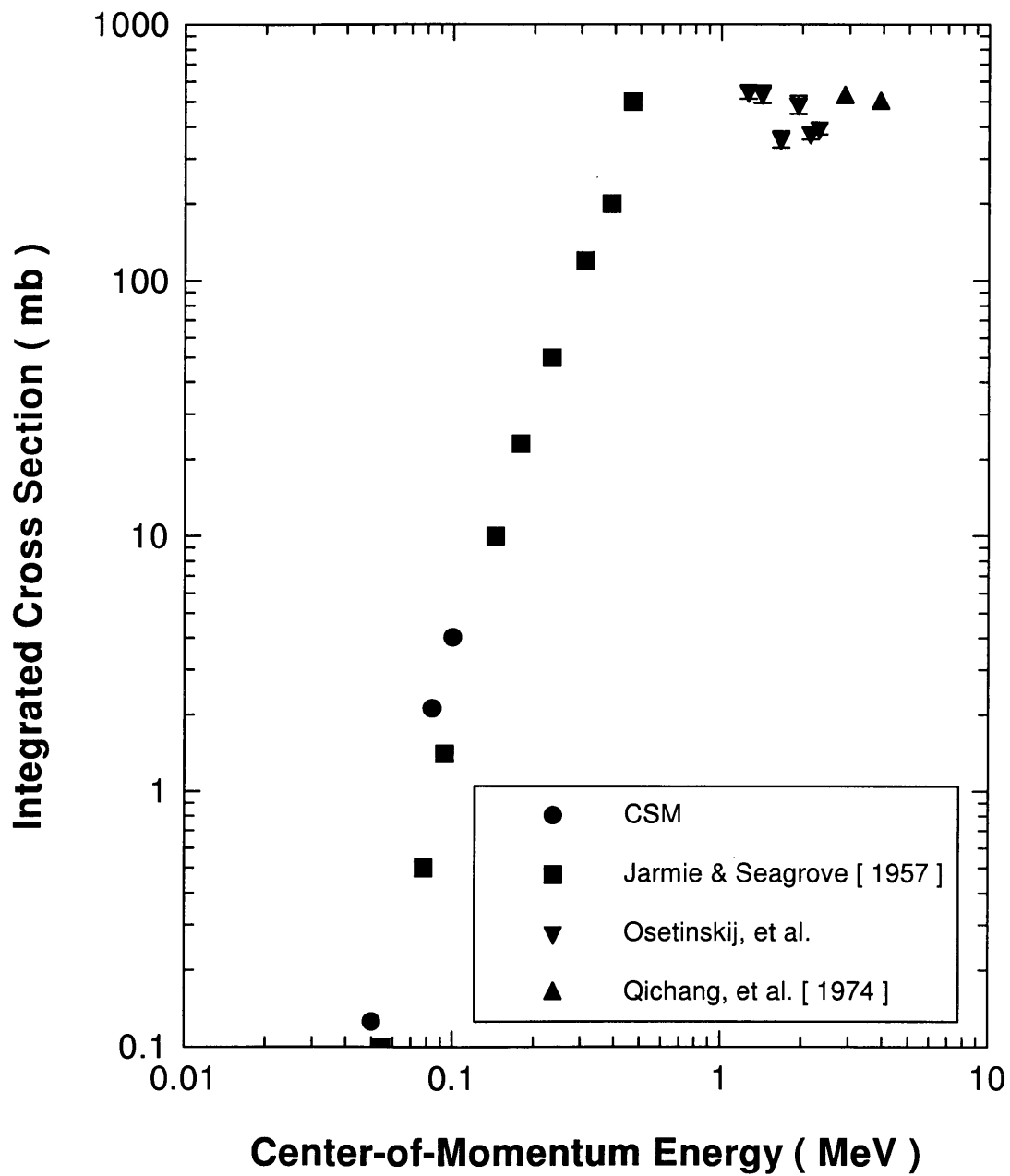


FIG. 6.19. Comparison of integrated cross sections for the direct decay reaction ${}^7\text{Li}(d,n){}^8\text{Be} \rightarrow 2\alpha$. Information regarding the data of Osetinskij and of Qichang can be found in references [12] and [11] respectively.

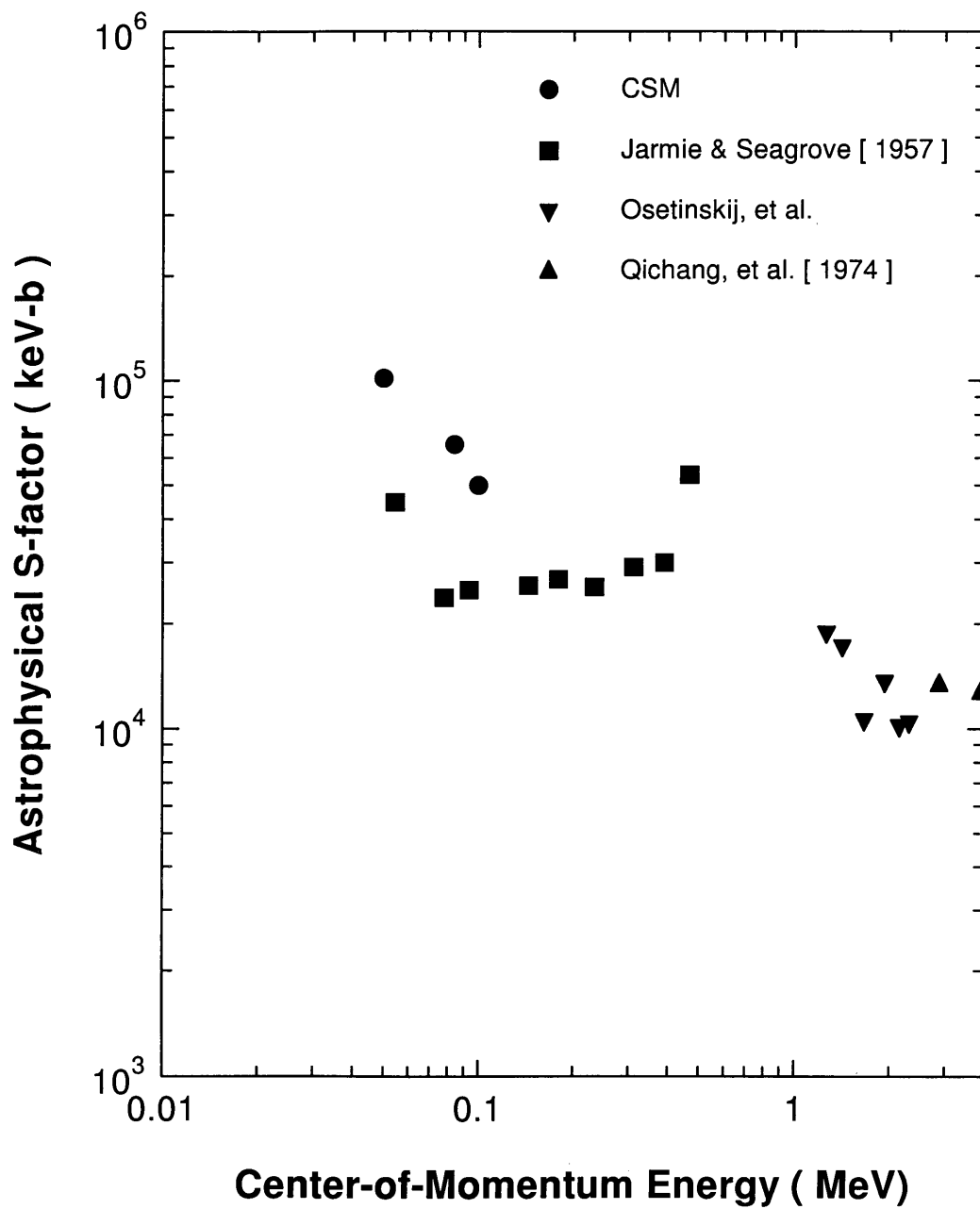


FIG. 6.20. Variation of the astrophysical S-factor with energy for the direct decay reaction ${}^7\text{Li}(d,n){}^8\text{Be} \rightarrow 2\alpha$.

neutron counts. This background was taken as constant and equal to the counts at one channel greater than the maximum channel of the $^{10}\text{B}(\text{d},\text{n})^{11}\text{C}$ reaction. These two effects are noted in the sample spectrum of Figure 6.21. Consider the $^{10}\text{B}(\text{d},\text{n})^{11}\text{C}$ reaction at the laboratory energy of 145 keV and at one angle, say 0° . The maximum channel for the reaction neutrons was 40. The $^{11}\text{B}(\text{d},\text{n})^{12}\text{C}$ reaction contributed 12 counts/channel to the total counts. The sum at each channel was divided by the corresponding integral efficiency for each channel as determined by the Kent State code. Figure 6.22 shows the summed neutron spectrum, the integral efficiency curve and the curve of neutron total counts resulting from the division. A representative set of low-end channels consisted of all the channels from 14 to 22. The neutron total counts from that representative set of channels were averaged. That average was taken to be the true neutron counts. The maximum deviation within the representative set from the average was taken to be the variance. For the current example, the average and variance were (5221 ± 273) counts. That normalized to 27.9 ± 1.5 counts/msr. Figure 6.23 shows a typical charged particle spectrum collected by the SSB detector. Note that the $^{10}\text{B}(\text{d},\alpha_0)^8\text{Be}$ peak was the only peak free of interference from α particles from the decay of the ^8Be products. Returning to the example, the angle subtended by the SSB detector as seen from the target equaled 51.6 msr. The counts from channels 460 to 512 equaled 387. The counts per steradian for the $^{10}\text{B}(\text{d},\alpha_0)^8\text{Be}$ reaction was determined to be 7.50 counts/msr as shown in the following calculation.

$$\begin{aligned} \frac{N_p}{\Omega_p \eta_p} &= \frac{387 \text{ counts} * 100 \%}{51.6 \text{ msr} * 100 \%} \\ &= 7.50 \text{ counts/msr} \end{aligned}$$

The differential cross section for the $^{10}\text{B}(\text{d},\alpha)^8\text{Be}$ reaction was determined from the

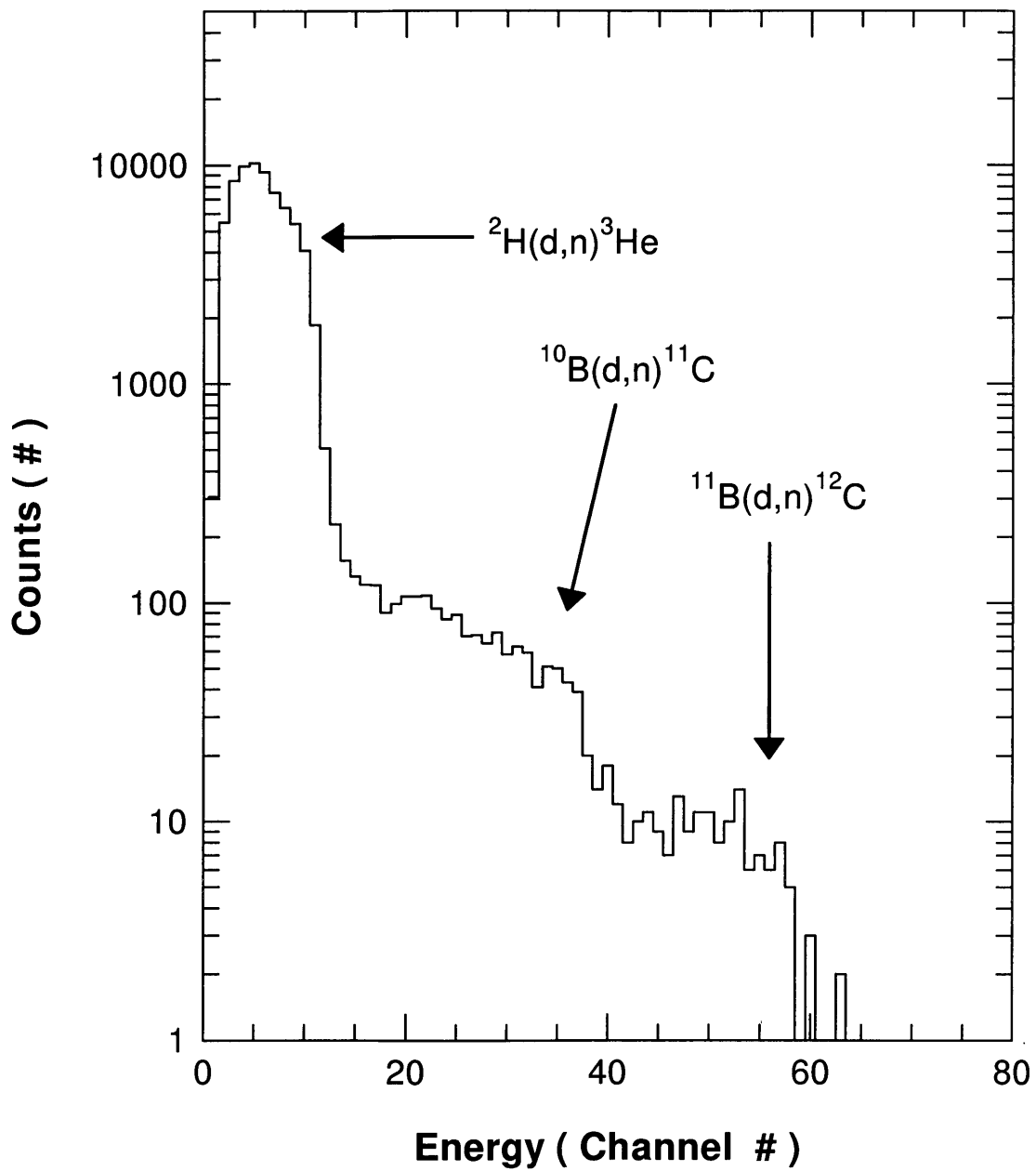


FIG. 6.21. Typical $^{10}\text{B}(\text{d},\text{n})^{11}\text{C}$ neutron spectrum. Note the contribution from the $^2\text{H}(\text{d},\text{n})^3\text{He}$ reaction and from the $^{11}\text{B}(\text{d},\text{n})^{12}\text{C}$.

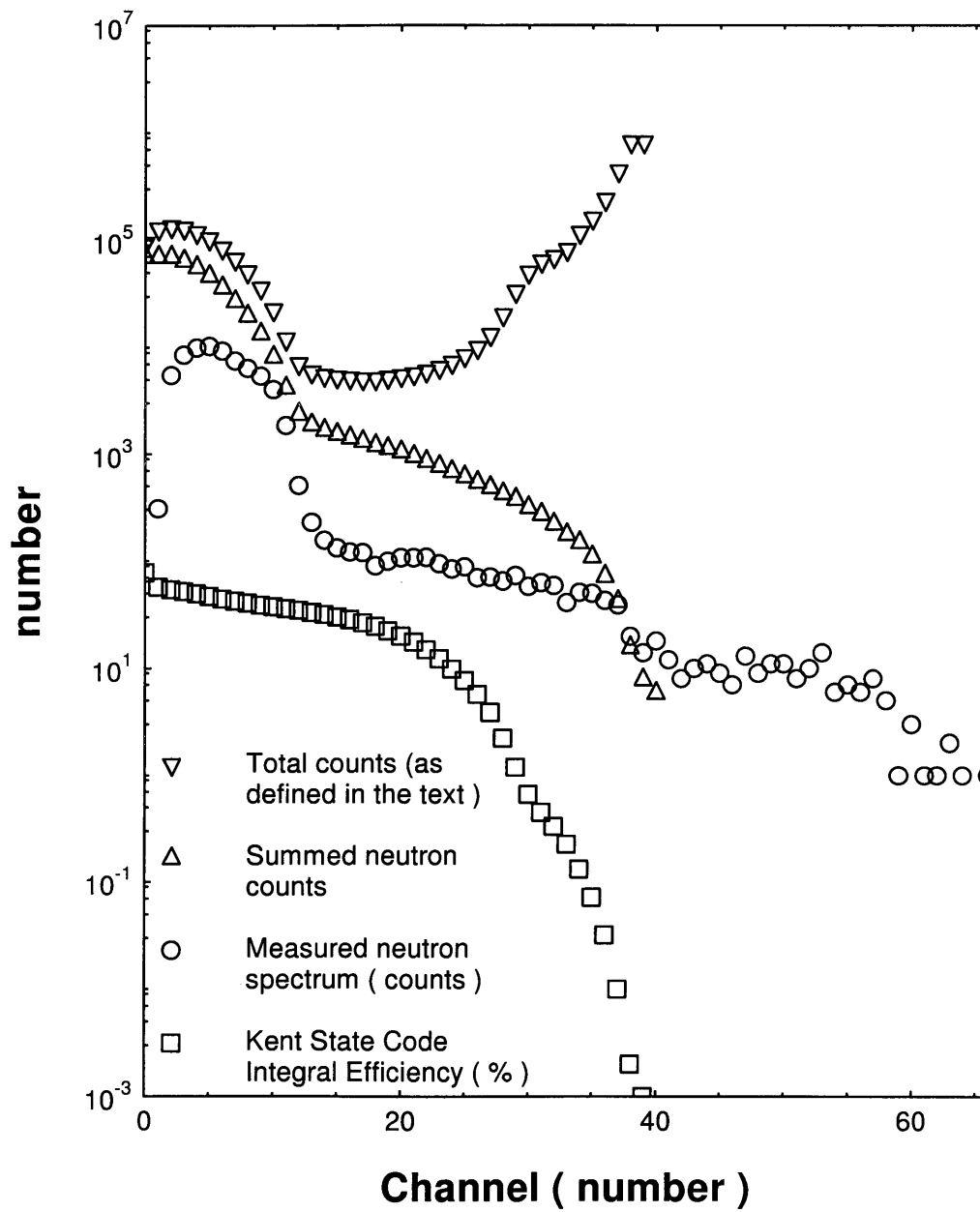


FIG. 6.22. Graphical representation of the method for determining the true neutron counts for the $^{10}\text{B}(\text{d},\text{n})^{11}\text{C}$ reaction.

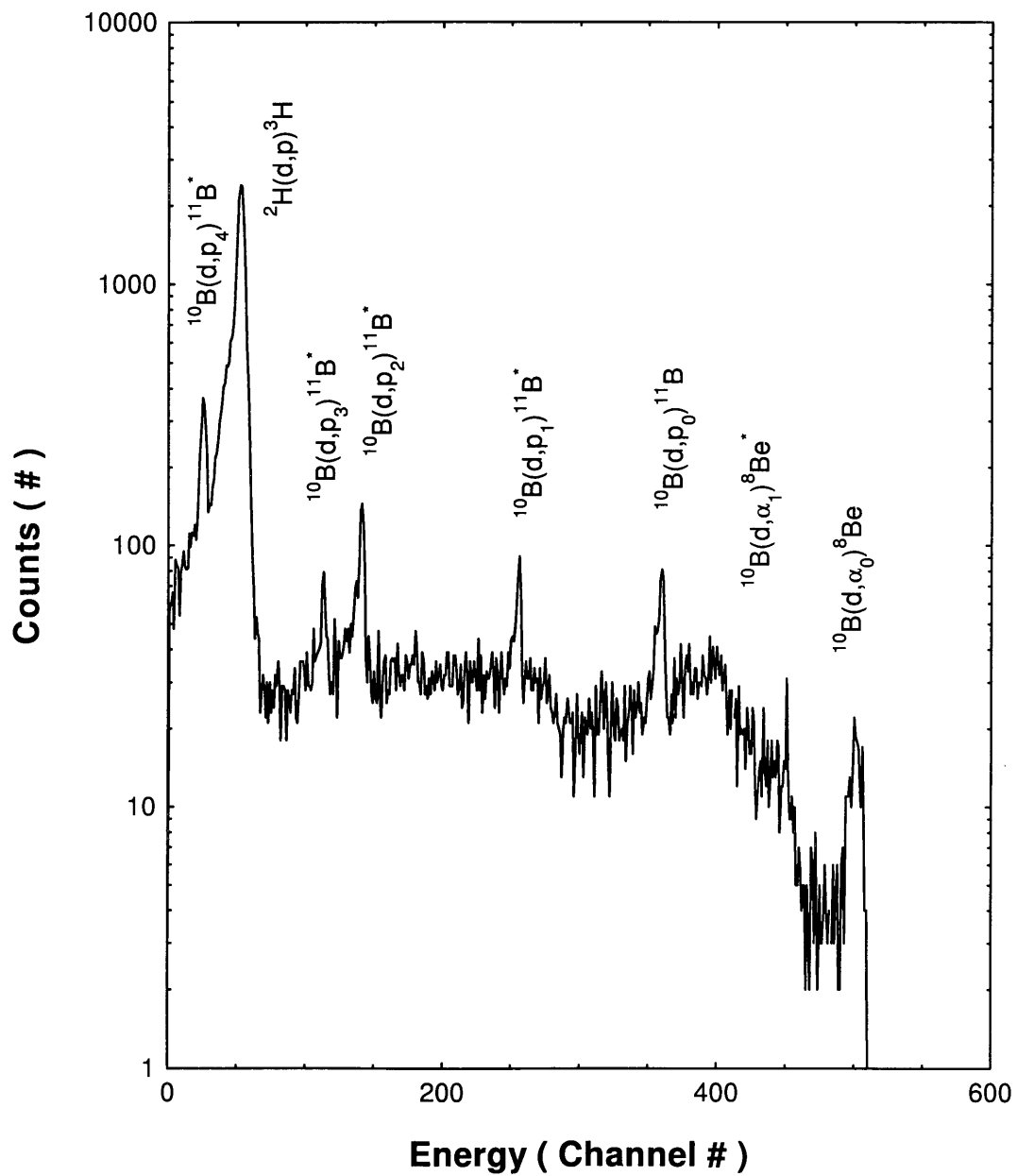


FIG. 6.23. Typical charged particle spectrum for the deuteron-induced reactions on ^{10}B .

previous work by Yan, et al. Application of equation 5.25 to the current example gives a differential cross section of $(0.167 \pm .009)$ mb/sr as shown in the following calculation. The quoted error is purely statistical.

$$\begin{aligned} \sigma(\bar{E}_{CM} = 111 \text{ keV}, \theta_{n,CM} = 0^\circ) &= \left[\frac{(27.9 \pm 1.5) \text{ counts/msr}}{7.5 \text{ counts/msr}} \right] (0.0449 \text{ } \mu\text{b/sr}) \\ &= (0.1670 \pm 0.0898) \text{ mb/sr} \\ &\approx (0.167 \pm 0.090) \text{ mb/sr} \end{aligned}$$

The absolute differential cross sections for all angles is given in Table 6.4. The errors listed do not include the $\pm 6.90\%$ systematic error from the calculation of the $^{10}\text{B}(d,\alpha_0)^8\text{Be}$ reactions.

Table 6.4. Experimental differential cross sections for the reaction $^{10}\text{B}(d,n)^{11}\text{C}$. The quoted errors are purely statistical and do not include the 6.90% systematic error.

Center-of-Momentum Effective Energy (keV)	Center-of-Momentum Angle (degrees)	Differential Cross Section (mb / sr)
111	0	0.167 ± 0.009
	30.3	0.180 ± 0.006
	60.5	0.213 ± 0.007
	90.6	0.229 ± 0.009
	120.5	0.238 ± 0.011

The differential data were fit to $\sigma(\bar{E}_{CM}, \theta_{CM}) = a + b \cos(\theta_{CM}) + c \cos^2(\theta_{CM})$ and statistical errors were determined with the same variational method as used for the $^2\text{H}(d,n)^3\text{He}$ reactions. The minimum and maximum values obtained with this method overestimated the effects of individual errors on the differential coefficients. Averaging a sample of the variations in the curve fit coefficients over combinations of

the errors in the data reduced the overestimate in this propagation of the errors. The resulting differential cross section coefficients are given in Table 6.7. The values of and curve fit to the differential cross section data are shown in Figure 6.24. Figure 6.25 compares the values of integrated cross section from the current research to published values over a range of energies.

Application of equation 6.1 to the absolute integrated cross sections of this research and to the cross sections cited in the literature produced the S-factor values shown in Figure 6.26 for the $^{10}\text{B}(\text{d},\text{n})^{11}\text{C}$ reaction.

6.5 The $^{11}\text{B}(\text{d},\text{n})^{12}\text{C}$ reaction.

Previous work at the Colorado School of Mines investigated the $^{11}\text{B}(\text{d},\text{p})^{12}\text{B}$ reaction [7]. The analog $^{11}\text{B}(\text{d},\text{n})^{12}\text{C}$ reaction was included in this work to complement that previous work and for the possible applications in fusion diagnostics. The neutron spectrum of the analog $^{11}\text{B}(\text{d},\text{n})^{12}\text{C}$ reaction resembles the spectrum from the $^7\text{Li}(\text{d},\text{n})^8\text{Be}$ spectrum. Deuterium accumulates in the pressed powder boron targets. The natural boron powder consisted of 80.2% ^{11}B and 19.8% ^{10}B . Contributions from the naturally occurring $^{10}\text{B}(\text{d},\text{n})^{11}\text{C}$ reaction set the minimum possible lower limit for the representative set of channels. The typical neutron spectrum in Figure 6.27 shows these effects. As also seen in that neutron spectrum, contributions from neutrons of energy higher than those from the $^{11}\text{B}(\text{d},\text{n})^{12}\text{C}$ reactions were negligible.

The true neutron counts for the $^{11}\text{B}(\text{d},\text{n})^{12}\text{C}$ reaction were determined in the same manner as for the $^7\text{Li}(\text{d},\text{n})^8\text{Be}$ reaction. Consider the reaction at the deuteron laboratory energy of 145 keV [effective center-of-momentum energy of 112 keV] and at an angle of 0° . The maximum channel for the reaction neutrons was 57. A representative set of low-end channels consisted of all the channels from 27 to 41.

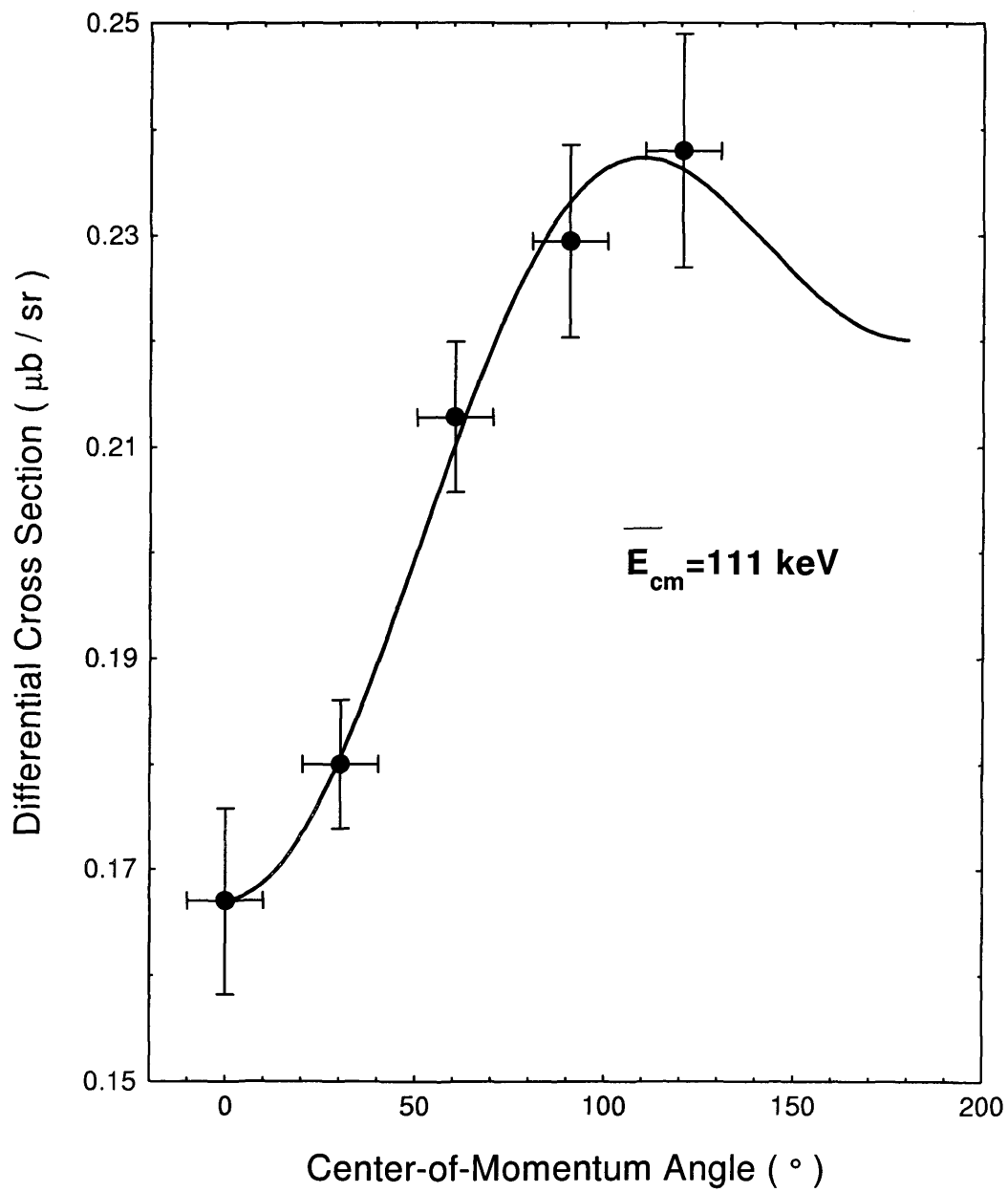


FIG. 6.24. Differential cross section for the $^{10}\text{B}(\text{d},\text{n})^{11}\text{C}$ reaction.

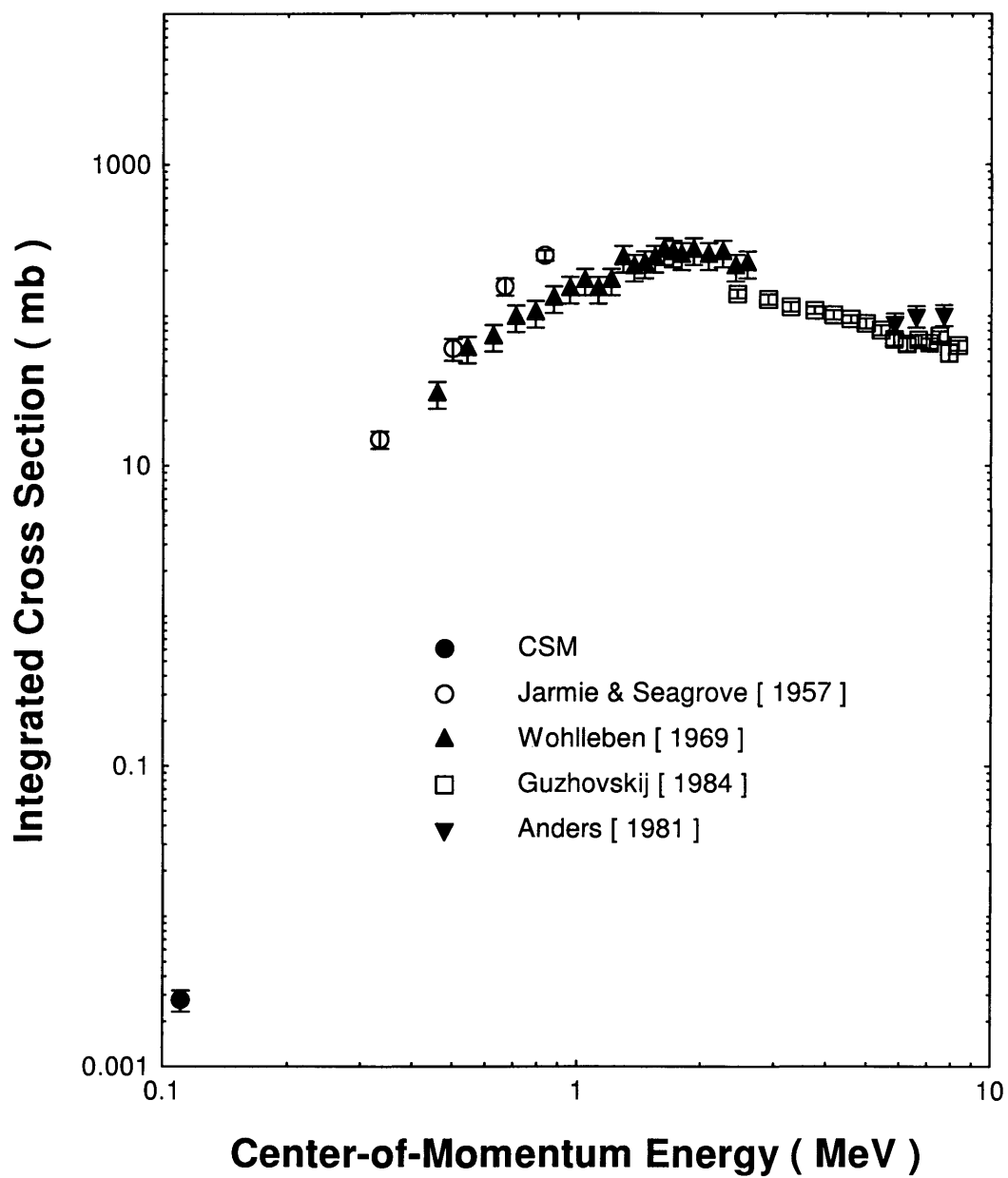


FIG. 6.25. Variation of the integrated cross section with energy for the $^{10}\text{B}(d,n)^{11}\text{C}$ reaction. Information regarding the data of Wohlleben and of Guzhovskij and of Anders can be found in references [13] and [14] and [15] respectively.

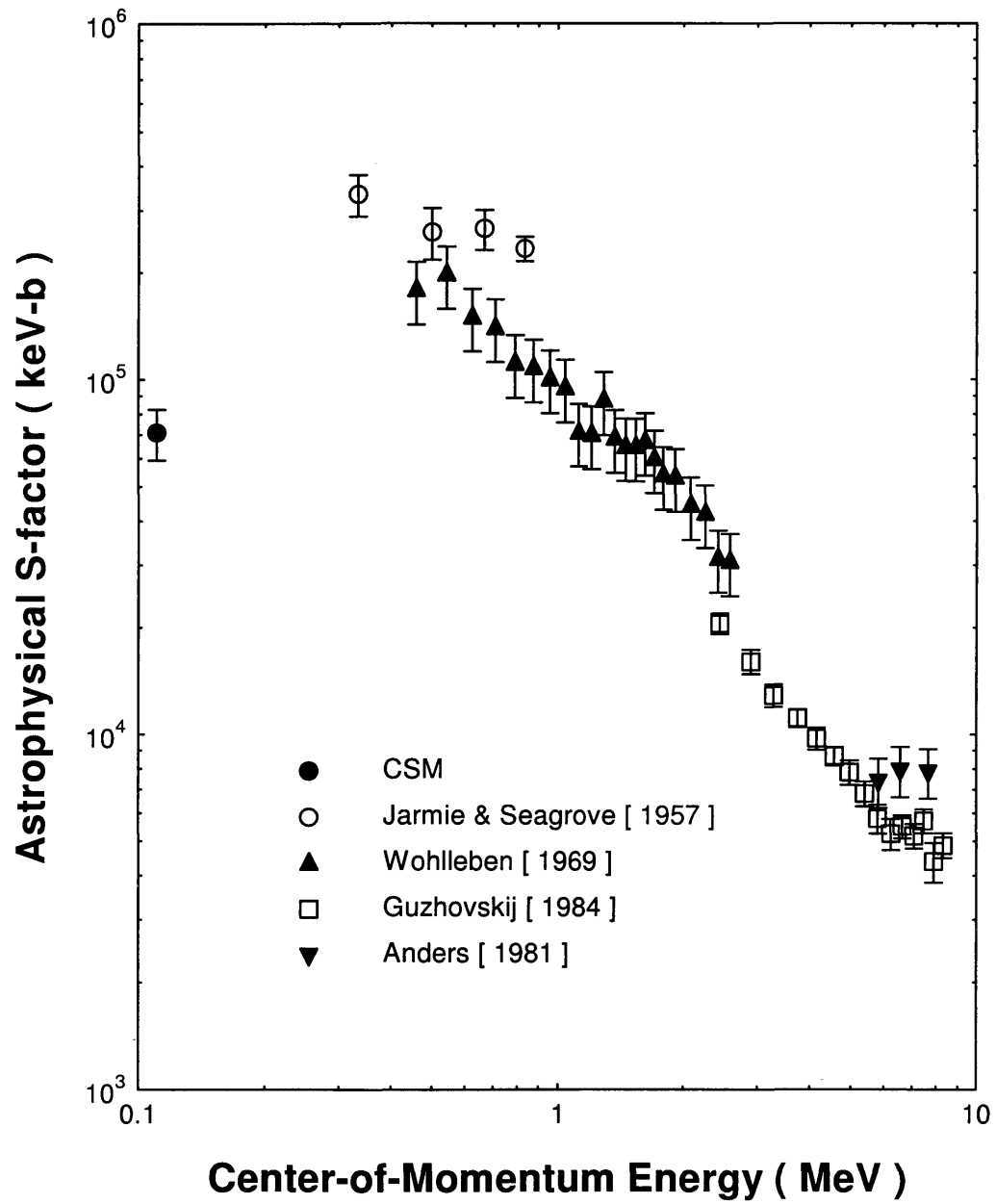


FIG. 6.26. Variation of the astrophysical S-factor with energy for the $^{10}\text{B}(d,n)^{11}\text{C}$ reaction.

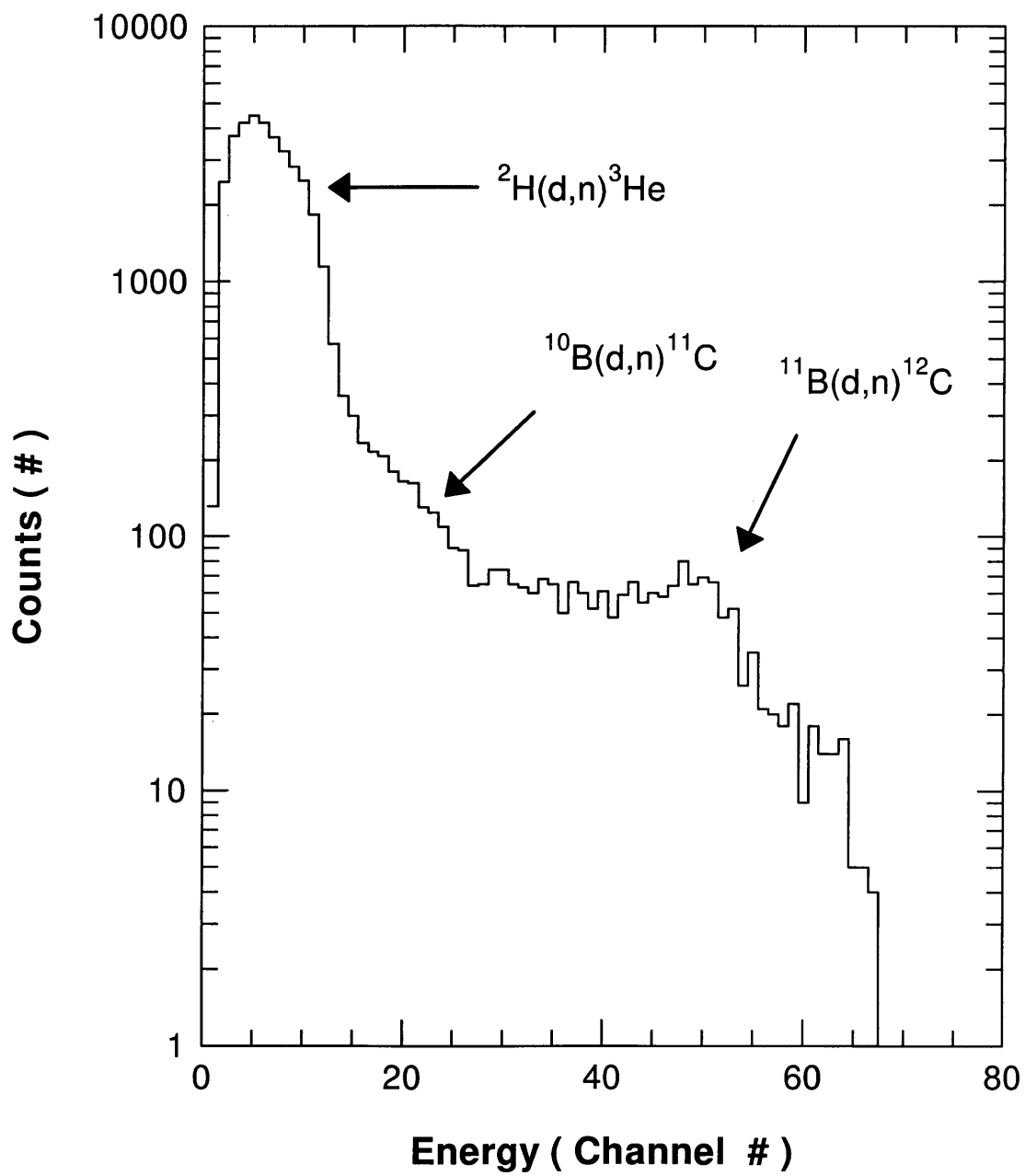


FIG. 6.27. Typical neutron spectrum for the ${}^{11}\text{B}(d,n){}^{12}\text{C}$ reaction. Note the presence of neutrons from the ${}^{10}\text{B}(d,n){}^{11}\text{C}$ reactions.

The sum at each channel was divided by the corresponding integral efficiency for each channel as determined by the Kent State code. Figure 6.28 shows the summed neutron spectrum, the integral efficiency curve and the curve of neutron total counts resulting from that operation. The neutron total counts from that representative sample of channels were averaged. That average was taken to be the true neutron counts. The maximum deviation within the representative set from the average was taken to be the variance. For the current example, the average and variance were (8432 ± 266) counts.

The naturally occurring ^{10}B in the target produced a $^{10}\text{B}(\text{d},\alpha_0)^8\text{Be}$ peak. The peak overlapped slightly with the high-end tail of the $^{10}\text{B}(\text{d},\alpha_1)^8\text{Be}$ peak as shown in Figure 6.29. The differential cross section for this reaction had been previously determined by Yan [7] at numerous energies. Following the method employed by Yan, the values of the angular distribution function and S-factor were calculated from the coefficients in tables 3.3 and 3.4 in [7]. The differential cross section at 90° and center-of-momentum energy of 123 keV was then determined to be equal to $(4.49 \pm .31) * 10^{-2} \mu\text{b}$.

Recall the example at the deuteron laboratory energy of 145 keV [effective center-of-momentum energy of 100 keV] and at an angle of 0° . The SSB detector subtended a solid angle of 51.6 msr. The $^{10}\text{B}(\text{d},\alpha_1)^8\text{Be}$ peak contributed 10 counts to the total of 69 counts over the channels 374 to 390.

The unequal abundances of ^{10}B and ^{11}B in the natural boron target must be accounted for when calculating the cross sections. The individual isotopic number densities, $n_{10\text{B}}$ and $n_{11\text{B}}$, are directly proportional to the percent abundances, $n_{\%10\text{B}}$ and $n_{\%11\text{B}}$, of the isotopes. Substitution of these percent abundances for the target

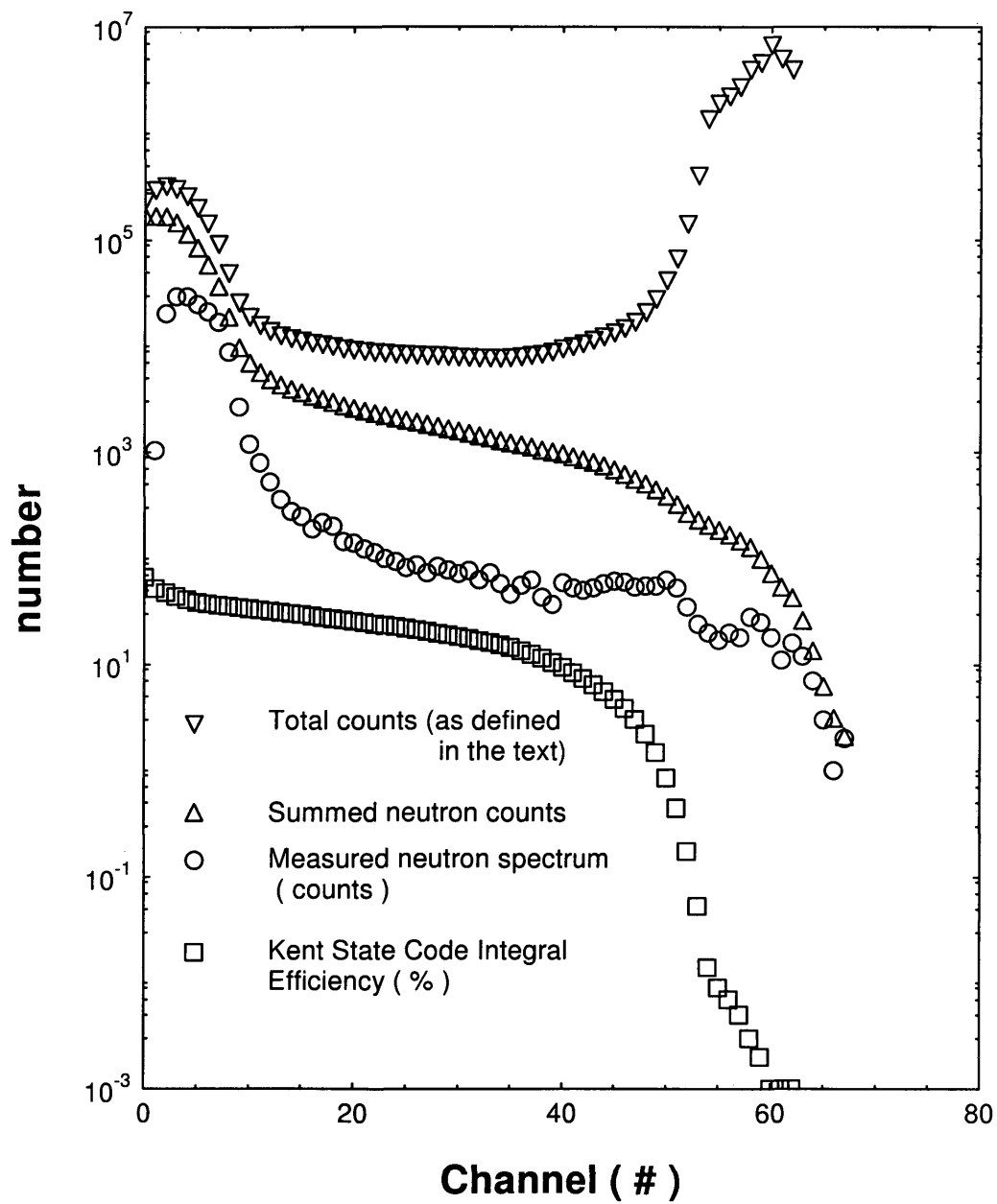


FIG. 6.28. Graphical representation of the method for determining the direct decay reaction neutron count.

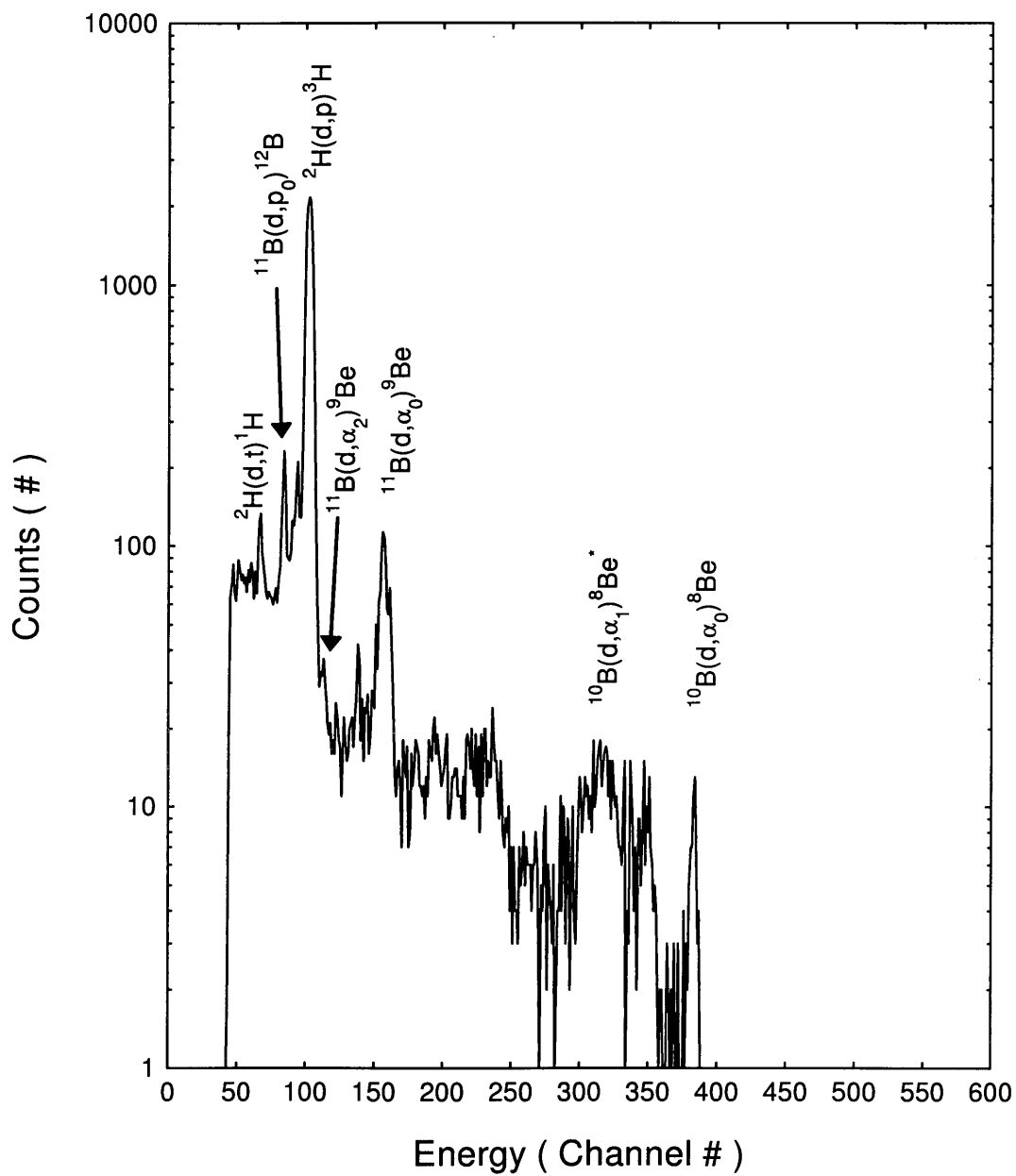


FIG. 6.29. Typical charged particle spectrum for the deuteron-induced reactions on naturally occurring boron. Note the presence of reaction products from the ${}^{10}\text{B}$ in the target.

number densities into equation 5.24 gives

$$\sigma_{11B} = \sigma_{10B} \frac{N_{11B} n_{\%10B} \eta_{10B} \Omega_{10B}}{N_{10B} n_{\%11B} \eta_{11B} \Omega_{11B}} \quad (6.4)$$

Returning to the example, there were $N_{11B} = (8432 \pm 266)$ neutron counts and $N_{10B} = 59 \alpha_0$ counts. The detector efficiencies were already folded into these counts. The neutron detector and SSB detector subtended solid angles of 95.5 msr and 51.6 msr respectively. The isotopic abundances for ^{10}B and ^{11}B were 19.8% and 80.2% respectively. The absolute differential cross section for the $^{10}\text{B}(d,\alpha_0)^{11}\text{C}$ reaction at a laboratory angle of 90° equaled $(0.0449 \pm 0.0031) \mu\text{b}/\text{sr}$. The absolute differential cross section with statistical error was $\sigma(\bar{E}_{CM} = 112\text{keV}, \theta_{CM} = 0^\circ) = (0.437 \pm 0.014) \mu\text{b}/\text{sr}$ as shown in the following calculation:

$$\begin{aligned} \sigma(112 \text{ keV}, 0^\circ) &= 0.0449 \mu\text{b} * \frac{(8432 \pm 266) \text{ counts} * 19.8\% * 51.6 \text{ msr}}{59 \text{ counts} * 80.2\% * 187 \text{ msr}} \\ &= (0.4367 \pm 0.0138) \mu\text{b} \\ &\approx (0.437 \pm 0.014) \mu\text{b}. \end{aligned}$$

The absolute differential cross sections for all angles is given in Table 6.5. The errors in the table are purely statistical and do not include the 6.90% systematic error from the calculation of the $^{10}\text{B}(d,\alpha_0)^8\text{Be}$ cross section.

The differential data were fit to $\sigma(\bar{E}_{CM}, \theta_{CM}) = a + b \cos(\theta_{CM}) + c \cos^2(\theta_{CM})$ and statistical errors were determined with the same variational method as used for the $^2\text{H}(d,n)^3\text{He}$ reactions. The minimum and maximum values obtained with this method overestimated the effects of individual errors on the differential coefficients. Averaging a sample of the variations in the curve fit coefficients over combinations of the errors in the data reduced the overestimate in this propagation of the errors. The resulting

Table 6.5. Experimental differential cross sections for the $^{11}\text{B}(d,n)^{12}\text{C}$ reaction. Values include statistical error only. The systematic error was 6.90%.

Center-of-Momentum Effective Energy (keV)	Center-of-Momentum Angle (degrees)	Differential Cross Section ($\mu\text{b} / \text{sr}$)
112	0	0.437 ± 0.014
	30.5	0.500 ± 0.030
	60.9	0.610 ± 0.023
	91.0	0.660 ± 0.047
	121	0.768 ± 0.028

differential cross section coefficients are given in Table 6.7. The values of and curve fit to the differential cross section data are shown in Figure 6.30. The differential cross section was integrated over solid angle to obtain the absolute integral cross section. The sample of differential curves used to determine the errors in the differential cross sections were integrated. The average of the minimum and maximum variance in the resulting values was designated the statistical error in the absolute cross sections. The results for the integrated cross section is listed in Table 6.8. Figure 6.31 compares the value from the current work with previously published cross sections of others.

Application of equation 6.1 to the integrated cross sections of this work and other published values produced the S-factors shown in Figure 6.32.

6.6 Observation of the ^{10}B final states from deuteron-induced proton transfer reactions on ^9Be .

The neutron spectrum of deuteron-induced proton transfer reaction on ^9Be was unique among the reactions in this research. Four distinct contributions were evident in the spectra. Deuterons accumulated in the beryllium target as in all the other targets. The $^2\text{H}(d,n)^3\text{He}$ reaction is visible below channel 13 in the typical neutron

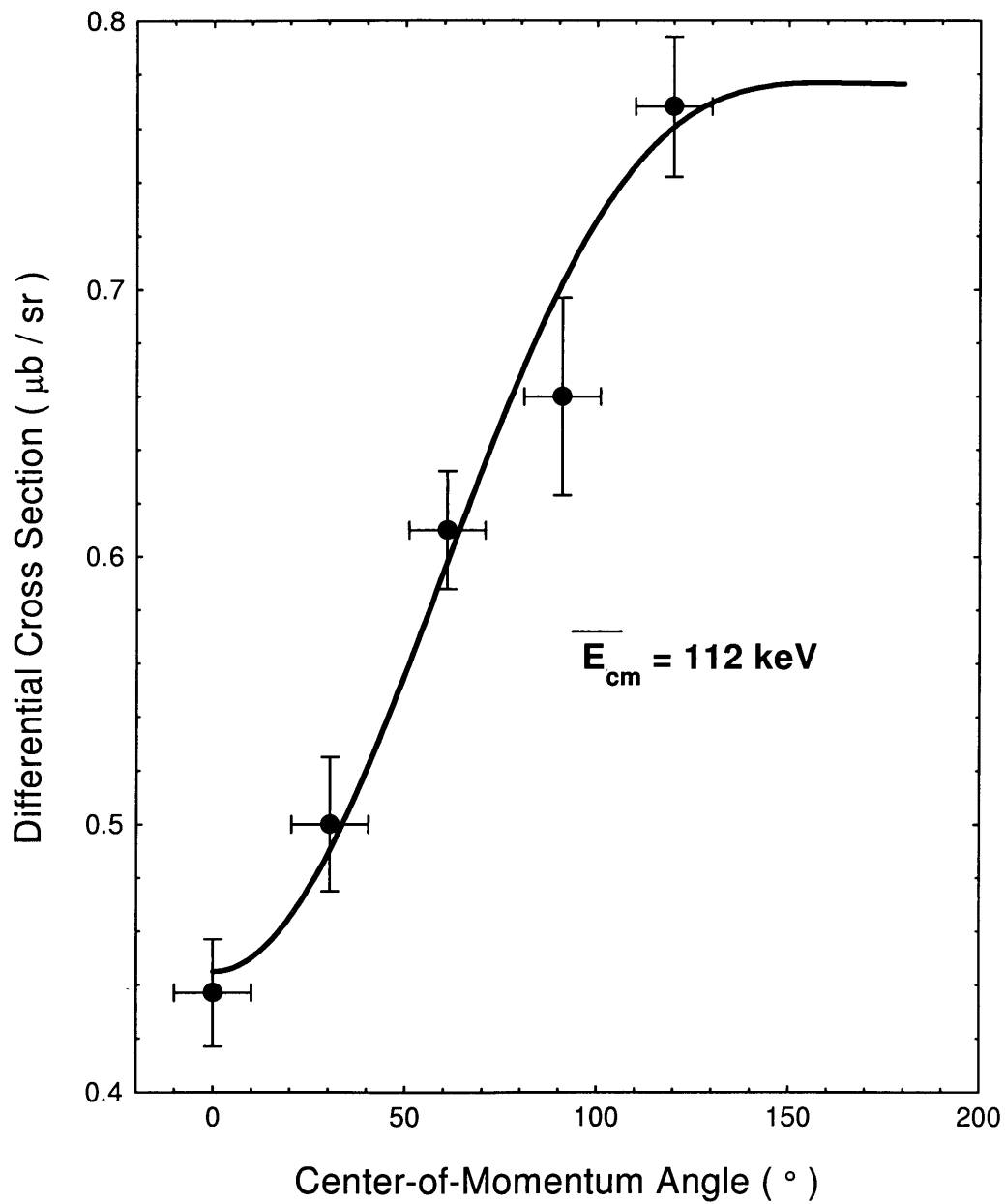


FIG. 6.30. Differential cross section for the $^{11}\text{B}(\text{d},\text{n})^{12}\text{C}$ reaction.

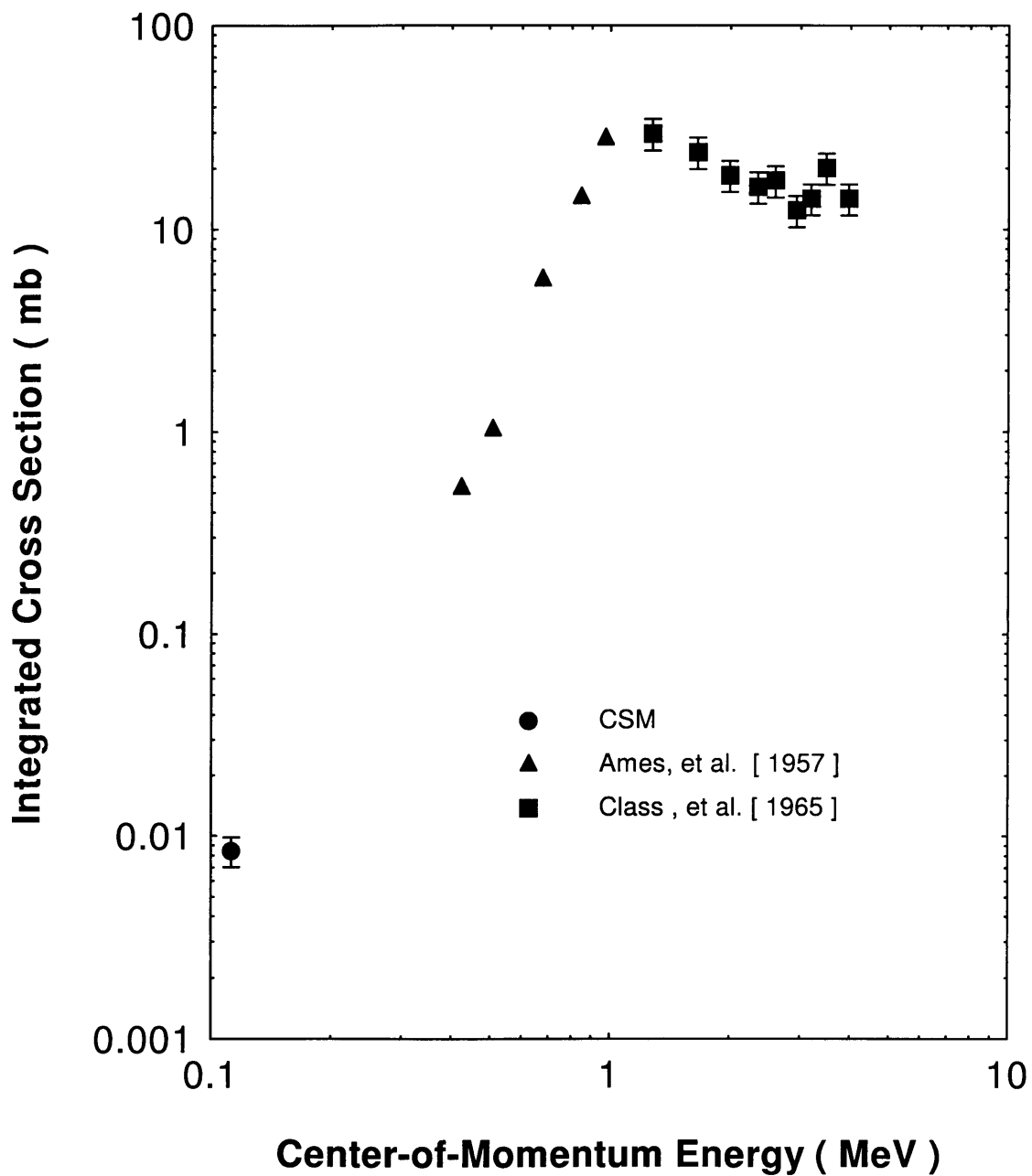


FIG. 6.31. Comparison of integrated cross sections for the $^{11}\text{B}(\text{d},\text{n})^{12}\text{C}$ reaction. Information regarding the data of Ames and of Class can be found in references [16] and [17] respectively.

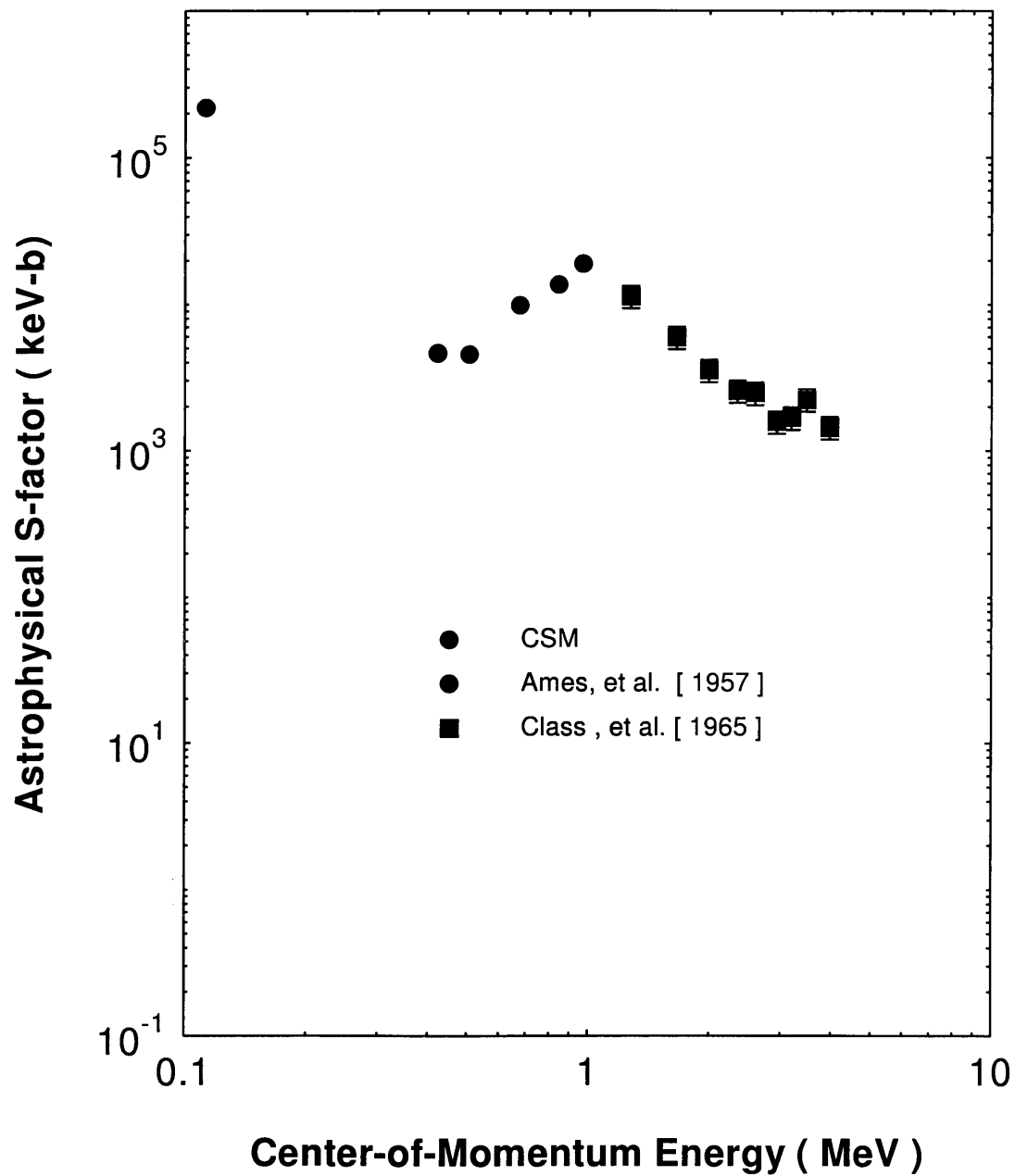


FIG. 6.32. Variation of the astrophysical S-factor with energy for the $^{11}\text{B}(d,n)^{12}\text{C}$ reaction.

spectrum of Figure 6.33. The first excited state of ^{10}B was attained in the reaction $^9\text{Be}(d,n_1)^{10}\text{B}$. That reaction is clearly visible from channels 14 through 20 in Figure 6.33 and extends to higher channels. The $^9\text{Be}(d,n_0)^{10}\text{B}$ reaction also occurs. Neutrons from that reaction extend to higher channels than the first excited state neutrons. This is also clearly visible in Figure 6.33. Finally, a background of counts [possibly due to the $^2\text{H}(d,p)^3\text{H} \rightarrow 2^3\text{H}(d,n)^4\text{He}$ reactions] extended out to even higher channels.

The analysis of the deuteron-induced proton transfer reactions on ^9Be differed from that of the other reactions. The difference arose from the need to separate the neutrons that accompanied the ground and first excited states of the ^{10}B product. Recall that the Kent State code produces the integral efficiencies of the detector. To separate the ^{10}B states, those integral efficiencies must be converted into something equivalent to counts per channel. Consider the definition of the integral efficiency of the Kent State code [page 55] - "Those integral efficiencies represented the percent of neutrons incident on the BC-501A detector that were detected when the counts were summed from the maximum energy channel associated with the incident neutron energy down to the chosen low-end channel." Subtraction of the integral efficiency at a chosen channel, say channel n , from the integral efficiency at one less channel, channel $(n-1)$, produces the percent of the total neutrons that entered the detector and deposited energy at channel $(n-1)$, the differential efficiency. Multiplication of that percentage by the total number of neutrons entering the detector gives the number of neutrons at channel $(n-1)$. Performing the preceding operations for every channel produces the equivalent to the measured counts per channel. In this research, the detected counts per channel were known. To determine the total number of neutrons entering the detector, the counts at each channel were divided by the differential efficiency at each channel.

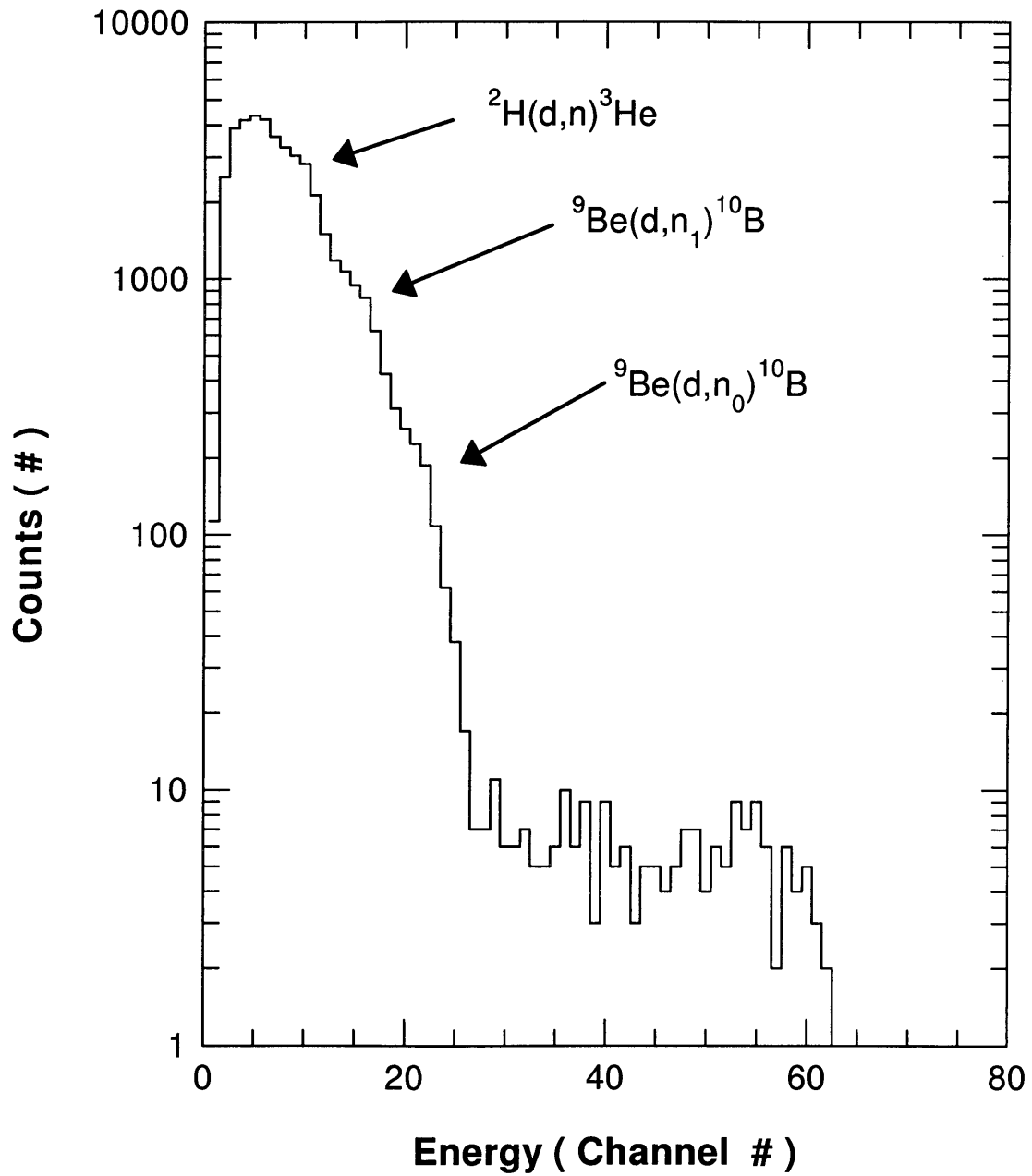


FIG. 6.33. Typical neutron spectrum for the deuteron-induced proton transfer reactions on ${}^9\text{Be}$. Note the existence of the ${}^{10}\text{B}$ ground and 1st excited states.

The analysis was complicated by the overlap between the ground and first excited states. The differential curves for these states were determined from the integral efficiency curves. After subtraction of the background contribution, the total neutron counts for the ground state were calculated for channels where only the ground state contributed. The average of the total neutron counts over those channels was chosen as the true neutron counts for the ground state. The average of the differences between the extrema within the sampled channels and the true counts was chosen as the error.

For example, consider the ${}^9\text{Be}(d,n_0){}^{10}\text{B}$ reaction at a laboratory deuteron energy of 145 keV [effective center-of-momentum energy of 109 keV] and angle of 0° . The best fit to the background was the constant value of 6 counts. Channels 24 to 27 were above the first excited state contributions. The excellent agreement over those channels between the differential efficiency curve and the neutron spectrum is evident in Figure 6.34. [The differential efficiency curve was scaled to match the neutron spectrum in that figure.] The true neutron counts obtained over channels 24 to 27 was (518 ± 29.4) . Neutrons from the ground state contributed to the measured neutron counts over the channels of the first excited state. The counts at each channel due to the ground state were calculated by multiplying the calculated true counts for the ground state by the ground state differential efficiency at each channel. These counts were subtracted from each channel. The remaining counts were attributed to the first excited state. [See Figure 6.34]. The same procedure used to calculate the true number of ground state neutrons was applied to the first excited state. Returning to the example, channels 14 to 17 were higher than the channels from the ${}^2\text{H}(d,n){}^3\text{He}$ reaction. The true neutron counts obtained over these channels was (1719 ± 93) . These counts were then normalized by the 95.5 msr solid angle for comparison with the charged particle results.

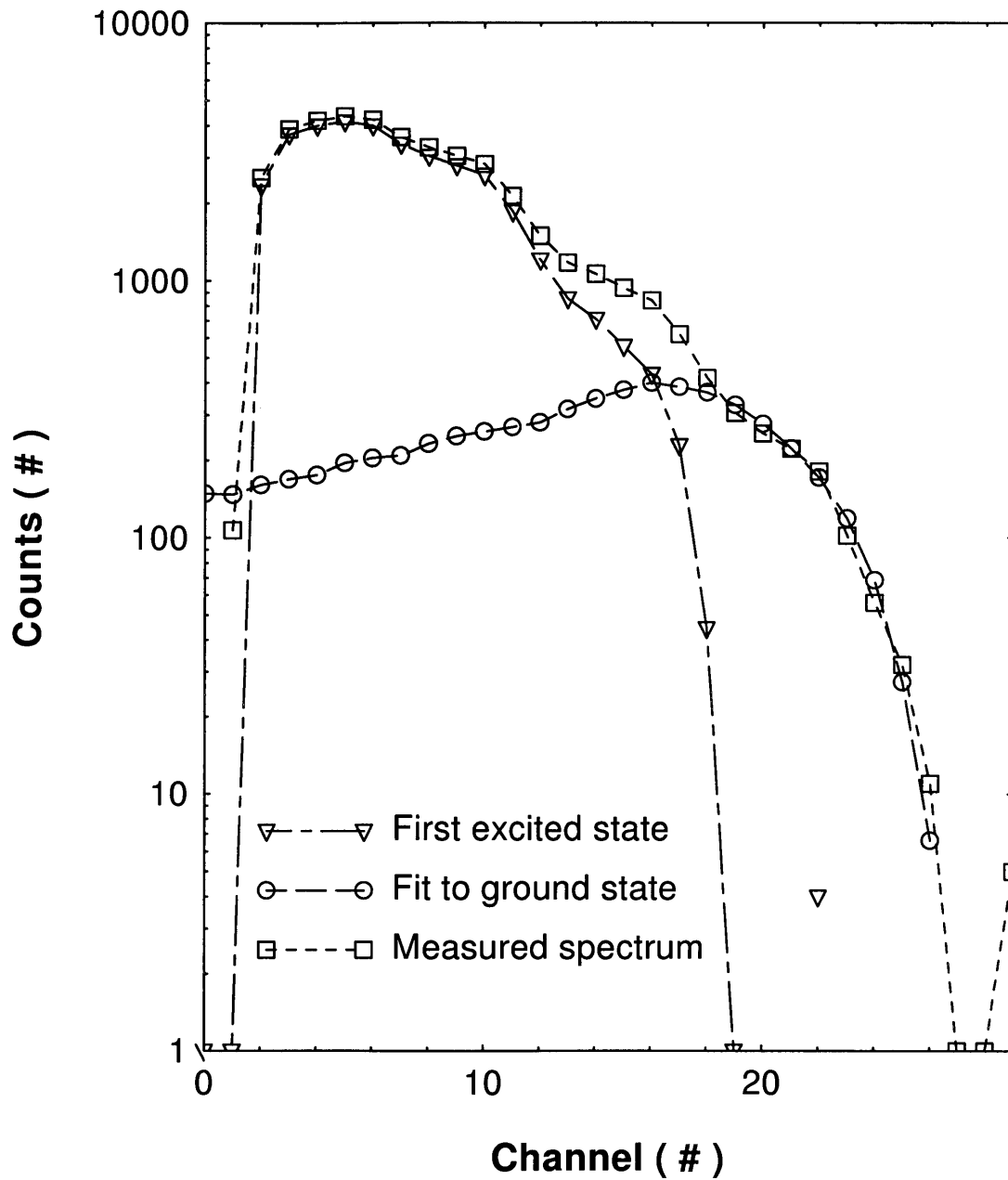


FIG. 6.34. Comparison of differential efficiency curve predicted by Kent State code to the measured spectrum for deuteron-induced proton transfer reactions on ${}^9\text{Be}$. The first excited state shown in the graph is calculated by subtracting the differential curve of the Kent State code from the measured spectrum.

Figure 6.35 shows the particle spectrum collected by the SSB detector. The ${}^9\text{Be}(d,p_0){}^{10}\text{B}$ peak sits on top of an α -particle continuum. The α -particle continuum counts were modeled as a constant over the channels. Subtraction of the linear fit from the total counts yielded the correct counts for the ${}^9\text{Be}(d,p_0){}^{10}\text{Be}$ reaction.

Recall the example at the deuteron laboratory energy of 145 keV [effective center-of-momentum energy of 109 keV] and at an angle of 0° . The SSB detector subtended a solid angle of 51.6 msr. The ${}^9\text{Be}(d,p_0){}^{10}\text{Be}$ peak spanned channels 151 to 177. The calculated α -particle continuum contributed 138 counts to the total of 685 counts over the ${}^9\text{Be}(d,p_0){}^{10}\text{Be}$ channels. Normalizing for the solid angle of 51.6 msr yielded a true count of (10.1 ± 0.5) counts/msr.

Application of equation 5.25 to the current example gives an absolute differential cross section of (1.27 ± 0.072) $\mu\text{b}/\text{sr}$ for the ground state as shown in the following calculation.

$$\begin{aligned} \sigma(\bar{E}_{\text{cm}} = 109 \text{ keV}, \theta_{\text{n,CM}} = 0^\circ) &= \left[\frac{(5.42 \pm 0.31) \text{ counts/msr}}{10.1 \pm 0.5 \text{ counts/msr}} \right] (2.36 \mu\text{b}/\text{sr}) \\ &= (1.266 \pm 0.096) \text{ mb}/\text{sr} \\ &\approx (1.27 \pm 0.10) \mu\text{b}/\text{sr} \end{aligned}$$

Table 6.6 lists the measured absolute differential cross sections for both the ground and first excited states. The errors in the table are purely statistical and do not include the 4.10% systematic error from the calculation of the ${}^9\text{Be}(d,p_0){}^{10}\text{B}$ cross section.

The differential data were fit with curves of the form

$$\sigma(\bar{E}_C M, \theta_{CM}) = a + b \cos(\theta_{CM})$$

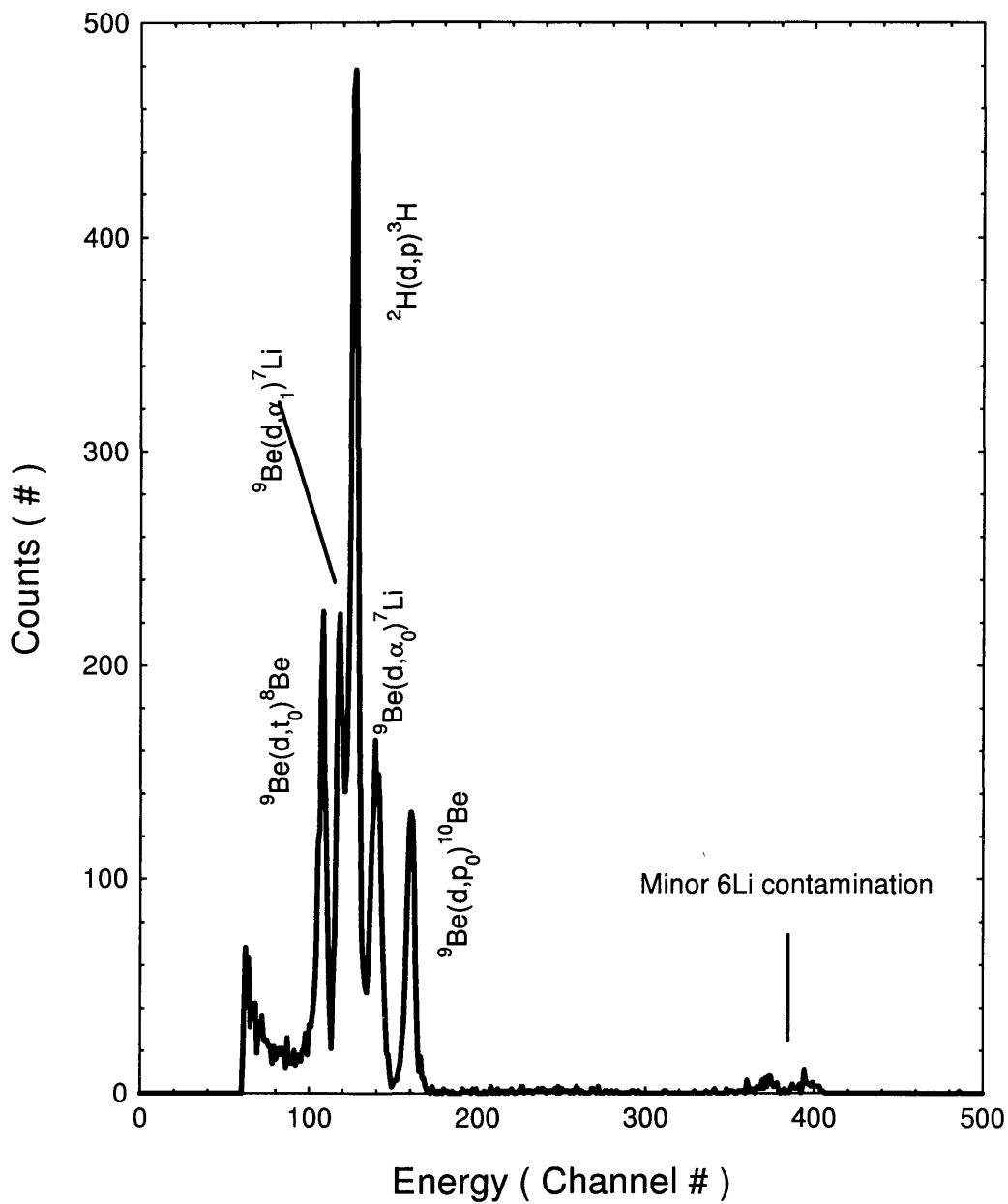


FIG. 6.35. Typical charged particle spectrum for the deuteron-induced reactions on ${}^9\text{Be}$.

Table 6.6. Experimental differential cross sections for the deuteron-induced proton transfer reactions on ${}^9\text{Be}$.

Center-of-Momentum Effective Energy (keV)	final state of 10B	Center-of-Momentum Angle (degrees)	Differential Cross Section ($\mu\text{b} / \text{sr}$)
109	ground	0	1.27 ± 0.072
		30.6	2.19 ± 0.095
		61.1	3.23 ± 0.237
		91.2	2.36 ± 0.213
	1st	0	4.21 ± 0.228
		30.6	4.81 ± 0.261
		61.1	5.25 ± 0.237
		91.2	8.33 ± 0.381

and statistical errors were determined with the same variational method as used for the ${}^2\text{H}(\text{d},\text{n}){}^3\text{He}$ reactions. The minimum and maximum values obtained with this method overestimated the effects of individual errors on the differential coefficients. Averaging a sample of the variations in the curve fit coefficients over combinations of the errors in the data reduced the overestimate in the errors. The resulting differential cross section coefficients are given in Table 6.7. The values of and curve fit to the differential cross section data are shown in Figure 6.36. The differential cross sections were integrated over solid angle to obtain the absolute integral cross sections. The sample of differential curves used to determine the errors in the differential cross sections were integrated. The averages of the minimum and maximum variance in the resulting values were designated the statistical error in the absolute cross section. The results for the integrated cross sections are listed in Table 6.8. Figure 6.37 compares the values from the current work with published cross sections of others. The calculated S-factors for this and the other research are shown in Figure 6.38.

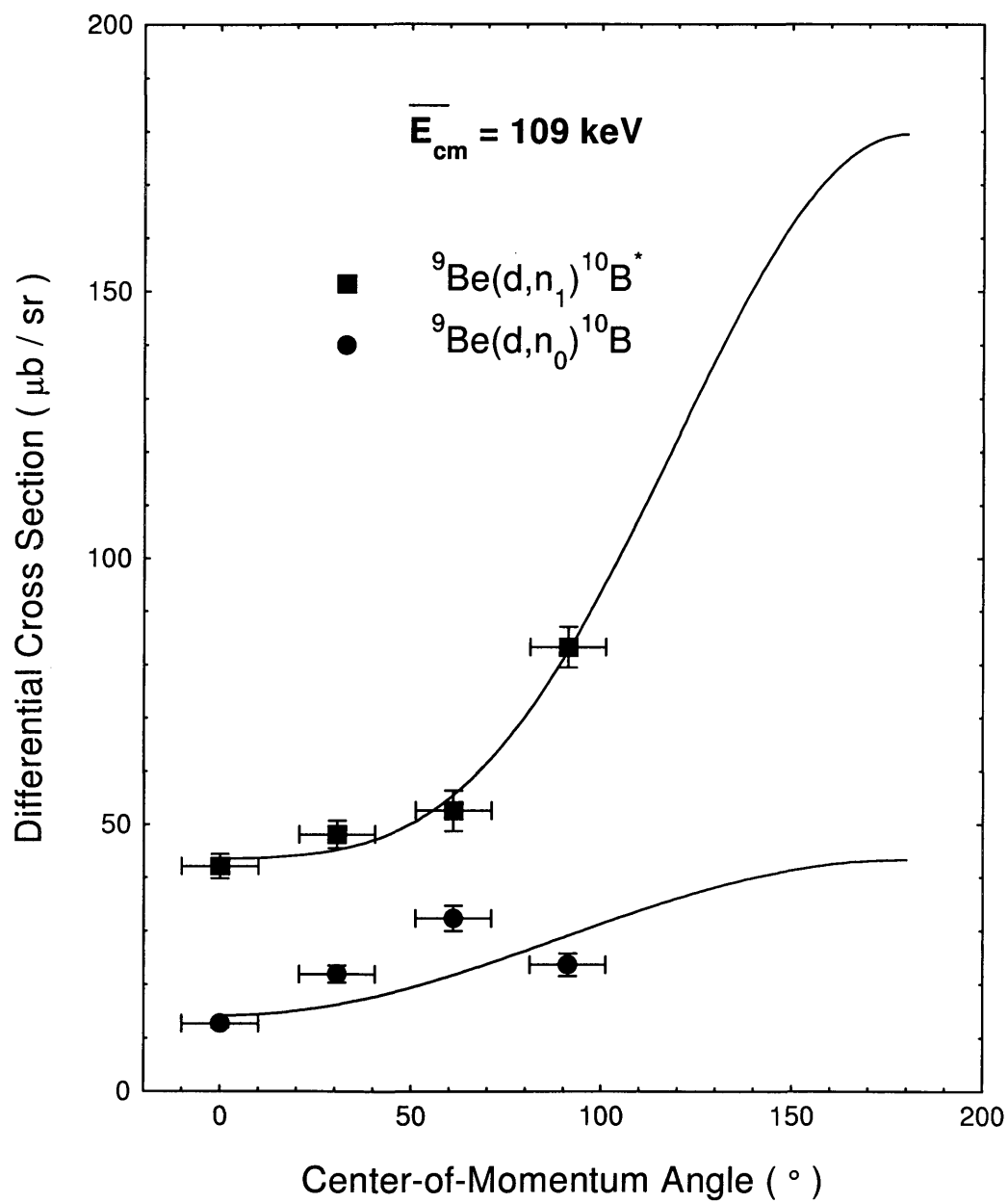


FIG. 6.36. Differential cross section for the ${}^9\text{Be}(d,n){}^{10}\text{B}$ reaction.

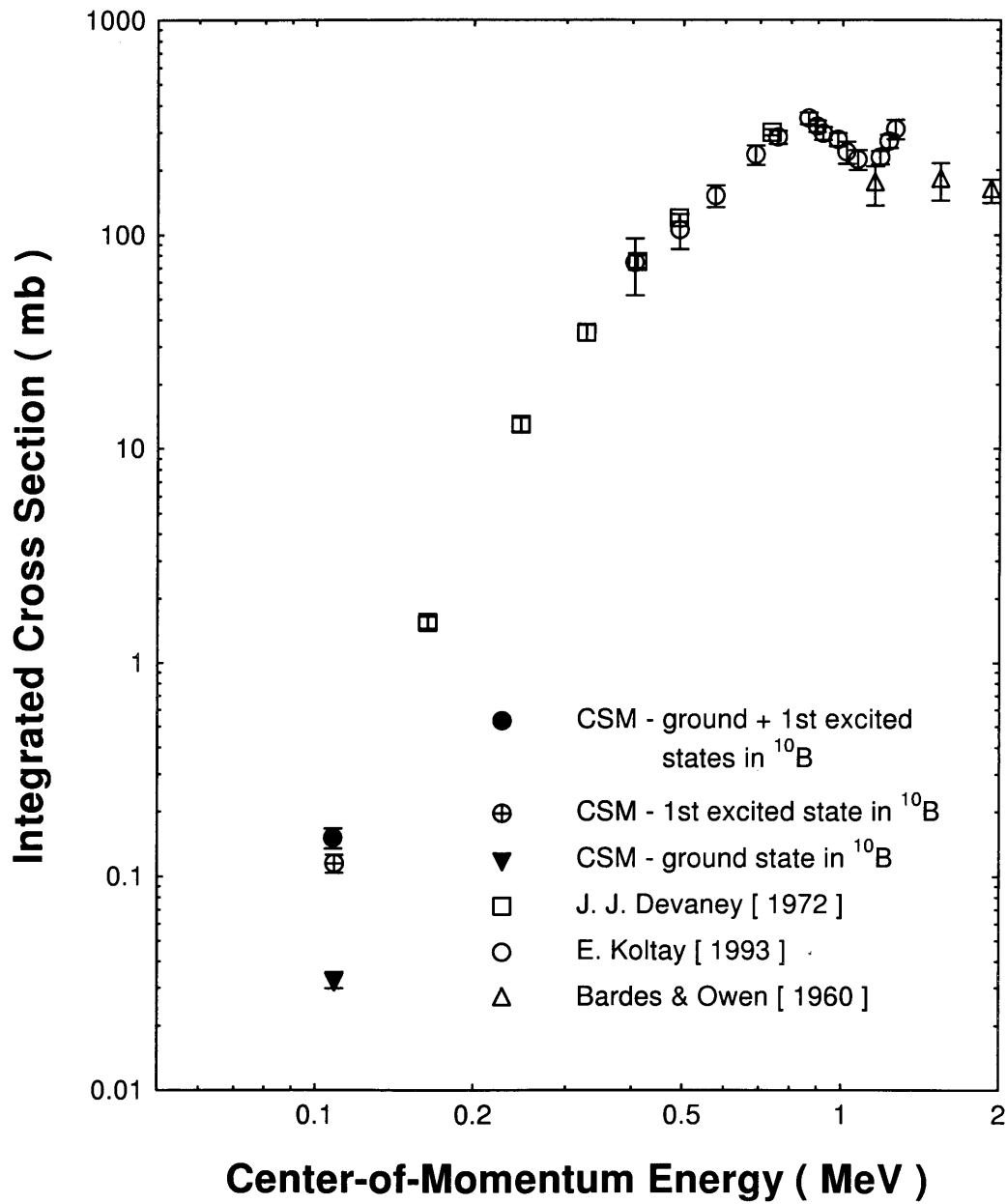


FIG. 6.37. Comparison of integrated cross sections for the deuteron-induced proton transfer reactions on ^9Be . Information regarding the data of Devaney and of Koltay and of Bardes & Owen can be found in references [18] and [19].

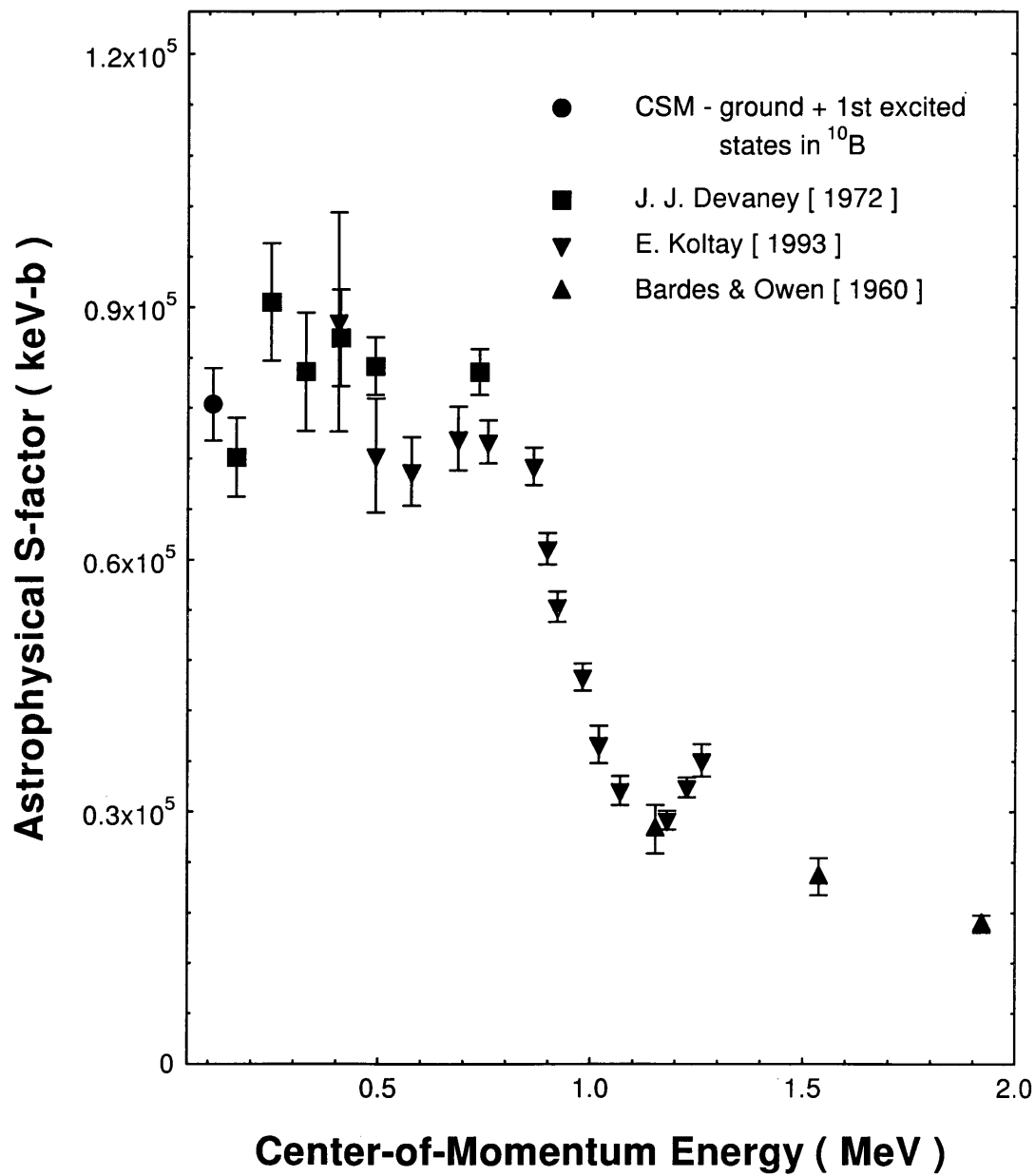


FIG. 6.38. Variation of the astrophysical S-factor with energy for the deuteron-induced proton transfer reactions on ^9Be .

Table 6.7. Differential cross section coefficients in the center-of-momentum reference frame for the deuteron-induced proton transfer reactions

Reaction	\bar{E}_{CM} (keV)	Coefficients ($\mu\text{b}/\text{sr}$)		
		Constant	$\cos(\theta_{CM})$	$\cos^2(\theta_{CM})$
${}^2\text{H}(d, n){}^3\text{He}$	24	288 ± 13	————	203 ± 38
	40	700 ± 41	————	489 ± 113
${}^6\text{Li}(d, n){}^7\text{Be}$	94.3	254 ± 8	————	————
${}^7\text{Li}(d, n){}^8\text{Be}$	50.0	9.92 ± 0.68	7.50 ± 0.74	————
	83.5	157 ± 10	-91.6 ± 12.1	32.9 ± 9.3
	100	383 ± 17	26.3 ± 3.8	-191 ± 23
${}^9\text{Be}(d, n_0){}^{10}\text{B}^{gs}$	109	2.87 ± 0.38	-1.46 ± 0.35	————
${}^9\text{Be}(d, n_1){}^{10}\text{B}^*$	109	8.12 ± 0.37	-6.8 ± 0.78	3.03 ± 0.73
${}^{10}\text{B}(d, n){}^{11}\text{C}$	111	0.233 ± 0.009	-0.0265 ± 0.0040	-0.0393 ± 0.0098
${}^{11}\text{B}(d, n){}^{12}\text{C}$	112	0.700 ± 0.046	-0.166 ± 0.035	$-0.0891 \pm .0190$

Table 6.8. Integrated cross sections and astrophysical S-factors for the deuteron-induced proton transfer reactions. The relative errors apply to the cross sections and the S-factors.

Reaction	Center of momentum effective energy (keV)	Integrated cross section (mb)	Astrophysical S-factor (MeV - b)	Statistical error (±%)	Systematic error (±%)
${}^2\text{H}(d,n){}^3\text{He}$	24	4.47	0.0651	5.37	2.00
	40	10.8	0.0619	4.63	2.00
${}^6\text{Li}(d,n){}^7\text{Be}$	96.6	3.17	42.7	3.17	7.50
${}^7\text{Li}(d,n){}^8\text{Be}$ $\rightarrow 2\alpha$	50.0	0.125	101	5.16	7.50
	83.5	2.11	65.3	6.53	7.50
	100	4.01	49.9	4.99	7.50
${}^9\text{Be}(d,n_0){}^{10}\text{B}$	109	0.0327	18.7	7.87	4.10
${}^9\text{Be}(d,n_1){}^{10}\text{B}^*$	109	0.115	59.7	8.70	4.10
${}^{10}\text{B}(d,n){}^{11}\text{C}$	111	$2.76 \cdot 10^{-3}$	70.9	4.35	6.90
${}^{11}\text{B}(d,n){}^{12}\text{C}$	112	$8.41 \cdot 10^{-3}$	217	4.75	6.90

Chapter 7

APPLICATIONS

7.1 Reaction Rates

Power generation in stars and fusion reactors depends on the reaction rates among the various particle species in these environments. The reaction rates depend on the number densities of the species and on the cross sections for the possible reactions among the species. For a given temperature, T , and particle species, a fraction of the particles, $\varphi(v) = n_v/n$, have velocities between v and $v + dv$ as described by the Maxwell-Boltzmann velocity distribution [46]:

$$\varphi(v) = 4\pi \left(\frac{m}{2\pi kT} \right)^{3/2} v^2 \exp\left(-\frac{mv^2}{2kT}\right). \quad (7.1)$$

The velocity distributions of the “projectiles” and of the “targets” are independent of one another. The probability for two independent distributions to occur within given intervals simultaneously is just the product of the independent probability distributions for those given intervals. The probability distribution for projectiles to have velocities between v_p and $v_p + dv_p$ and targets to have velocities between v_t and $v_t + dv_p$ is thus given by [37]:

$$\begin{aligned} \varphi(v_p, v_t) &= \varphi(v_p) \varphi(v_t) \\ &= 16\pi^2 v_p^2 v_t^2 \left[\frac{(m_p m_t)}{2\pi kT} \right]^3 \exp\left(-\frac{m_p v_p^2 + m_t v_t^2}{2kT}\right). \end{aligned} \quad (7.2)$$

The reaction rate per particle pair is defined as

$$\langle \sigma \nu \rangle = \int_0^\infty \int_0^\infty dv_p dv_t \nu \sigma(\nu) \varphi(v_p, v_t). \quad (7.3)$$

The center-of-momentum and relative velocities are functions of the projectile and target velocities - $\nu = \nu(v_p, v_t)$ and $V = V(v_p, v_t)$. The theory of Jacobian determinants describes the transformation from one set of differential variable to a second set that are functions of the first set. The magnitude of the determinant is the ratio of the differentials. For example :

$$\begin{aligned} \frac{dv_{p,x} dv_{t,x}}{dV_x d\nu_x} &= \begin{vmatrix} \frac{\partial v_{p,x}}{\partial V_x} & \frac{\partial v_{p,x}}{\partial \nu_x} \\ \frac{\partial v_{t,x}}{\partial V_x} & \frac{\partial v_{t,x}}{\partial \nu_x} \end{vmatrix} \\ &= \begin{vmatrix} 1 & \frac{m_t}{m_p+m_t} \\ 1 & \frac{m_p}{m_p+m_t} \end{vmatrix} \\ &= -1 \end{aligned} \quad (7.4)$$

therefore, $dV_x d\nu_x = |-1| dv_{p,x} dv_{t,x}$. These results also apply to the y and z components; thus, $d^3V d^3\nu = |-1| d^3v_p d^3v_t$. The reaction rate per particle pair transforms into center-of-momentum and relative velocities coordinates as [47] :

$$\begin{aligned} \langle \sigma \nu \rangle &= \int_0^\infty \int_0^\infty d^3v d^3V \nu \sigma(\nu) \left(\frac{m_p + m_t}{2\pi kT} \right)^{3/2} \exp \left[- \left(\frac{m_p + m_t}{2kT} \right) V^2 \right] \left(\frac{\mu}{2\pi kT} \right)^{3/2} \\ &\quad \times \exp \left[- \frac{\mu \nu^2}{2kT} \right] \\ &= \int_0^\infty d\vec{V} \varphi(\vec{V}) \int_0^\infty d\nu \nu \sigma(\nu) \left(\frac{\mu}{2\pi kT} \right)^{3/2} \exp \left[- \frac{\mu \nu^2}{2kT} \right]. \end{aligned} \quad (7.5)$$

Maxwell-Boltzmann distributions normalize to unity; therefore, the integral over \vec{V} equals one. Applying nonrelativistic kinematics and equation 5.19 to equation 7.5,

assuming a constant S-factor, and simplifying yields

$$\begin{aligned}\langle\sigma\nu\rangle &= \left(\frac{8}{\pi\mu}\right)^{1/2} (kT)^{-3/2} \int_0^\infty dE_{CM} \sigma(E_{CM}) E_{CM} \exp\left[-\frac{E_{CM}}{kT}\right] \\ &= \left(\frac{8}{\pi\mu}\right)^{1/2} (kT)^{-3/2} S_0 \int_0^\infty dE_{CM} \exp\left[-\frac{E_{CM}}{kT} - \sqrt{\frac{E_G}{E_{CM}}}\right]\end{aligned}\quad (7.6)$$

As shown in equation 7.6, two factors determine the reaction rate per particle pair. The Maxwell-Boltzmann distribution peaks at low energy. The quantum mechanical probability for penetrating the Coulomb barrier increases with increasing energy. These competing terms in the integrand in equation 7.6 produce a peak known as the Gamow peak, with a maximum value at energy E_0 and a width of Δ [7].

$$\begin{aligned}E_0 &= 1.22 \left(Z_p^2 Z_t^2 \mu T_6^2\right)^{1/3} \text{ (keV)} \\ \Delta &= 0.749 \left(Z_p^2 Z_t^2 \mu T_6^5\right)^{1/6} \text{ (keV)}\end{aligned}\quad (7.7)$$

where temperature is designated by $T_n = T/10^n$ in Kelvin. The energy windows of the Gamow peaks for environments of the Big Bang nucleosynthesis ($T_9 \sim 0.60$), tokamaks ($T_9 = 0.12$), and massive stars (interiors at $T_6 \sim 60$) are given in Table 1.1. The energies of this research are within these energy windows, demonstrating the relevance of the measurements.

Assuming that only contributions from the energy window about the Gamow peak are significant and that the S-factor is constant within the energy window, the reaction rate per particle pair can be simplified to [52]:

$$\langle\sigma\nu\rangle = \left(\frac{2}{\mu}\right)^{1/2} \frac{\Delta}{(kT)^{3/2}} S(E_0) \exp(-3E_0/kT).$$

The power generated due to a reaction can be calculated from the reaction rate

per particle pair, the number densities of the projectile and of the target, and the active volume, V , over which the reactions occur [53]:

$$P = \frac{n_p n_t}{(1 + \delta_{p,t})} \langle \sigma v \rangle V.$$

Reaction network codes predict relative elemental abundances and net power generation in stars and other environments [21]. The codes require information on the rate of creation and of destruction of the nuclei to determine the time evolution of the abundances. The various reactions are linked together in a network where elements created in one reaction are destroyed in others. [See Figure 7.1.] As shown in equation 7.5, a reaction rate depends on the cross section for that reaction.

7.2 Fusion Diagnostics

7.2.1 Background

Fusion reactors heat a fuel into the plasma state, confine that plasma, and extract the energy produced by the nuclear reactions within the plasma. The charged particles in the plasma collide which result in accelerations. The accelerated charged particles produce bremsstrahlung radiation which carries energy from the plasma. The power dissipated by the bremsstrahlung radiation, P_{br} , depends on the square of the charge [Z] of the ion in the collision and on the number densities of the ion and of the electrons [n and n_e respectively] [4, 54].

$$P_{br} \approx 0.5 \times 10^{-36} Z^2 n n_e (kT)^{1/2}. \quad (7.8)$$

Fusion reactors must operate at high enough temperatures so that the power from the fusion reactions is greater than these bremsstrahlung losses. Some current fu-

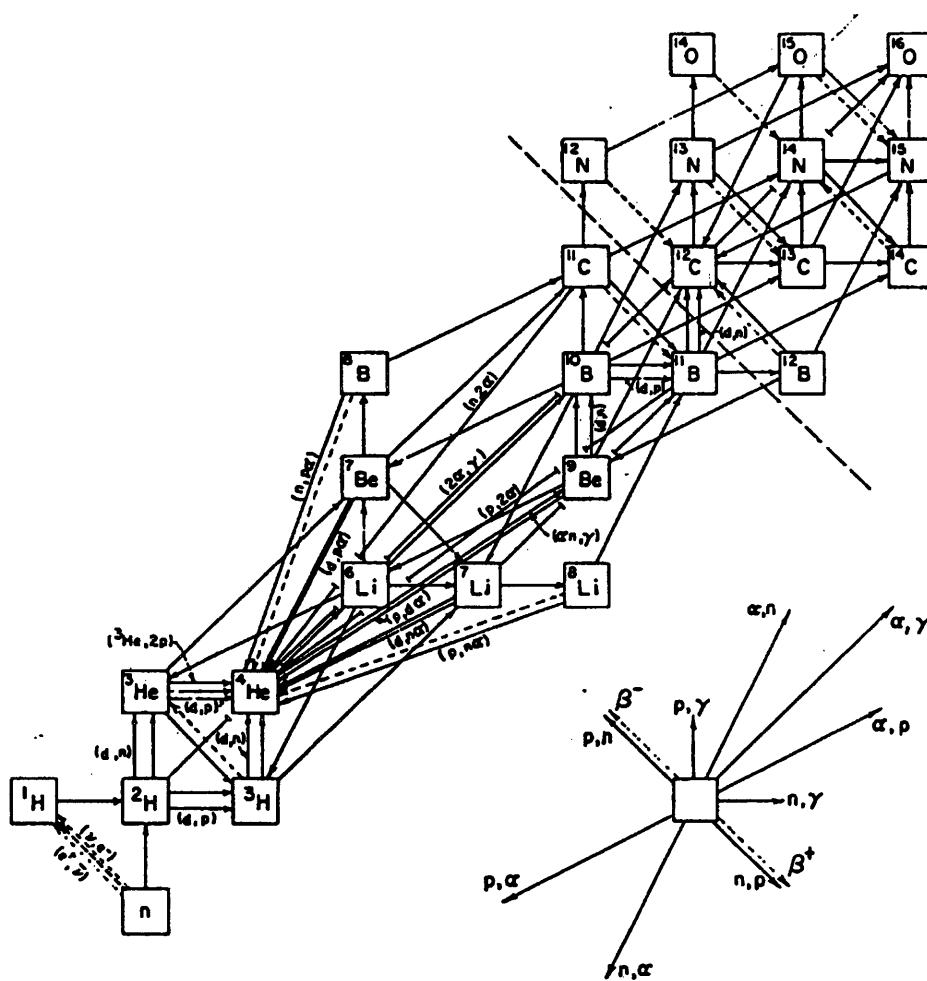


FIG. 7.1. Nuclear reaction network.

sion reactors are lined with beryllium or boron. The bremsstrahlung losses due to contamination of the plasma from these linings may be enough to quench the fusion reactors. [See Figure 7.2.]

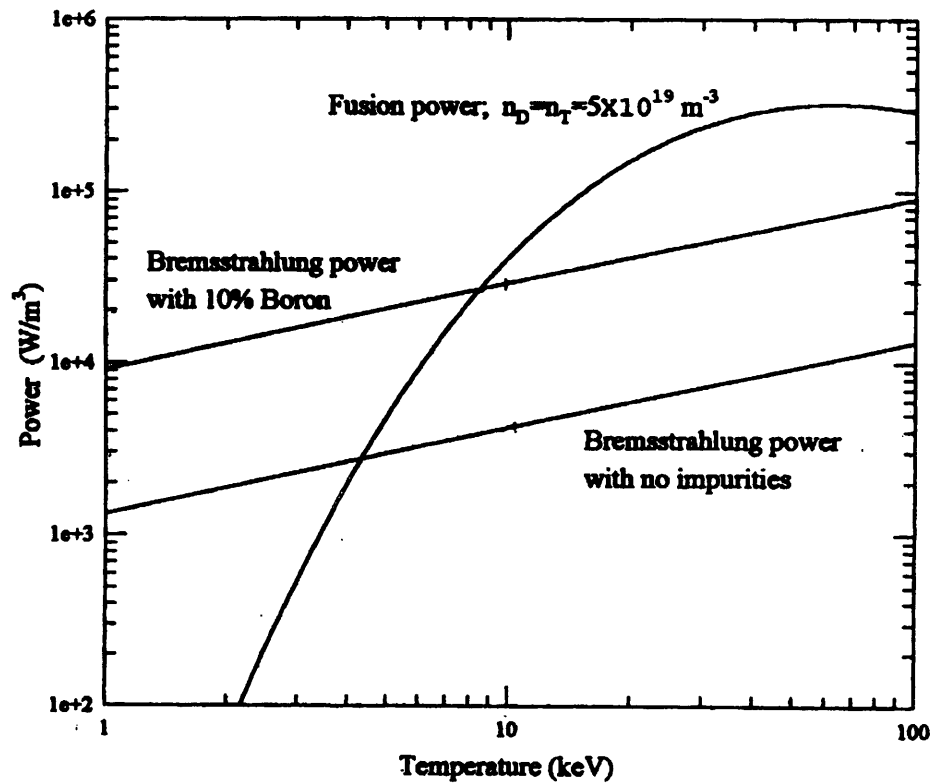


FIG. 7.2. Effect of contamination on the Bremsstrahlung radiation losses in a typical tokamak plasma [reproduced from [7]].

7.2.2 Monitoring plasma contamination

Plasma contamination can be monitored by the γ -transitions of product nuclei [7]. The technique can only monitor reactions that place the product nucleus in an excited state. The measured γ -transition rate, $R_m(\gamma)$, due to the reactions ${}^9\text{Be}(d, p_1){}^{10}\text{Be}^* \rightarrow \gamma + {}^{10}\text{Be}^{gs}$ and ${}^{10}\text{B}(d, p_2){}^{11}\text{B}^* \rightarrow \gamma + {}^{10}\text{B}^{gs}$ are used to measure

the number density of the contaminants in the plasmas.

$$R_m(\gamma) = n_1 n_2 \langle \sigma \nu \rangle V \eta_\gamma \quad (7.9)$$

Plasma contamination can also be monitored directly by the (d,n) reactions on contaminants. The cross sections for the ${}^9\text{Be}(d, n){}^{10}\text{B}$ and for the ${}^{10,11}\text{B}(d, n){}^{11,12}\text{C}$ reactions have been measured. These cross sections are larger than the analog (d,p) reactions. The efficiency of a 2" x 2" cylindrical BC-501A detector was calculated with the Kent State University Neutron Detection Efficiency code. At energies corresponding to the 4.27 MeV neutron from the ${}^9\text{Be}(d, n){}^{10}\text{B}$ reaction, the calculated efficiency was approximately 0.5%. A typical cylindrical sodium iodide (NaI) detector of comparable size has a γ -efficiency of 0.1% to 0.2% [4]. Both of the stated efficiencies measure the percentage of particles (neutrons or gammas) that are detected from a given flux of particles into the detector. The higher efficiency and larger cross section of the (d,n) reactions permit detection of contaminants at lower number densities than possible with the γ -transition technique.

The large ${}^2\text{H}(d, n){}^3\text{He}$ cross section also presents the opportunity to monitor the concentrations of deuterium in the plasma. Equation 7.9 must be modified to avoid double counting of the deuterium nuclei. The generalized equation is

$$R_m(\gamma) = \frac{n_1 n_2}{(1 + \delta_{1,2})} \langle \sigma \nu \rangle V \eta_\gamma \quad (7.10)$$

Chapter 8

SUMMARY AND CONCLUSIONS

8.1 Summary

This research began as a complement to the earlier work by Yan, et al. [7, 20] on the analog (d,p) reactions. These reactions are important for a complete understanding of big bang nucleosynthesis. Knowledge of the reactions responsible for the creation and destruction of ${}^7\text{Li}$ and ${}^9\text{Be}$ will help determine which of the competing big bang models, homogeneous or inhomogeneous, is correct [22]. The cross sections for those reactions are one input into models of the reaction chains that determine the primordial abundances of the nuclei. These predictions are compared with observed abundances reported by astronomers.

Current tokamak fusion test reactors are lined with beryllium or with boron. Plasma collisions with the walls of the tokamaks and heat from the plasma release these elements from the wall into the plasma. Since the power radiated by charged particles goes as the square of the charge of the particle, the losses due to the beryllium or boron contaminations is important. The levels of contamination can be monitored by measuring the neutrons from the ${}^9\text{Be}(d,n){}^{10}\text{B}$ or ${}^{10,11}\text{B}(d,n){}^{11,12}\text{C}$ reactions and knowing the cross sections. [See Section 7.2.]

In this research, I improved cross section measurements over past investigations by others of the deuteron-induced proton transfer reactions on the same light nuclei. For the reaction on ${}^6\text{Li}$, the error in the cross section was reduced from $\pm 15\%$ to $\pm 8\%$. For the reactions on ${}^7\text{Li}$, ${}^9\text{Be}$, and ${}^{10,11}\text{B}$, the cross sections were determined

for the first time at these low energies.

The optimization of the combined detector and electronics produced a pulse shape discriminator capable of separating neutrons from the large background of gamma photons. Measurement of the different decay times in the intensity of the light produced in the BC-501A liquid scintillator by the neutrons and by the photons form the basis for the separation. The total light produced by a particle is directly related to the energy deposited by the particle in the detector. Plotting energy versus decay time improves the separation of the neutrons and gamma photons. Different (d,n) reactions are distinguished based on the energy projected neutron spectra. The energy transfer mechanisms between the neutrons and the BC-501A produces a continuum of energies in the projected neutron spectrum for each reaction. The overlap of these continua necessitated the use of a Monte Carlo simulation to extract the true neutron counts for a given reaction. The Kent State Neutron Detection Efficiency code was chosen for the task.

The method of relative cross sections uses the known absolute cross section of one reaction and the true counts from that reaction and a second reaction to determine the absolute cross section of the second reaction. [See Section 5.3] A silicon surface barrier (SSB) detector, fixed at a laboratory angle of 90° , provided the reference spectra of deuteron-induced charged-particle-as-product reactions. Absolute cross sections for these reference reactions have been determined by other researchers. Those cross sections and the relative results of this research were used to determine the absolute cross sections for the (d,n) reactions.

The cross section varies greatly with energy. Removing the effects of the Coulomb barrier penetration and of the wave nature of matter leaves a slowly varying function of energy, the astrophysical S-factor. [See Section 5.3] The S-factor accounts for the

nuclear effects and, through the relation to the cross section, is an input parameter to reaction rate codes. Those codes are used to predict the time evolution of the abundances of the nuclei.

8.2 Conclusions

The relative cross section method is valid for targets of sufficient thickness to stop all projectiles [deuterons] inside the targets. Effective thin-target energies for each thick-target reaction-energy pair were calculated assuming a constant S-factor for each reaction. Although an approximation, the constant S-factor assumption gave effective energies for which the ${}^2\text{H}(d,n){}^3\text{He}$ cross sections agreed with published values. [See Figures 6.5 and 6.6.] The agreement also validates the use of the Kent State University Neutron Detection Efficiency code.

Elwyn, et al. [9] determined the ${}^6\text{Li}(d,p_0){}^7\text{Li}$ and ${}^6\text{Li}(d,p_0){}^7\text{Li}^*$ cross sections to laboratory effective energies of 118 keV. Those cross sections were used to determine the ${}^6\text{Li}(d,n){}^7\text{Be}$ cross section at a laboratory effective energy of 126 keV [center-of-momentum effective energy of 94.4 keV]. Hirst, et al. measured the ${}^6\text{Li}(d,n){}^7\text{Be}$ integrated cross section to laboratory effective energies as low as 115 keV with reported total errors of $\pm 15\%$. The total error in the integrated cross section from this research is $\pm 8.14\%$. The fit to the measurements of Hirst do agree with the results of this research to within the overlapping errors; therefore, I believe the values published by Hirst, et al. to within the reported $\pm 15\%$ error.

The naturally occurring lithium in the targets used for the ${}^7\text{Li}(d,n){}^8\text{Be} \rightarrow 2\alpha$ research contained 7.5% ${}^6\text{Li}$. The ${}^6\text{Li}(d,p_0+p_1){}^7\text{Li}$ double peak appeared in the charged particle spectra. The cross sections for that reaction were calculated from the data published by Elwyn, et al. [9] and was used to determine the ${}^7\text{Li}(d,n){}^8\text{Be} \rightarrow 2\alpha$ cross

sections. Comparison of those cross sections with values obtained from a secondary source on a 1957 Los Alamos report indicate that the Los Alamos values are low. [See Figures 6.18 and 6.19.] The lack of access to the original report made direct comparison of the measurements and experimental methods impossible, thus no reason can be ascertained for the difference. In addition, that Los Alamos data did not extend to as low an energy as the current research; therefore, direct comparison would only have been possible for a portion of the current data set.

The $^{10}\text{B}(\text{d},\text{n})^{11}\text{C}$ research produced an interesting result. The absolute differential cross sections for this reaction were determined using the known cross section of the $^{10}\text{B}(\text{d},\alpha_0)^8\text{Be}$ reaction formerly measured by Yan, et al. of the Colorado School of Mines [7]. This reaction was easily measured in the charged particle spectra. The S-factor showed a marked drop in value compared to the values at higher energy. [See Figure 6.26.] The apparent drop is due to the nuclear structure of ^{11}C . Resonances in the reaction may occur due to energy levels in the ^{11}C that coincide with the higher energies in the other experiments.

The naturally occurring boron used in the targets for the $^{11}\text{B}(\text{d},\text{n})^{12}\text{C}$ research contained 19.8% ^{10}B . The $^{10}\text{B}(\text{d},\alpha_0)^8\text{Be}$ peak was visible in the charged particle spectra and was used to determine the absolute cross sections for the $^{11}\text{B}(\text{d},\text{n})^{12}\text{C}$ reaction. A broad energy level occurs in ^{12}C just below the $^{11}\text{B}(\text{d},\text{n})^{12}\text{C}$ reaction energy. The high energy tail of this energy level should enhance the reaction cross section over the expected nonresonant value. That enhancement is visible in the integrated cross section when compared to the values at higher energies. [See Figures 6.30 and 6.31.]

The most unexpected result occurred in the measurement of the $^9\text{Be}(\text{d},\text{n})^{10}\text{B}$ reactions. The neutron spectra [see sample spectrum in Figure 6.32] revealed what appeared to be two reactions. Further investigation showed the two reactions to

be the expected final ground state product of ^{10}B and the unexpectedly large first excited state [0.7184 MeV above the ground state in energy] of the product ^{10}B . A widened literature search uncovered a secondary source ([55] regarding thermal neutron analysis) which refers to a Soviet publication that demonstrated the increase in the relative intensity [hence cross section] of the first excited state to that of the ground state with decreasing energy from 1.0 MeV to 0.5 MeV. [Here intensity refers to the number of counts per incident deuteron.] No explanation was given in the secondary source and the original Soviet journal was unavailable. No simple explanation can be determined from the energy level diagram of ^{10}B . An interesting aside is the existence of a resonance in the $^7\text{Li}(\alpha,n)^{10}\text{B}$ reaction at the correct energy for the first excited state in ^{10}B .

8.3 Outlook

This research has produced information useful in various fields from cosmological research to the applied physics of tokamak fusion reactor diagnostics. As with any quality research, this research also points the way to future work. The technique of combining relative cross section measurements with the Kent State Neutron Detection Efficiency code to extract deuteron-induced proton transfer reaction cross sections has been proven for low energies of interest in nucleosynthesis in nature and in future fusion reactors. For a number of the reactions, the energies explored were lower than any previous research. For other reactions, the total error in measured cross sections were reduced. The next step in the progression of research is to conduct these same measurements at numerous, closely spaced energies within this low energy regime for each of the reactions. Those measurements will improve the values for the S-factors and possibly permit functional fits to the S-factors. Functional fits to the S-factors

would then be used to better extrapolate cross sections to still lower energies and also be used in the calculations of the thick-target effective energies. Some of the needed measurements [below 180 keV deuteron energy in laboratory reference frame] can be carried out at the current facility at the Colorado School of Mines. Some of the reactions [such as those on ^9Be and $^{10,11}\text{B}$] have gaps at higher energies that would require collaboration with colleagues at higher energy facilities.

A computer model of deuteron-induced single-nucleon [proton or neutron] transfer reactions is currently under development at the Colorado School of Mines. The experimental cross sections can be used to guide the development of that computer model. The completed model could then be used to predict cross sections not yet determined experimentally.

REFERENCES

- [1] M. Zeilik and S. A. Gregory, *Introductory Astronomy & Astrophysics*, Saunders College Publishing, New York, 4th edition, 1998.
- [2] P. W. Nicholson, *Nuclear Electronics*, John Wiley and Sons, NY, 1974.
- [3] L. C. Woods, *Introduction to Neutron Distribution Theory*, John Wiley and Sons, NY, 1964.
- [4] K. S. Krane, *Introductory Nuclear Physics*, John Wiley and Sons, NY, 1988.
- [5] R. A. Winyard, J. E. Lutken, and G. W. McBeth, *Nuclear Instruments and Methods* **95**, 141 (1971).
- [6] G. F. Knoll, *Radiation Detection and Measurement*, John Wiley and Sons, NY, 2nd edition, 1989.
- [7] J. Yan, *Measurement and Applications of Nuclear Reactions $^7\text{Li}+d$, $^9\text{Be}+d$, $^{10}\text{B}+d$, $^{11}\text{B}+d$ and $^7\text{Li}+^3\text{He}$* , PhD thesis, Colorado School of Mines, Golden, CO, 1995.
- [8] H. Liskeien and A. Paulsen, *Nuclear Data Tables(Nuclear Data Sect. A)* **11**, 569 (1973), Compiled in 1996 by Arzamas for CSISRS.
- [9] A. J. Elwyn et al., *Physical Review C* **16**, 1744 (1977).
- [10] B. Guzhovskij, N. Abromovich, A. Zvenigorodskij, G. Slepcev, and S. Trusillo, *Izv. Rossiiskoi Akademii Nauk, Ser. Fiz.* **44**, 80 (1983), Retrieved from CSISRS.

- [11] L. Q. L. Qichang, W. Zongxi, Z. Naigong, and S. Zongren, *Chin. J. Science and Technique of Atomic Energy* **1** (1977), referenced from CSISRS.
- [12] G. Osetinskij, B. Sikora, J. Tyke, and B. Fryschin, The investigation of ${}^7(\text{d},\text{n})\text{be}-8$ reaction, reference JINR-P15-5143, 4ZZZDUB, 1970, referenced from CSISRS.
- [13] K. Wohlleben and E. Schuster, *Radiochimica Acta* **12** (1969), referenced from CSISRS.
- [14] B. Guzhovskij, S. N. Abromovich, and V. A. Pereshivkin, *Vop. At.Nauki i Tekhn, Ser. Yadernye Konstanty* **55** (1984), referenced from CSISRS.
- [15] W. Anders, P. Herges, and W. Scobel, *Zeitschrift fuer Physik, Section A* **301** (1981), referenced from CSISRS.
- [16] O. Ames, G. Owen, and C. Swartz, *Physical Review* **106** (1957), referenced from CSISRS.
- [17] C.M.Class, J. Price, and J. Risser, *Nuclear Physics* **71** (1965), referenced from CSISRS.
- [18] J. J. Devaney, $\text{Be}9(\text{d},\text{n})\text{b}10$ cross section in the range 0 to 2.8 mev, reference LA4851, Los Alamos, 1972.
- [19] E. Koltay, *Acta Physica Hungarica* **16** (1963), referenced from CSISRS.
- [20] J. Yan, F. E. Cecil, J. A. McNeil, M. Hofstee, and P. D. Kunz, *Physical Review C* **55**, 1890 (1997).
- [21] D. N. Schramm and R. V. Wagoner, *Annual Review of Nuclear Science* **27**, 37 (1977).

- [22] V. Trimble, *The Astronomy and Astrophysics Review* **3**, 1 (1991).
- [23] M. S. Smith, L. H. Kawano, and R. A. Malaney, *The Astrophysical Journal Supplement Series* **85**, 219 (1993).
- [24] J. Szabo, Z. Boedy, S. Szegedi, and M. Varnagy, *Nuclear Physics A* **289** (1977),
Referenced from CSISRS.
- [25] S. G. Buccino and A. B. Smith, *Physics Letters* **19** (1965), referenced from
CSISRS.
- [26] N. Jarmie and R. E. Brown, *Nuclear Instruments and Methods in Physics Research B* **10/11**, 405 (1985).
- [27] R. E. Brown and N. Jarmie, *Physical Review C* **41**, 1391 (1990).
- [28] F. Hirst, I. Johnstone, and M. Poole, *Philosophical Magazine* **45** (1954).
- [29] W. R. Leo, *Techniques for Nuclear and Particle Physics Experiments*, Springer-Verlag, NY, 2nd edition, 1994.
- [30] E. Segre, *Nuclei and Particles, an Introduction to Nuclear and Subnuclear Physics*, Addison-Wesley Publishing Company, Inc., NY, 2nd edition, 1982,
Reprint.
- [31] M. L. Roush, M. A. Wilson, and W. F. Hornyak, *Nuclear Instruments and Methods* **31**, 112 (1964).
- [32] T. K. Alexander and F. S. Goulding, *Nuclear Instruments and Methods* **13**, 244 (1961).

- [33] J. B. Birks, *The Theory and Practice of Scintillation Counting*, Pergamon Press, NY, 1967, reprint.
- [34] W. Scharf, *Particle Accelerators and Their Uses: Part 1*, Harwood Academic Press, NY, 1986, Eugene Lepa, translator.
- [35] B. Sabbah and A. Suhami, *Nuclear Instruments and Methods* **58**, 102 (1968).
- [36] L. J. Heistek and L. van der Zwan, *Nuclear Instruments and Methods* **80**, 213 (1970).
- [37] C. Rolfs and W. S. Rodney, *Cauldrons in the Cosmos*, The University of Chicago Press, Chicago, 1988.
- [38] F. E. Cecil, e-mail, 2000, Confirmation of ion source and accelerator operating parameters.
- [39] K. F. Flynn, L. E. Glendenin, E. P. Steinberg, and P. M. Wright, *Nuclear Instruments and Methods* **27** (1964).
- [40] Bicron, Bc-501a liquid scintillator, Web site, 2000, <http://www.bicron.com/bc501A.htm>.
- [41] N. Nakao et al., *Nuclear Instruments and Methods in Physics Research A* **362**, 454 (1995).
- [42] R. A. Cecil, B. D. Anderson, and R. Madey, *Nuclear Instruments and Methods* **161**, 439 (1979).
- [43] R. A. Cecil, B. D. Anderson, and R. Madey, Kent state university neutron detector efficiency code, electronic, 9, Tranfered via internet to Colorado School of Mines.

- [44] B. D. Anderson, e-mail, 1999, Conversation regarding the Kent State University Neutron Detection Efficiency code.
- [45] C. Rolfs and C. A. Barnes, *Annual Review of Nuclear and Particle Science* **40**, 45 (1990).
- [46] E. E. Anderson, *Modern Physics and Quantum Mechanics*, W. B. Saunders and Co., Philadelphia, 1971.
- [47] D. C. Clayton, *Principles of Stellar Evolution and Nucleosynthesis*, The University of Chicago Press, Chicago, 2nd edition, 1983.
- [48] W. J. Thompson, B. W. Carrey, and e. Hugon J. Karwowski, *Workshop on Primordial Nucleosynthesis*, World Scientific Publishing Co Pte., Ltd., Teaneck, NJ, 1990.
- [49] H. C. Ohanian, *Principles of Quantum Mechanics*, Prentice Hall, Englewood Cliffs, NJ, 1990.
- [50] J. F. Ziegler and J. P. Biersack, Srim-2000.10: The stopping and range of ions in matter, electronic, 1999, IBM - Research, Yorktown, NY.
- [51] L. C. Feldman and S. T. Picraux, *Ion Beam Handbook for Material Analysis*, chapter 4, page 174, Academic Press, Inc., New York, 1977, J. W. Mayer and E. Rimini, editors.
- [52] R. N. Boyd, C. A. Mitchell, and B. S. Meyer, *Physical Revue C* **47**, 2369 (93).
- [53] M. Baranger and E. Vogt, editors, *Advances in Nuclear Physics*, volume 4, chapter 3, 1970.

- [54] J. D. Jackson, *Classical Electrodynamics*, John Wiley and Sons, New York, 2nd edition, 1975.
- [55] W. Lee, D. Mahood, P. Ryge, P. Shea, and T. Gozani, Nuclear Instruments and Methods in Physics Research B **99**, 739 (1995).

Appendix A

PULSE SHAPE DISCRIMINATOR ELECTRONICS

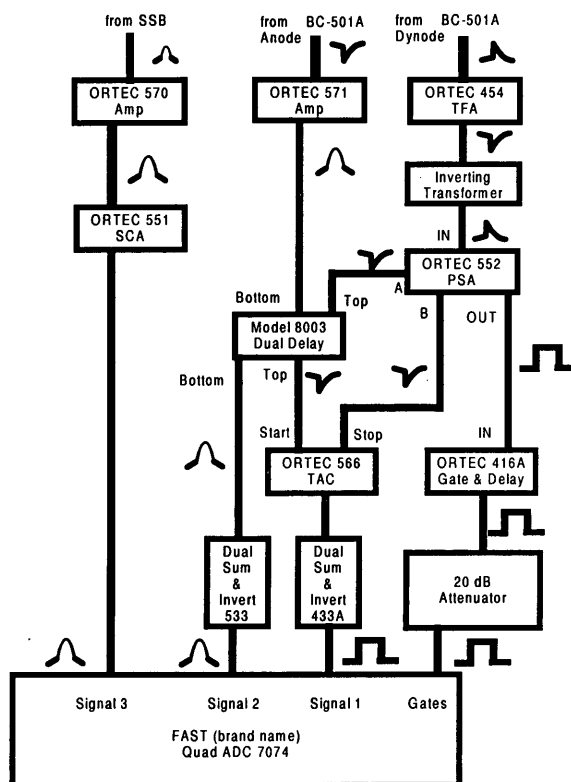


FIG. A.1. Pulse shape discriminator electronics details with pulse shapes.

Appendix B

SELECT PROPERTIES OF BC-501A

Table B.1. Select properties of the organic liquid scintillator BC-501A

Light Output	78% athracene
Wavelength of maximum emission	425 nm
Flash point, T.O.C.	26°C
Refractive index	1.505
Decay time (short component)	3.2 ns
Mean decay times of first three components	3.16, 32.3, & 270 ns
Mean lifetime for solute to solvent energy transfer	1.66 ns
Number photoelectrons / keV energy loss	1.7
α/β ratio, "fast"	0.073
α/β ratio, "slow"	0.098
H / C (atomic ratio)	1.212
Number H atoms per cc	4.82×10^{22}
Number C atoms per cc	3.98×10^{22}
Number of electrons per cc	2.87×10^{23}

Appendix C

**SAMPLE KENT STATE NEUTRON DETECTION EFFICIENCY
CODE INPUT FILE**

```

6 BY 6 BY 6 CYLINDRICAL BC501A DETECTOR
SENSE SWITCH SETTINGS AND NUMBER OF EVENTS TO DUMP (6I1,I4)
122222 0 1 GIVES MIN OUTPUT AND FAST EXECUTION, 2 GIVES MORE
BIAS (MEVEE), TIMING (NSEC) BIN WIDTH, POSITION (IN.) FOR STUDY (3F8.3)
0.244 0.1 0.2
TWO VALUES OF ONE-PE LEVEL (MEVEE) FOR RES. SMEARING (2F6.2)
.00588.02
SEED FOR RANDOM NUMBER GENERATOR (I5)
2223
DENSITY (GM/CM**3) AND RATIO OF H TO C ATOMS (2F8.3)
0.874 1.212
LIGHT OUTPUT COEF. FOR PROTONS (6F12.5)
-2.8000 -.20000 1.0000000 .81 0.0 0.0
LIGHT OUTPUT COEF. FOR ALPHAS (6F12.5)
-5.90000 -.065 1.01 .41 0.0 0.0
SCINTILLATOR BOUNDARIES (INCHES), IGEO, IRANP (3F6.2, 2I2)
6.0 6.0 6.0 1 1 0=RECT, 1=CYLINDER FACE, 2=CYL SIDE
POSITIONS DIRECTION COSINES ENERGY DELTA E COUNTS BINWIDTH
-----**.*-----**.*-----**.*-----**.*-----**.*-----**.*-----**.*
6 BY 6 BY 6 CYLINDRICAL BC501A DETECTOR
0.0 0.0 0.0 0.0 0.0 1.0 8.15 0.00 100000 3.06e-2
0.0 0.0 0.0 0.0 0.0 1.0 8.06 0.00 100000 3.06e-2
0.0 0.0 0.0 0.0 0.0 1.0 7.87 0.00 100000 3.06e-2

```

FIG. C.1. Sample input file for Kent State University Neutron Detector Efficiency code

Appendix D**CHARGED PARTICLE AND NEUTRON DATA**

Table D.1. Charged particle monitor reactions for the ^2H and ^6Li reactions

Monitor Reaction	Deuteron Lab Energy (keV)	Neutron Detector Angle ($^\circ$)	Counts (#)	
			Raw	Corrected
$^2\text{H}(\text{d,p})^3\text{H}$	60	0	2830	2830
		30	3338	3338
		60	4899	4899
		90	4077	4077
	105	0	5989	5989
		30	8328	8328
		60	10138	10138
		90	11651	11651
		90	12603	12603
	$^6\text{Li}(\text{d,p})^7\text{Li}$	140	0	13894
30			3216	3216
60			5264	5264
90			7921	7921

Note: The background contributions were negligible for these two reactions.

Table D.2. Charged particle monitor reactions used for the ${}^7\text{Li}(d,n){}^8\text{Be}$ reaction

Monitor Reaction	Deuteron Lab Energy (keV)	Neutron Detector Angle ($^{\circ}$)	Counts (#)	
			Raw	Corrected
${}^6\text{Li}(d,p_0+p_1){}^7\text{Be}$	145	0	9681	40800
		30	10690	40040
		60	11365	48471
		90	6104	25187
	120	0	2721	11027
		30	2505	11307
		60	3085	13520
		90	7083	28320
${}^6\text{Li}(d,\alpha){}^4\text{He}$	70	0	69	920
		30	44	587
		60	41	547
		90	32	427

Note: The corrected counts account for the isotopic abundances in the natural lithium used as targets.

Table D.3. Charged particle monitor reactions for ^9Be , ^{10}B , and ^{11}B

Reaction	Deuteron Lab Energy (keV)	Neutron Detector Angle ($^\circ$)	Counts (#)	
			Raw	Corrected
$^9\text{Be}(d,p_0)^{10}\text{Be}$	145	0	523	523
		30	833	671
		60	1218	678
		90	1818	738
$^{10}\text{B}(d,\alpha_0)^8\text{Be}$	145	0	807	387
		30	874	454
		60	712	334
		90	901	292
		120	605	227
$^{10}\text{B}(d,\alpha_0)^8\text{Be}$ Note: used for the $^{11}\text{B}(d,n)^{12}\text{C}$ calculations	145	0	69	298
		30	83	247
		60	62	268
		90	65	328
		120	133	328

Note: As with the ^6Li particle data used for the $^7\text{Li}(d,n)^8\text{Be}$, the corrected counts account for the isotopic abundances of the boron.

Table D.4. Range of sampled channels for determining counts from deuteron-induced proton transfer reactions on ^2H and on ^6Li

Reaction	Deuteron Lab Energy (keV)	Neutron Detector Angle ($^\circ$)	Summation Channels	
			Minimum	Maximum
$^2\text{H}(\text{d},\text{n})^3\text{He}$	60	0	21	30
		30	20	30
		60	20	30
		90	20	28
	105	0	15	30
		30	15	30
		60	15	30
		90	15	30
$^6\text{Li}(\text{d},\text{n})^7\text{Li}$	140	0	28	40
		30	28	40
		60	28	40
		90	27	37

Note: Minimum channel is lowest channel in sample of summations. Maximum channel is the highest channel in sampling of summations.

Table D.5. Range of sampled channels for determining counts from deuteron-induced proton-transfer reactions on ${}^7\text{Li}$

Reaction	Deuteron Lab Energy (keV)	Neutron Detector Angle ($^\circ$)	Summation Channels	
			Minimum	Maximum
${}^7\text{Li}(d,n){}^8\text{Be}$	145	0	34	45
		30	32	45
		60	30	41
		90	27	40
	120	0	34	45
		30	32	44
		60	30	42
		90	23	43
	70	0	33	46
		30	34	44
		60	29	41
		90	29	41

Note: Minimum channel is lowest channel in sampling of summations. Maximum channel is the highest channel in sampling of summations.

Table D.6. Range of sampled channels for determining counts from deuteron-induced proton-transfer reactions on ^9Be , ^{10}B , and ^{11}B

Reaction	Deuteron Lab Energy (keV)	Neutron Detector Angle ($^\circ$)	Summation Channels	
			Minimum	Maximum
$^9\text{Be}(d,n_0)^{10}\text{C}$	145	0	24	27
		30	20	24
		60	18	21
		90	17	21
$^9\text{Be}(d,n_1)^{10}\text{C}$	145	0	14	17
		30	12	15
		60	11	15
		90	11	13
$^{10}\text{B}(d,n)^{11}\text{C}$	145	0	14	21
		30	14	21
		60	14	21
		90	12	20
		120	12	19
$^{11}\text{B}(d,n)^{12}\text{C}$	145	0	26	41
		30	27	41
		60	27	39
		90	24	40
		120	26	37

Note: Minimum channel is lowest channel in sampling of summations. Maximum channel is the highest channel in sampling of summations.

Table D.7. True counts determined for deuteron-induced proton transfer reactions on ^2H and on ^6Li .

Reaction	Deuteron Lab Energy (keV)	Neutron Detector Angle ($^\circ$)	total Counts	
			True	Variance ($\pm\%$)
$^2\text{H}(\text{d},\text{n})^3\text{He}$	60	0	9219	5.97
		30	9284	4.16
		60	9836	4.55
		90	7478	4.78
	105	0	18159	10.6
		30	21414	12.7
		60	21194	7.68
		90	20878	12.4
$^6\text{Li}(\text{d},\text{n})^7\text{Li}$	140	0	29784	1.37
		30	7215	2.50
		60	11220	2.48
		90	17202	3.33

Note: Variance is the magnitude of the difference between the average value [true counts] and the average of the extrema from the mean within the sample population.

Table D.8. True counts determined for deuteron-induced proton-transfer reactions on ${}^7\text{Li}$

Reaction	Deuteron Lab Energy (keV)	Neutron Detector Angle ($^\circ$)	Total Counts	
			True	Variance ($\pm\%$)
${}^7\text{Li}(d,n){}^8\text{Be}$	145	0	106545	4.00
		30	131258	4.94
		60	203377	2.34
		90	117038	2.64
	120	0	34737	2.77
		30	30445	4.13
		60	44139	4.37
		90	133189	3.97
	70	0	2641	5.55
		30	1996	4.09
		60	1364	4.18
		90	1601	4.65

Note: Variance is the magnitude of the difference between the average value [true counts] and the average of the extrema from the mean within the sample population.

Table D.9. True counts determined for deuteron-induced proton-transfer reactions on ^9Be , ^{10}B , and ^{11}B

Reaction	Deuteron Lab Energy (keV)	Neutron Detector Angle ($^\circ$)	Totals Counts	
			True	Variance ($\pm\%$)
$^9\text{Be}(d,n_0)^{10}\text{C}$	145	0	5180	5.41
		30	11524	4.34
		60	17216	7.34
		90	13645	9.04
$^9\text{Be}(d,n_1)^{10}\text{C}$	145	0	17186	5.41
		30	25288	5.43
		60	27828	7.17
		90	48188	3.81
$^{10}\text{B}(d,n)^{11}\text{C}$	145	0	5221	5.23
		30	6579	4.04
		60	5746	4.44
		90	5397	5.21
		120	4433	6.02
$^{11}\text{B}(d,n)^{12}\text{C}$	145	0	8432	3.15
		30	7998	5.02
		60	10582	3.66
		90	14017	5.68
		120	8309	3.42

Note: Variance is the magnitude of the difference between the average value [true counts] and the average of the extrema from the mean within the sample population.